Investigation of Mechanical Properties of Graphene on Silicon Wafers

This thesis is submitted in fulfilment of the requirements for the degree of

Doctor of Philosophy

from

University of Technology Sydney

by

Zulfiqar Hasan Khan

B. Sc. (Hons) & M. Sc.

School of Electrical and Data Engineering

Faculty of Engineering and Information Technology

2017

ABSTRACT

Graphene is an atomically thin two-dimensional crystalline material with very low mass, high Young's modulus, high elastic strength, high optical transparency, high-electron mobility, high thermal conductivity and high degree of biocompatibility. Due to these extraordinary properties, graphene has many promising applications. Graphene can be synthesized in vastly different ways, for example by chemical vapour deposition and micromechanical exfoliation. However, the invariably poor graphene/substrate adhesion energy is a major drawback for ensuring the reliability, stability and longevity of sensors and other micro- and nano-mechanical devices, precluding us from achieving semiconductor technology requirements and rendering manufacturing efforts futile. Therefore, synthesising wafer level graphene that has sufficient quality and adhesion with the substrate is still an open and critical research problem.

To address these issues, we have demonstrated for the first time a fivefold improvement in adhesion between graphene and its underlying substrate, using a transfer-free, catalytic alloy approach for synthesising a monolayer of graphene on silicon carbide on silicon. An interfacial adhesion energy of 5.7 J/m^2 between graphene and silicon carbide is found using double cantilever beam testing, as compared to 1.02 J/m^2 reported for transferred graphene on silicon dioxide.

As the obtained adhesion energy is a good starting point for achieving reliable resonant sensors, we have fabricated and evaluated graphene coated silicon carbide membranes, showing quality factor (Q) as high as $2.7x10^4$. We have also investigated the influence of graphene coating on the quality factor of the silicon carbide membrane resonators and reported a significant reduction in damping when a graphene overlayer is present on silicon carbide membranes instead of a conventional metal layer.

CERTIFICATE OF ORIGINAL AUTHORSHIP

I, Zulfiqar Hasan Khan, certify that the work presented in this thesis has not previously been submitted for a degree nor been submitted as part of the requirements for a degree except as fully acknowledged within the text.

I also certify that the thesis has been written by me. Any help that I have received in my research work and the preparation of the thesis itself has been acknowledged. In addition, I certify that all information sources and literature used are indicated in the thesis.

Production Note:
Signature removed prior to publication.

Zulfiqar Hasan Khan

Sydney, Australia

August 2017

DEDICATION

This thesis is dedicated to my family. Thank you for all of your love and support.

ACKNOWLEDGEMENTS

I would like to gratefully thank the many people who have helped, encouraged and supported me through the years spent in finishing this work. I would like to express my deepest gratitude to my principle supervisor, Professor Francesca Iacopi for her invaluable advice, guidance and supervision throughout this research work. Her knowledge, experience and support were very helpful in helping me pass the many obstacles that I faced.

A special thanks to Professor Reinhold Dauskardt, my external supervisor, for hosting me at his lab at Stanford University, California, United States in 2016. The assistance and collaboration provided by Dr. Ryan Brock at Stanford was much appreciated. I would also like to thank Professor Warwick Bowen and James Bennett of the University of Queensland Quantum Nano/Opto-mechanics group for providing the optical measurements in this work. I would like to thank Avi Bendavid of CSIRO Manufacturing, Lindfield, NSW, Australia for the XPS measurements.

My appreciation is extended to the Australian National Fabrication Facility (ANFF, Queensland node) and ANFF, UQ staff members Kai-Yu Liu, Elliot Cheng, Doug Mair, Wael Al Abdulla, Elena Taran, and Lien Chau for their instrumental support. I appreciate the administrative and technical support I received from Dian Riseley of the Environmental Futures Research Institute (EFRI) at Griffith University and Phil Moffat, Eryani Tjondrowalujo, Caroline Harvey, Dr. Ronald Shimmon, Dr. Linda Xiao, Katie McBean, and Mark Berkahn at the University of Technology Sydney (UTS).

In addition, I would like to acknowledge the University of Technology, Sydney for providing me with the PhD scholarship. Thanks extended to the Graduate Research School (GRS) and my colleagues at the School of Electrical and Data Engineering of UTS.

One of the wonderful aspects of doing a Ph. D. is going through it together with other graduate students. I was lucky enough to have phenomenal friends and colleagues, in particular Dr Atieh Ranjbar Kermany, Dr. Neeraj Mishra, Dr. Mohsin Ahmed, Dr. Bei Wang, Ms. Aiswarya Pradeepkumar, Dr. Sai Jiao, and Dr. Anjon Mondal whose collaboration has helped me greatly in my work. I would also like to thank my close friend Dr. Nurul Kabir who encouraged me constantly. Last, but not least, I express my deepest gratitude to my wife, daughter, mother, father and all family members for their endearing encouragement, patience, and love.

TABLE OF CONTENT

LIST OF FIGURES

LIST OF TABLES

THESIS FRAMEWORK

This thesis is divided into six chapters: Chapter 1: Introduction; Chapter 2: Published review paper–*Mechanical and electromechanical properties of graphene and their potential applications in Micro Electro-Mechanical Systems (MEMS)*; Chapter 3: Methodology; Chapters 4: Unpublished paper–*Ultrahigh adhesion of epitaxial graphene on SiC on silicon*; Chapter 5: Mechanical performance of graphene on cubic silicon carbide membrane resonators on silicon, and Chapter 6: Conclusion.

Chapter 1 is the introduction, and includes a brief discussion of the research background, motivation, importance and scope of the work. It also provides the thesis framework and the list of publications.

Chapter 2 is the literature review in the form of a published journal paper, which reviews the types of graphene, the mechanical properties of graphene such as elastic and fracture properties, its thermo-mechanical properties**,** as well as its tribology, adhesion and electromechanical properties. This chapter includes a comparative study of the adhesion of graphene on different substrates as measured by different tests. Moreover, this chapter provides a general overview of MEMS resonators; dynamic resonant sensing parameters, such as resonance frequency and quality factor; resonant sensing principles; electrical actuation and detection schemes; and transduction techniques. Lastly, this chapter discusses the potential of graphene in MEMS and examples of applications. Overall, the idea of this chapter is to present a review and explanation of the existing literature on the mechanical properties of graphene.

The overall experimental methodology is introduced in Chapter 3. It starts with graphene synthesis, followed by characterization techniques (for evaluating the graphene and the membranes resonators) and for performing the failure analysis after

mechanical fracture or delamination. Next, the chapter explains double cantilever beam (DCB) and four-point bending (FPB) test sample preparation, the microresonator fabrication stages, including photolithography, silicon carbide (SiC) and silicon (Si) etching. Subsequently, it covers the principles of DCB testing, FPB testing and the optical measurements of the mechanical properties (*f* and *Q)* of membrane resonators by using Mach-Zehnder optical interferometry. Lastly, it specifies all the implemented instruments and their specifications. The intention of this chapter is to discuss the equipment, methods, and the calculations that were used throughout this work.

Chapter 4 presents the sample preparation for the four-point bending test and the double cantilever beam-bending test. Chapter 4 focuses on the measurement of the adhesion energy of nickel-copper (Ni-Cu) alloy mediated catalytic graphene on SiC on Si by the DCB test. This chapter also describes the failure analysis undertaken, in order to verify the location of the debonding path. This result of the DCB test is significant because of the fact that catalytic graphene offers fivefold improvement in adhesion compared to adhesion between graphene and silicon dioxide (SiO_2).

Chapter 5 includes the results obtained from the simulation, fabrication, characterization and the measurement of the mechanical properties of the graphene coated SiC resonators, Ni-Cu coated SiC resonators and uncoated SiC resonators. Thus, the chapter reports the influence of graphene coating on mechanical properties of SiC membrane resonator. Moreover, the chapter demonstrates *Q*-factor improvement of graphene coated SiC membrane resonator by backside etching.

Finally, a general conclusion is given in chapter 6, which provides a summary and benefits of this work; and suggests ideas for future advances in this area.

LIST OF ABBREVIATIONS

Abbreviations/Symbols	Full name
CVD	Chemical vapor deposition
AFM	Atomic force microscopy
Si	Silicon
SiC	Silicon carbide
3C-SiC	Cubic silicon carbide
SEM	Scanning electron microscopy
MEMS	Micro-electro-mechanical systems
FEM	Finite element modelling
G	Strain energy release rate
G_c	Critical strain energy release rate
Ψ	Mode mixity/ Phase angle
P_c	Critical load
F	Resonant frequency
Q	Quality factor
E	Young modulus
E'	In-plane strain modulus of the substrate
P	Density
L	Distance between outer and inner dwell pin
DRIE	Deep reactive ion etching
XPS	X-ray photoelectron spectroscopy
a.u.	Arbitrary unit
SiO_2	Silicon dioxide
Si_3N_4	Silicon nitride

SiC/Si	Epitaxial silicon carbide on silicon

JOURNAL PUBLICATIONS

1 **Khan Z H**, Kermany A R, Öchsner A, Iacopi F. "Mechanical and electromechanical properties of graphene and their potential application in MEMS". *Journal of Physics D: Applied Physics*, 50(5):053003, 2017.

AWARDS

1. First prize in 3-minute presentation at School of Electrical and Data Engineering, UTS.

2. Finalist in the HDR research showcase, 2017, for the Faculty of Engineering and Information Technologies.

CONFERENCES AND WORKSHOPS

1. ANN ECR Workshop Griffith University, 2015, Goldcoast, Queensland, Australia.

2. Z. H. Khan *et al*., 5th International Symposium on Graphene Devices, 2016, Brisbane, Australia.

3. Z. H. Khan *et al.*, SPIE Conference, 2016, San Diego, California, United States.

Chapter 1–Introduction

1.1 Properties & Applications

Graphene, as a single-layer of sp^2 bonded carbon atoms organized into a hexagonal lattice, is an ideal structural material for achieving better performance and sensitivity than conventional MEMS and NEMS [1-5]. Graphene possesses a plethora of outstanding properties such as 1 TPa Young's modulus [6, 7], exceptionally high 2D failure strength [8, 9], high thermal conductivity, good electrical conductivity [10, 11], high optical transparency [12], extraordinary flexibility, lightness, robustness and chemical inertness [13]. The adhesion energy between graphene and its substrate is one of the practical mechanical properties which is crucial for ensuring stability and longevity of graphene based micro/nano devices [14].

Insufficient adhesion in graphene coated SiC micro-resonators can result in folding, bending and even auto-lift-off of the graphene sheet during device fabrication and/or operation, leading to the resonator failure [15-17]. Therefore, improving the adhesion between graphene and its substrate is prerequisite for reliable device fabrication.

Other than use in sensing applications, ultrahigh adhesion of graphene may be useful for preventing delamination in pressurized suspended graphene membranes [18]. For example, ultrahigh adhesion can result in higher efficiency of gas separator membranes because it will be able to tolerate a wider range of pressures. Moreover, ultrahigh adhesion may make the strain-induced bandgap opening possible in a pressurized suspended graphene membrane [19].

1.2 Graphene synthesis

Graphene synthesis is categorised into two types: transferred graphene and transfer-free graphene [5].

1.2.1 Transferred graphene

For transferred graphene, the relocation of the graphene onto a working substrate is needed after synthesis for device fabrication. The chemical vapour deposition (CVD) growth on metal foil [20-22], the reduction of graphene oxide and the exfoliation techniques are generally referred to as being the 'transferred graphene' type.

The main advantage of CVD graphene is its scalability [5]. CVD graphene is promising in making flexible and transparent electronics [23-27] and corrosion protective coatings [13, 28-31]. In contrast, the advantage of exfoliated graphene is that it is pristine in nature and it ensures high quality graphene synthesis. However, lack of scalabity and controlling number of layers are two major drawbacks for graphene synthesis by exfoliation [5]. Therefore exfoliated graphene is suitable for laboratory scale fabrication of high performance devices [5].

The main limitation of transferred graphene is the poor adhesion energy between graphene and the substrate after the transfer [32]. This limitation makes wafer-level fabrication extremely challenging if not impossible.

1.2.2 Transfer-free graphene

Graphene obtained by thermal decomposition [33, 34] of bulk SiC or by thermal decomposition of cubic silicon carbide thin film on silicon (3C-SiC/Si) [35] are examples of transfer-free graphene.

The advantages of transfer-free graphene include the ability to grow graphene on top of a wide bandgap semiconductor substrate (SiC) [36, 37] and the potential of wafer-

scale production [36]. The drawbacks of epitaxial graphene obtained by thermal decomposition of 4H-SiC are the high cost of commercial bulk wafers and limited wafer scale (6 inch). Further, this method also requires high thermal budget (1300^0C-1600^0C) for the graphitization [1].

1.2.2.1 Metal catalyst assisted graphitization

To alleviate the above-mentioned drawbacks of epitaxial graphene on SiC based on thermal decomposition of SiC bulk wafers, our group proposed a catalytic metal assisted graphitization method. Catalytic graphene is grown at a much lower temperature (1100^0C) compared to the sublimation technique [1, 33, 38]. Catalytic graphene is a more affordable technique for graphene synthesis because 3C-SiC can be grown on inexpensive Si wafers and is compatible with existing silicon process technology. For this method, Ni and Cu are first deposited on top of the 3C-SiC/Si substrate using an e-beam evaporator; then being annealed at 1100°C for about an hour under medium vacuum (below ~10^{-3}-10^{-4}mbar) [1, 36, 39].

There are three intermediate steps of the graphitization process [39]. The first step is the oxidation of Ni. The second step is the oxidation and amorphization on the top few tens of nm of SiC surface and simultaneous release of atomic carbon. The third step is the formation of the graphene layer on the SiC surface by catalytic action of Cu. Finally, after removing the metal silicides by Freckle etching, a monolayer graphene is obtained on 3C-SiC/Si [Appendix A, 39].

The study of adhesion between catalytic graphene and SiC substrate is imperative, since the available information on adhesion between transfer-free graphene and SiC substrate is minimum.

1.2.2.2 Challenges for adhesion measurement

Most measurements of graphene adhesion reported in literature have been limited to transferred graphene [40-42] whereas to date, no direct measurement of adhesion has been performed for transfer-free graphene. There are no reports of double cantilever beam (DCB) adhesion tests in the literature to measure graphene adhesion on bulk SiC, likely due to the higher relative brittleness of SiC wafers, leading to beam fracture at relatively low loads. Due to the difficulty in producing graphene with consistent coverage on a sufficiently large area on SiC, there has been no study of adhesion of the transfer-free graphene on 3C-SiC/Si. Herein, we discuss the first of such measurements by DCB test.

1.3 Methodology

Sandwiched structured specimens for DCB tests are prepared by bonding the graphitized 3C-SiC/Si wafer with the mirroring Si wafer. Then the individual rectangular beams are diced out from the sandwiched structured. For the DCB test, both Si beams are loaded and unloaded at a constant displacement rate, while the applied load is monitored as a function of the displacement to obtain a load-displacement curve. At a critical value of load, P_c, the load-displacement curve demonstrates a deviation from linearity and shows a sharp decrease, indicating the initiation of debonding. Multiple loading/crack-growth/unloading cycles were performed to measure the respective crack lengths. From the critical loads and corresponding crack length, the adhesion energy of the catalytic graphene on 3C-SiC has been measured [43]. The location of the debonding is verified through failure analysis with Raman, SEM and surface XPS analysis on both sides of the delaminated interface.

After measuring high adhesion, graphene coated silicon carbide membrane resonators were fabricated by backside Si etching in deep reactive ion etching (DRIE) and the performances (f and Q) were measured by the "free ring-down" method [44].

1.4 Summary

The importance of this work lies in two aspects:

1) This is the first study of adhesion between graphene and 3C-SiC substrate on Si. We measured the adhesion between transfer-free catalytic graphene and 3C-SiC/Si substrate as 5.7 J/m^2 by double cantilever beam fracture mechanics testing. Since the reported adhesion of transferred graphene on SiO_2 is 1.02 J/m^2 or lower [32, 45], the catalytic graphene demonstrates a five-fold improvement of adhesion.

2) The high adhesion between graphene and 3C-SiC made it possible to study the influence of graphene on the performance of SiC membrane resonator in terms of the Q factor. We found its potential to replace metals as actuation and readout circuit material.

Chapter 2–Mechanical and electromechanical properties of graphene and their potential applications in MEMS*

*This chapter includes a co-authored published paper. The bibliographic details of the co-authored published paper, including all authors, are:

Khan Z H, Kermany A R, Öchsner A, Iacopi F. "Mechanical and electromechanical properties of graphene and their potential application in MEMS". *Journal of Physics D: Applied Physics*, 50(5):053003, 2017.

Chapter 3–Methodology

3.1 Catalytic graphene synthesis

For synthesizing monolayer graphene on 3C-SiC epitaxial films on Si substrate, an 'alloy mediated catalytic approach' is used. First, nickel (Ni) and copper (Cu) are sputtered on the SiC surface via a Temescal FC-2000 e-beam evaporator at a rate of 1 – 1.5 Å/sec and at a base pressure of 2×10^{-6} Torr. Next, the samples are introduced into a Carbolite high temperature (HT) furnace for thermal annealing at moderate temperature (1100 °C) and vacuum (10^{-3}-10^{-4} mbar). The cool down ramp is about 8 hours from 1100 °C to room temperature under medium vacuum. The steps for catalytic graphene synthesis are shown in figure 3.1.

Figure 3.1 Schematic of the catalytic graphene synthesis process.

A highly intermixed layer of metal and metal silicides are produced during the annealing. By immersing the graphitized samples into Freckle etch solution for six hours, the intermixed layer is removed.

After that, we performed wet chemical etching with Freckle's etch solution [36] for metal and metal silicide removal and to get a monolayer of graphene on the SiC (100). Freckle solution could be prepared by mixing acids with specific ratio. The ratio mix for making the Freckle etch solution is: 85% Phosphoric Acid (H_3PO_4): Glacial acetic acid:70% HNO_3:48% Tetraflouroboric Acid (HBF_4):H_2O ≡70:10:5:5:10. After

immersion in the freckle solution, the samples were finally rinsed with milli-Q water and dried by Nitrogen gas flow.

3.2 Characterization techniques

3.2.1 Scanning electron microscope

The SEM produces images by scanning the sample with a high-energy beam of electrons produced from an electron source. For example, Tungsten (W) electron filament consists of an inverted V-shaped 100 μm long wire of tungsten, which is heated resistively to produce electrons [231]. The produced electron beam penetrates the sample to a depth of a few microns, depending on the accelerating voltage and the density of the sample.

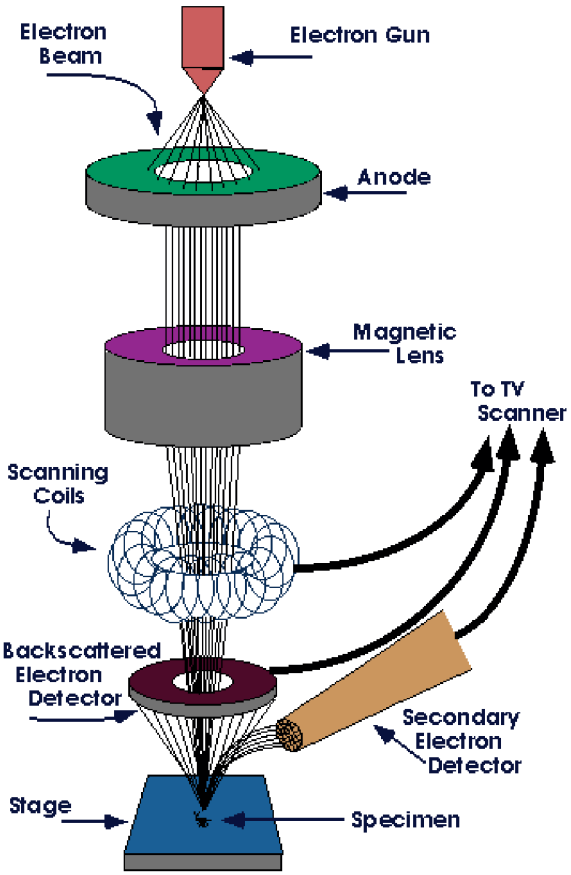

Figure 3.2 Basic diagram of scanning electron microscope [232].

As the electrons interact with the sample, they produce two types of electrons: i) secondary electrons and ii) backscattered electrons. Backscattered electrons are higher energy electrons that are elastically backscattered by the atoms of the sample. On the other hand, secondary electrons are low energy electrons produced when electrons are ejected from the k-orbitals of the sample atoms by the imaging beam. The detector collects the electrons coming off the sample. Since electrons have much shorter wavelengths than visible light, better resolution is achieved in SEM images. Depending on electron spot size and the interaction volume of the electron beam with the sample, modern full-sized SEMs provide resolution of between 1 and 20 nm [233]. Thus, SEM images of delaminated surfaces can preliminarily indicate whether our interface of choice has been debonded during the double cantilever beam adhesion test or four-point bending test.

3.2.2 Raman spectroscopy

The inelastic interaction between a photon and a molecule is known as the Raman effect. There are two types of Raman effect: Stokes Raman scattering, and anti-Stokes Raman scattering. In Stokes Raman scattering, atoms or molecules absorb energy, move to a higher vibrational energy level, which results in scattered photons with less energy than the incident photon. On the other hand, in the case of anti-Stokes Raman scattering, atoms or molecules loses energy, move to a lower vibrational energy level and so the scattered photons have more energy than the incident photons.

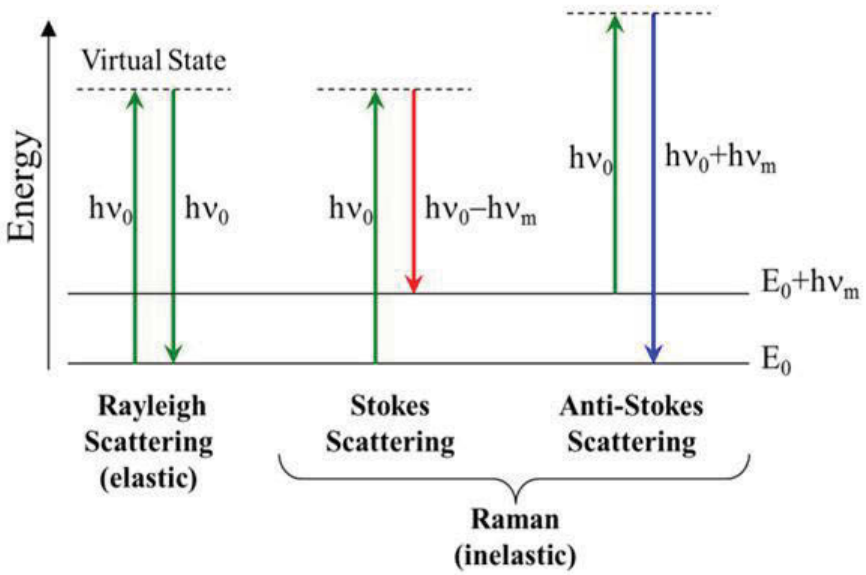

Figure 3.3 Energy diagram for Raman scattering [234].

The various energy shifts associated with different molecular vibrations leads to a Raman spectrum. The Raman spectrum provides a spectral fingerprint to detect atoms/molecules present in a sample. Raman spectroscopy needs to be carried out to confirm delamination between desired interfaces in an adhesion test.

3.2.3 X-ray photoelectron spectroscopy (XPS)

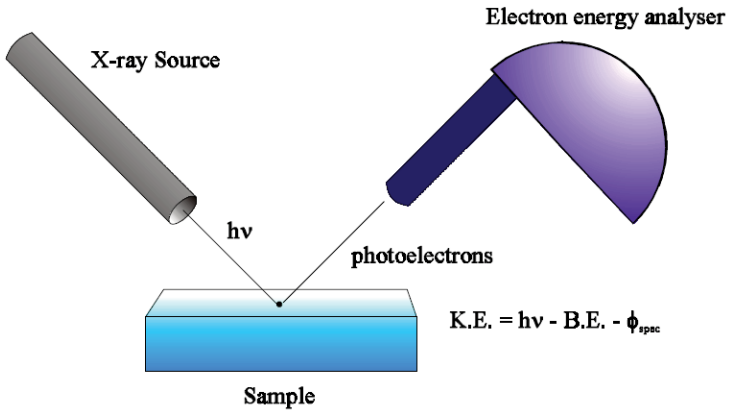

Figure 3.4 Basic diagram representing working principle of X-ray photoelectron spectroscopy [235].

In XPS, an incident "soft" X-ray photon of 200-2000 eV energy (hv) knocks an electron out of the atom by photoelectric effect. The resulting photoelectrons escapes with an energy equal to

$$K_E = hv - B_E - \Phi \quad (3.1)$$

$$\text{or, } B_E = hv - K_E - \Phi \quad (3.2)$$

where, Φ = spectrometer work function (of the order of a few eV).

and B_E= binding energy of core electron

The binding energy of electron could be measured from the energy of the incident X-ray, kinetic energy of photoelectron and spectrometer work function. As different elements have different binding energies, XPS can find out which elements are present in the surface region.

Although X-ray penetration depth is~μm, photoelectrons cannot escape from depths greater than 10-80 A^o inside a material [236]. As electrons are extracted only from a narrow region around the surface, XPS is a perfect analytical tool for investigating which interface has been debonded.

XPS is performed in an ultra-high vacuum (UHV) chamber to avoid scattering of the XPS electrons with air. Samples can be studied without any preparation other than normal cleaning. XPS can detect elements starting from Li (Z=3) and other atoms with higher atomic number (Z > 3); hydrogen (Z = 1) and helium (Z = 2) cannot be detected due to the low probability of electron emission. XPS has only 6 – 8 nm probing depth, 0.003 to 0.008 times that of EDS, XRF, and FTIR [236], which makes XPS most convenient for surface analysis after delamination. In this thesis, the chemical bonding and composition of the surface of the samples was assessed by XPS using a Specs 150 SAGE instrument operated with a Mg K_α X-ray source (Mg anode operated at 10 keV

and 10 mA). Binding energies of some of the relevant chemical states are tabulated in Table 3.1.

Table 3.1 Binding energies of common chemical states in XPS spectra.

Chemical State	Binding Energy (eV)
C-C (sp_2 carbon)	~284
C-C (sp_3 carbon)	~284.8
C-Si	282.7
C-O	~286
C=O	~289
Cu metal	933
Ni metal	852.6

3.2.4 Atomic force microscopy (AFM)

Atomic force microscopy (AFM) is a very powerful high-resolution scanning probe microscopy with demonstrated horizontal and vertical resolution down to a fraction of a nanometer. AFM is operated by measuring the force between the sample and the probe.

Generally, the probe is a sharp tip with a 3-6 μm tall pyramid and a 15-40 nm end radius [237]. AFMs can normally measure the vertical and lateral deflections of the cantilever by using the optical lever to obtain the image resolution [237]. The optical lever functions by reflecting a laser beam off the cantilever. The reflected beam of laser strikes a position-sensitive four-segment photo-detector. The differences between the segments of the photo-detector specify the position of the laser spot on the detector as

well as the angular deflections of the cantilever (figure 3.5) [237]. Piezo-ceramics, a kind of material that expands or contracts in the application of a voltage gradient, act as high resolution and high precision three-dimensional positioning devices for the tip [237].

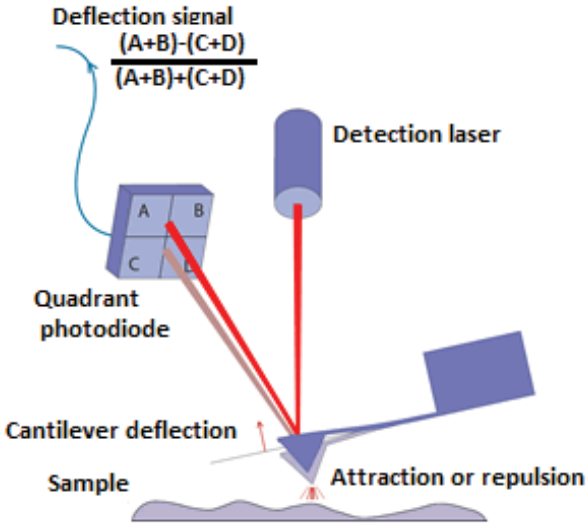

Figure 3.5 Schematic of atomic force microscopy (adapted from [238]).

AFM has three different modes of operation such as contact mode, tapping mode and non-contact mode. In the contact mode of an AFM operation, the cantilever scans across the sample surface; whereas in the non-contact mode of scanning in an AFM operation, the cantilever oscillates just above the surface without contacting as it scans. In the tapping mode, the cantilever oscillates at a much higher amplitude of oscillation compared to the non-contact mode. The bigger oscillation makes the deflection signal large enough for the control circuit, and hence an easier control for topographical feedback [239]. The feedback loop maintains a constant oscillation amplitude by maintaining a constant RMS of the oscillation signal acquired by the split photodiode detector. The vertical position of the scanner at each (x,y) data point in order to maintain a constant setpoint amplitude is stored by the computer to form the

topographic image of the sample surface [239]. By maintaining a constant oscillation amplitude, a constant tip sample interaction is maintained during imaging [239]. In the research investigation reported in this thesis, a Digital Instruments Dimension 3100 atomic force microscope (AFM) was used in tapping mode to measure the topography of the sample before and after delamination; NanoScope Analysis 1.7 software was used to analyse the data.

3.3 Sample preparation

3.3.1 Double cantilever beam (DCB) test sample preparation

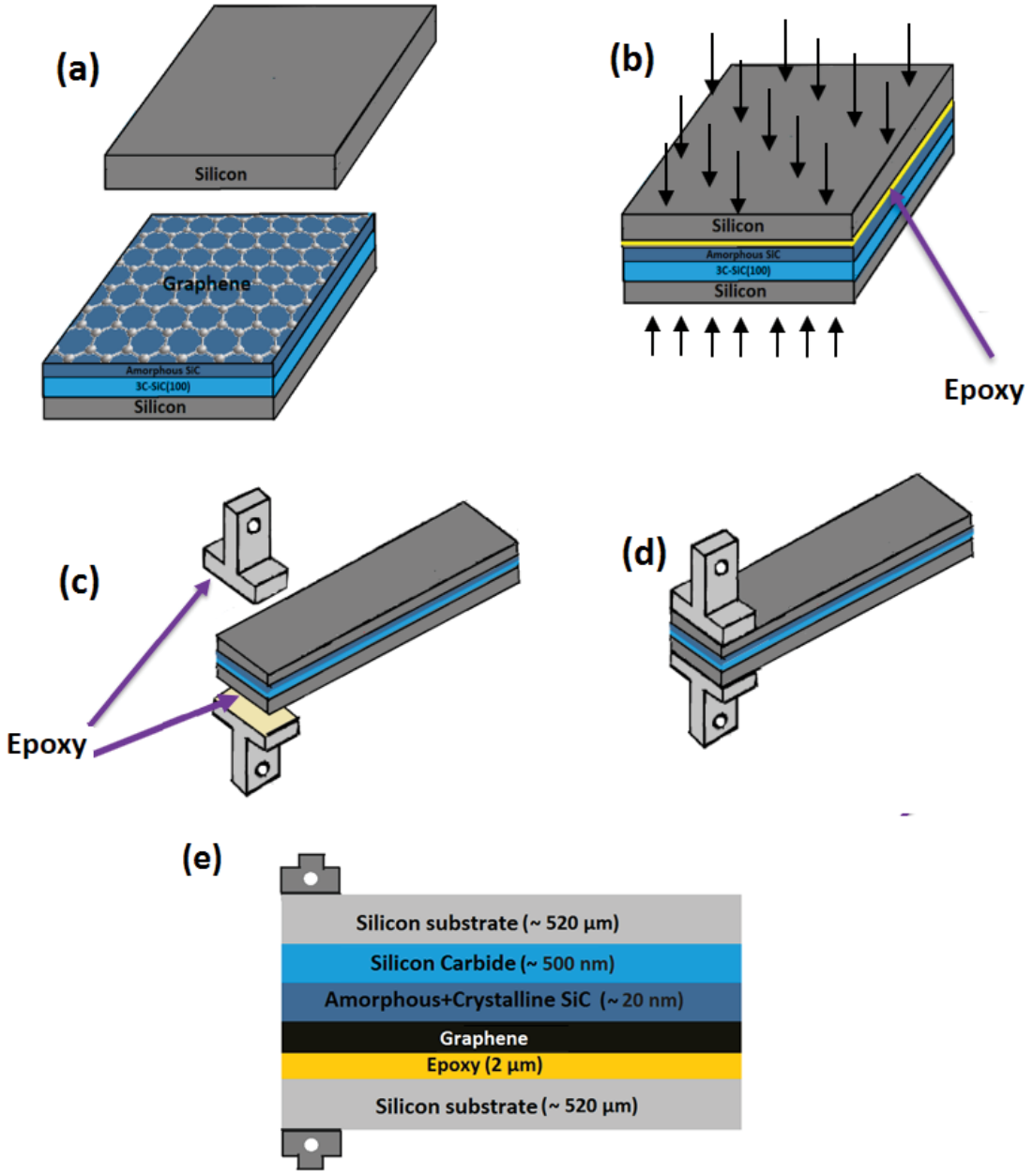

Figure 3.6 Description of DCB specimen preparation. (a) A silicon carbide on silicon containing graphene and a counterpart bank silicon substrate are cut to the same size, (b) Apply epoxy adhesive and attach two substrates and cure under constant clamping pressure, (c) Attach the aluminum loading tabs with epoxy adhesive, (d) Completed DCB specimen (e) Schematic of a sandwiched beam structure containing the graphene on SiC for DCB test of the interfacial debonding energies.

Specimens were fabricated by cutting a 30-mm wide and 60-mm long rectangular beam from a graphene/SiC/Si wafer and bonding it to a Si counterpart (figure 3.6(a)). A selected epoxy (EpoTek 353ND consisting of bisphenol F and imidazole; Epoxy Technology) was used for bonding. Then, the two substrates were bonded with constant clamping pressure (150kPa) (figure 3.6(b)) and the epoxy was cured for 1 hour at 125^0C in a convection oven. This curing resulted in an approximately 2μm thick epoxy layer.

Individual DCB specimens were diced from the sandwiched coupon using a dicer blade such that the dimensions of each beam were 5 mm x 60 mm x 1 mm. A commercial epoxy adhesive (Loctite E-20NS) was cured for 1 hour at 75^0C in a convection oven to attach the aluminum loading tabs on the DCB specimen (figure 3.6(c)). The excess epoxy was scraped off with a razor blade and the Si/SiC/graphene/Si stack sidewalls were polished with a Buehler Metaserv 250 Grinder/Polisher.

The completed DCB specimen is shown in figure 3.6(d) and the schematic of the cross-section of the sandwiched beam structure containing the graphene on SiC is represented in (figure 3.6(e)). Sometimes a precrack will not form even after overloading, due to excess epoxy flowing out of the interfaces and partially coating the Si beams at the end of the specimen. Therefore, the excess epoxy needs to be scraped off the sidewall of the specimen using a razor blade.

3.3.2 Four-point bending test sample preparation

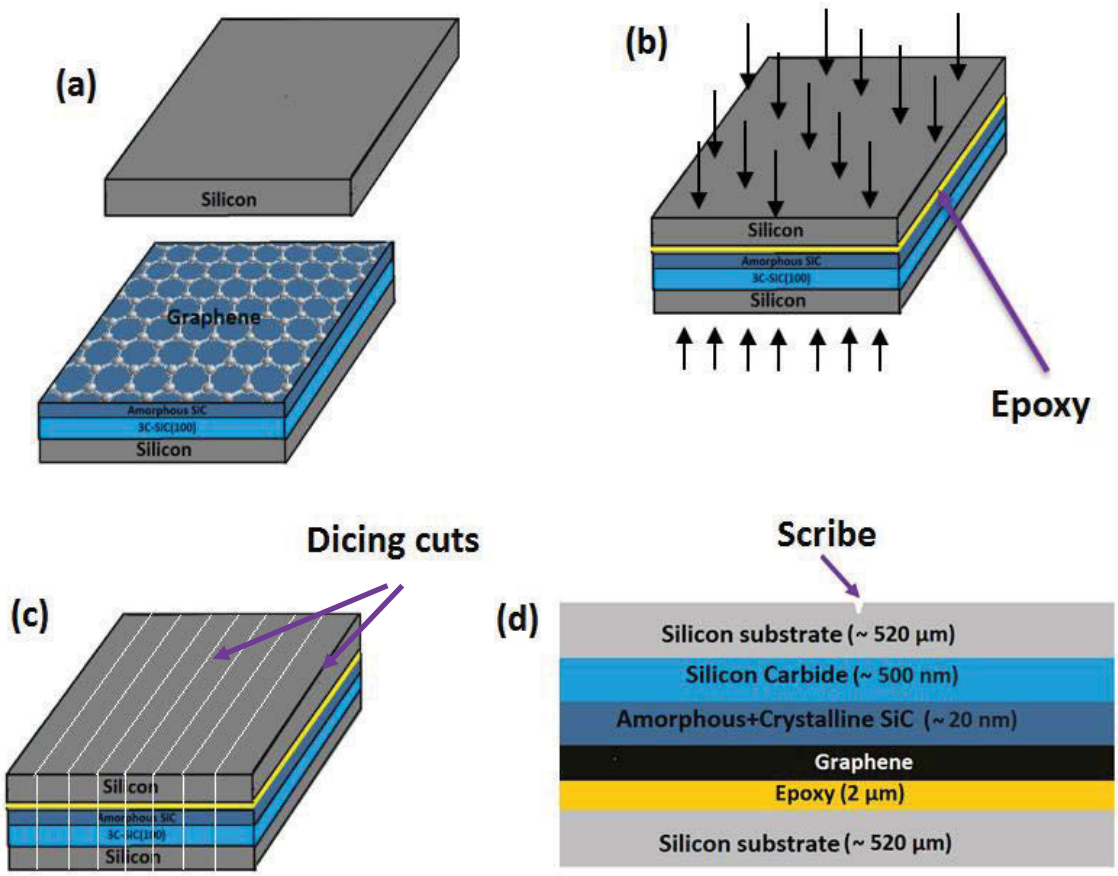

Figure 3.7 Description of DCB specimen preparation. (a) A silicon carbide on silicon containing graphene and a counterpart bank silicon substrate are cut to the same size, (b) Apply epoxy adhesive and attach two substrates and cure under constant clamping pressure, (c) Dice the stack into several FPB specimens (d) Sideview schematic of a FPB specimen.

Four-point bending test specimens were fabricated using the epoxy bonding technique. Speciments were fabricated by cutting a 30-mm wide and 50-mm long rectangular beam from a graphene/SiC/Si wafer and bonding it to a 530 µm Si wafer (figure 3.7(a)). A selected epoxy (EPO-TEK 353ND) was used for bonding and the two substrates were attached together with constant clamping pressure (150 kPa) (figure 3.7(b)). The epoxy was cured for 1 hour at 125^0C in a convection oven. This curing resulted in an approximately 2 µm thick epoxy layer. In this case, a central region (~5mmx50mm) was not bonded, which served to aid initiation of the delamination process during

testing. The sandwiched specimen was diced to make a 5 mm wide and 50 mm long rectangular beam with thickness of 1mm. Finally, a vertical notch was made on the top Si (100) wafer with a diamond wafering blade to initiate crack propagation during the four-point bending test (figure 3.7(c)). A sideview schematic of a fabricated FPB specimen is shown in figure 3.7(d).

3.3.3 Fabrication of drum resonators

We fabricated a range of SiC (100) membranes without coating, with Ni-Cu coating and with graphene coating on the surface through photolithography and an anisotropic etching technique, DRIE. It should be noted that the membrane fabrication process started from the back side of the wafer (Si surface). To further improve the *Q*, we performed a partial etch-back process of the SiC on a graphene coated SiC (100) membrane (G/ e-SiC (100)) to remove the highly defective bottom part of the SiC film so as to improve the overall crystal quality. SiC etching was also performed from the backside of the sample with DRIE. In summary, we therefore performed the epitaxial 3C-SiC on Si membrane fabrication, using Si surface micro-machining and through photolithography, SiC etching (DRIE), and Si etching (DRIE).

3.3.3.1 Photolithography

Photolithography uses UV light to transfer the pattern of the mask to a light-sensitive chemical called photoresist, deposited on the surface of the wafer. Photolithography was performed to fabricate the graphene coated silicon carbide membranes.

Prior to the start of lithography, we cleaned the wafer piece with acetone, IPA and N_2. The wafer piece was then pre-baked (soft baked) at 126°C for 7 minutes on a hotplate. We initiated the lithography process by coating AZ40XT photoresist using a spin coater to obtain uniform deposition of the resist. The ~25 μm thick photoresist (AZ 40 XT)

was deposited on the backside of the SiC (100) on Si wafer slide through 2300 rotation per minute of the spin-coater. After that, we used EVG620 to print the photomask on the wafer by exposing it to UV light. Next, we developed the mask using AZ 726 developer. AZ40XT, a positive photoresist, becomes soluble in the AZ 726 developer when exposed to UV light. Finally, we hard-baked the wafer at 120°C for 15 minutes using the hotplate, hardening the remaining photoresist before etching. The photoresist acts as a protective mask for the DRIE process and allows the etching of the unprotected circular area of the wafer [240].

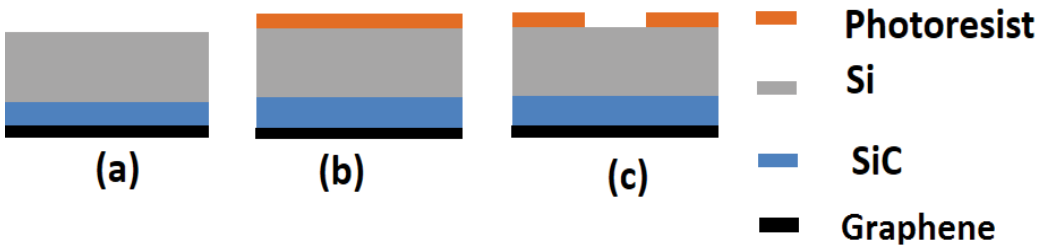

Figure 3.8 Fabricating SiC membranes having radius of 440 µm with an in-situ graphene coating: (a) as grown catalytic graphene on SiC, (b) deposition of the AZ40XT photoresist on the back of the wafer slide, (c) the protective mask of photoresist obtained after the development in AZ 726 developer.

3.3.3.2 Etching

Etching is the process of releasing the structures or removing some regions of the wafer through liquid, gas or ion. In the etching process, the chemical or ion agent removes the topmost layer of the substrate in the unprotected areas i.e. regions having no photoresist. The etching can be performed by either of the two types of movements of the chemical agents or ions: anisotropic or isotropic [240]. The unprotected area in the wafer is etched by using an anisotropic system VersalineTM DRIE (Plasma-Therm, USA) system. For Si and SiC etching, we used Deep Reactive Ion Etching (DRIE) with a flow of 100 sccm C_4F_8 and 150 sccm SF_6 gases.

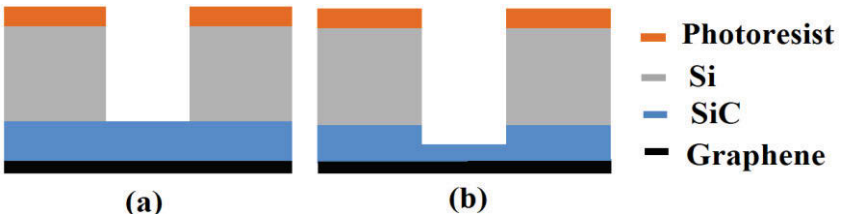

Figure 3.9 (a) Si anisotropic etching by DRIE that use a flow of 100 sccm C_4F_8 and 150 sccm SF_6 gases, (b) SiC anisotropic etching by DRIE with the same gas flow.

DRIE uses the Bosch process that alternates repeatedly between two steps to achieve nearly vertical structures. In the first step, a nearly isotropic plasma containing sulfur hexafluoride (SF_6) ions etches the wafer from a nearly vertical direction. In the second step, octafluorocyclobutane (C_4F_8) plasma provides a sidewall passivation layer that protects the entire substrate from further chemical attack, prevents further etching and provides improved selectivity. Note that during the first cycle repeats, the directional SF_6 ions bombard the passivation layer and sputter it off to expose the substrate to the etchant at the bottom of the trench. This process allows etching of 530 μm of silicon to leave a silicon carbide layer of ~300 nm thickness, as shown in figure 3.9 (a). Thus, we fabricated graphene coated ~300 nm thick SiC membranes (G/SiC) with radius of 440 μm (figure 3.9 (a) and figure 3.10 (a)). To further improve the *Q*, we performed a partial etch-back process of the silicon carbide on an equivalent G/SiC membrane (e-G/SiC) by DRIE (figure 3.9 (b) and figure 3.10(b)). Hence we removed the highly defective bottom part of the silicon carbide film to improve the overall crystal quality. Therefore, we fabricated a range of SiC (100) membranes with graphene coating on the surface (figure 3.10(a) and (b)), without any coating (figure 3.10(c)), and with Ni-Cu coating (figure 3.10(d)) through photolithography and DRIE.

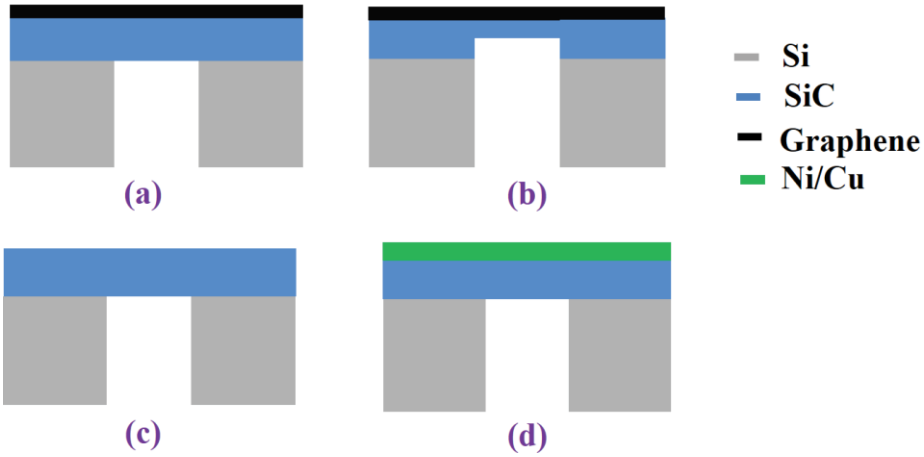

Figure 3.10 Side view schematic of the fabricated samples with radius of 440 µm a) graphene coated silicon carbide membrane, b) graphene coated silicon carbide membrane after backside etching, c) as-grown silicon carbide membrane with no coating, d) Ni-Cu coated silicon carbide membrane.

Removing graphene from SiC

In order to isolate the effect of the graphene coating on the *Q*-factor of the resonator, we used an ashing plasma process where the graphene was oxidised and removed from the silicon carbide wafer. We used Prog 200 reactive ion etching (RIE) system for O_2 ashing to remove graphene from substrates. We performed the etching in a vacuum with 100W RF power, 35 sccm of oxygen plasma for 30 minutes to remove the graphene from silicon carbide substrate and obtained a SiC membrane without graphene.

3.4 Mechanical testing

3.4.1 Four-point bending test

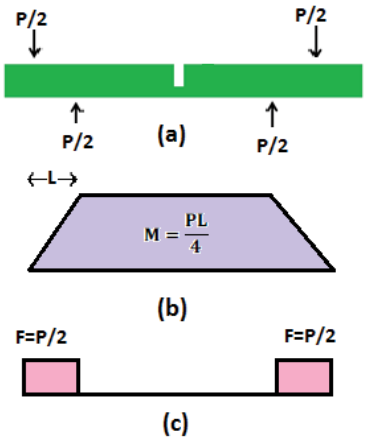

Figure 3.11 (a) A schematic of the four-point bend test system, (b) bending moment diagram and (c) shear force [241].

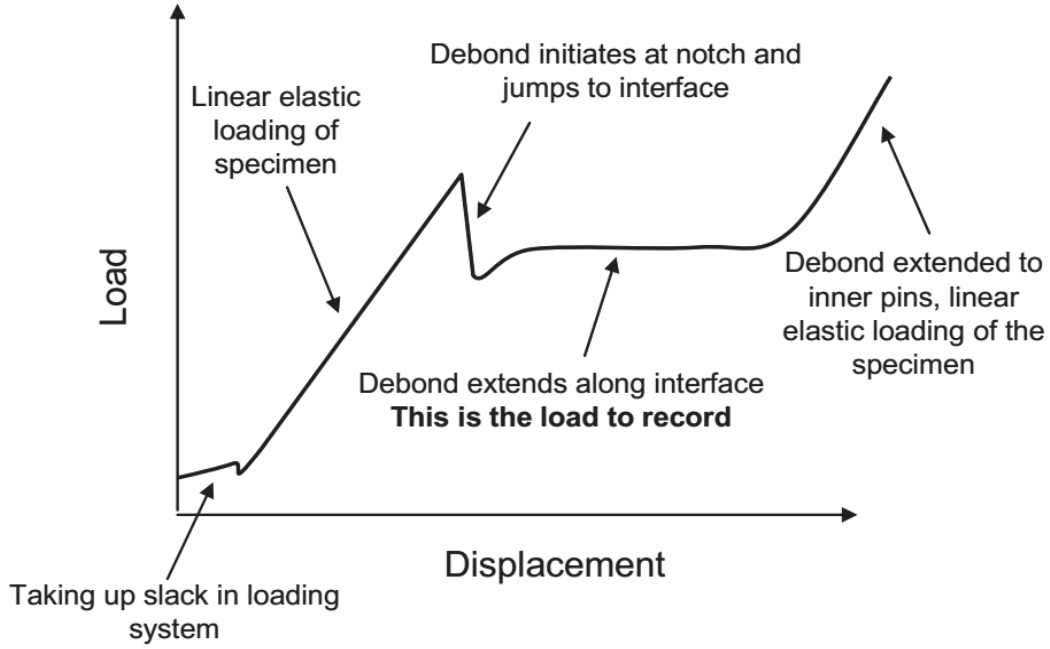

Figure 3.12 Schematic representation of a load-displacement curve for a four-point bending test [242].

For the four-point bending sample preparation, the thin films are sandwiched between two thicker elastic beams and a pre-crack is notched in the top beam. The sample is

placed between four load pins and same load (P/2) is applied to all the four pins (figure 3.11(a)). The initial pressing locks the specimen in place and after that, load increases linearly with displacement, showing the elastic behavior of the sandwiched specimen.

The bending of the beam causes the storing of the elastic strain energy. For four-point bending, there is uniform bending moment between the inner loading points (figure 3.11(b)). The shear force and interlaminar shear stress are zero in the same region which leads to pure bending (figure 3.11(c)). Therefore, elastic strain energy will be stored inside the sandwiched structure. At a certain load, debonding is initiated at top notch and jumps to the thin film/substrate interface. Across a characteristic plateau region, debonding extends in a steady-state manner (figure 3.12) and some of the strain energy is relaxed. This relaxation energy provides a driving force for debonding. From the plateau of the load–displacement curve, the critical load P_c [243] can be extracted for calculating the critical strain energy release rate or interfacial adhesion energy (G_c). If the debonding has extended sufficiently far from the vertical pre-crack (a>2h), then the interfacial adhesion energy (G_c) is independent of the debond length and could be calculated using the following expression [244]

$$G_c = \frac{21(1-\upsilon^2)P_c^2L^2}{16Eb^2h^3} \quad , \tag{3.3}$$

where, the geometrical parameters L, b and h represent distance between inner and outer dowel pins, width of the beam and half height of beam respectively. On the other hand, E and υ stands for Young's modulus and Poisson's ratio for the substrate, respectively.Under conditions of steady state crack growth i.e. in the plateau region, the phase angle of loading (ratio of shear to normal stresses) for the four-point bending test is approximately 43° [244]. The main advantage of the FPB test is that adhesion can be measured without any influence from the crack length; whereas the disadvantage

is the energy dissipation by friction, which leads to slight overestimation of adhesion energy.

3.4.2 Double cantilever beam (DCB) test

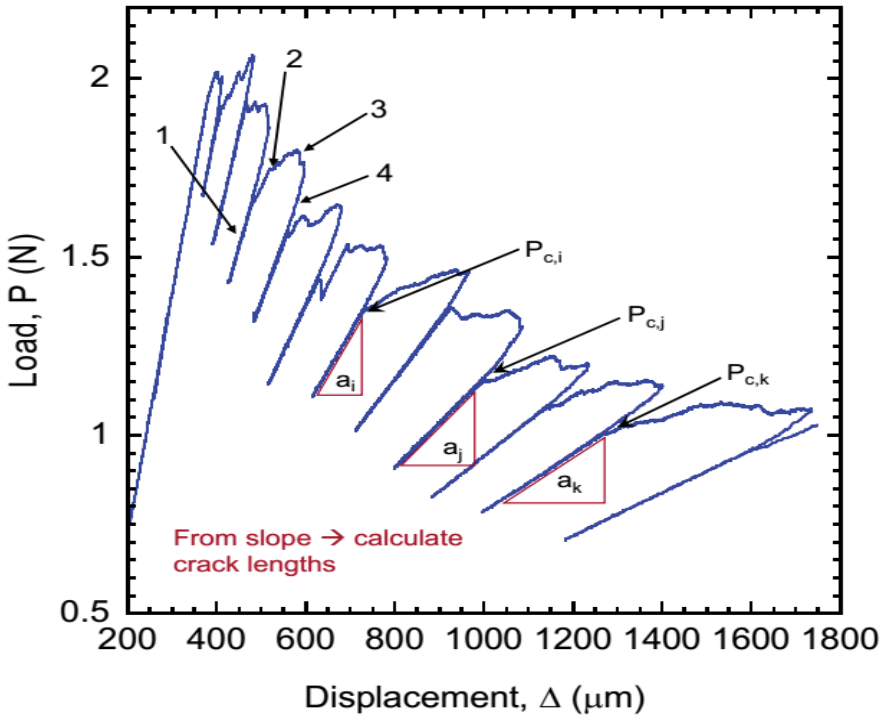

Figure 3.13 A typical load-displacement curve for a DCB specimen [242].

The load-displacement curve for a typical DCB test is shown in figure 3.13. An initial loading was followed by a sharp decrease in load, representing the crack initiation. At a critical value of load, P_c, the load-displacement curve demonstrates a deviation from linearity which indicates the initiation of debonding. With crack extension, specimen compliance changes as seen from the load-displacement curve. In order to measure the specimen compliance, the beams are unloaded and the inverse of the slope of the unloading curve estimates the specimen compliance. The sample is loaded again until further crack propagation occurs, ands this loading/crack growth/unloading cycle is repeated several times [43]. In loading-crack growth-unloading cycles, crack lengths (a_i, a_j, a_k….) are associated with corresponding critical loads (P_{ci}, P_{cj}, P_{ck} ……) (figure

3.13) and each of these (crack lengths, critical load) pairs are used to calculate the associated critical strain energy release (G_{ci}, G_{cj}, and G_{ck}……). In order to record accurate values of P_c, the test data file can be exported to a graphing program that can be used for precise determination of critical loads.

Instantaneous crack lengths of the DCB specimen can be calculated by using the specimen compliance (C), geometry (width, B and half-thickness, h) and plane strain elastic modulus (E') [40],

$$a = \left(\frac{CE'Bh^3}{8} \right)^{1/3} - 0.64h \quad , \tag{3.4}$$

where C = specimen compliance .

From the crack length (a) and the critical load (P_c) at which debond extension occurs, the critical fracture energy or the adhesion energy, G_c (J/m^2) can be measured from [40]

$$G_c = \frac{12P_c^2a^2}{E'B^2h^3}\left(1+0.64\frac{h}{a}\right)^2 \quad , \tag{3.5}$$

The applied phase angle of loading (ratio of shear to normal stresses) for DCB geometry is ~ 0^0. Therefore, the DCB test corresponds to a pure opening mode fracture of interface and only the normal force is associated at the interface.

3.4.3 Membrane resonator optical measurement

We measured membrane resonators out-of-plane flexural Q and f through optical means at room temperature and in a vacuum (below about 10^{-7} mbar). This was performed through a standard all-fibre Mach-Zehnder interferometer [245] setup (figure 3.14) in Warwick Bowen's laboratory, at the University of Queensland.

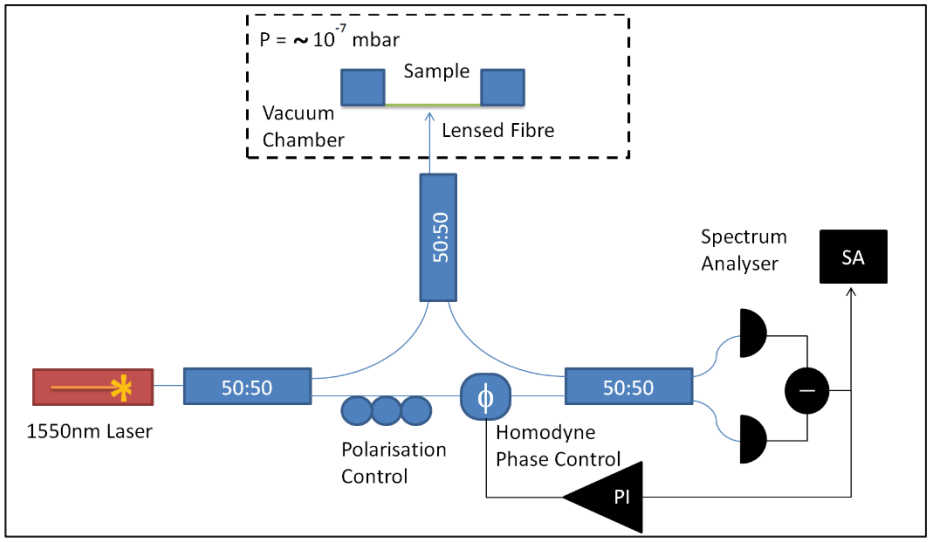

Figure 3.14 Optical measurement setup using Mach-Zehnder interferometer [270].

The sample was mounted and mechanically actuated on an inbuilt piezo-electric modulator of the nanopositioning system [SLC-24 Positioner by SmarAct GmbH].The Mach-Zehnder interferometer was arranged to perform homodyne detection of the light reflected off the sample. A low noise fibre 1550 nm CW laser [Koheras AdjustiK by NKT Photonics] was used to generate around 50 μW of laser light incident on the sample. Of this incident light, 1-2% was then collected using a homodyned and polished lensed fibre at the detectors. We estimated the *Q*-factors using the "free ring down" method [246]. By measuring the time necessary to reduce the amplitude to (1/e) of its initial value of exponential fit, the decay time constant (τ_0) of the ring-down was obtained. *Q*-factor can be calculated from [246]

$$Q = \pi \tau_0 f_0 , \tag{3.6}$$

We measured the circular membrane resonators' out-of-plane flexural *f* and *Q* in a high vacuum at room temperature by using the Mach-Zehnder interferometer and homodyne detection of light as shown in figure 3.14. We performed the *f* and *Q*-factors measurements on SiC(100) membranes, graphene on SiC(100) membranes, and conventional metals (nickel and copper) on SiC(100) membranes in order to investigate

the influence of graphene and metal coating on the resonators' mechanical *f* and *Q*. We also compared the measured frequencies with the simulated frequencies. The results of this experiment are shown in Chapter 5.

3.5 Details of the instruments used

3.5.1 DTS delaminator adhesion test system

The delaminator adhesion test system (DTS Company, Menlo Park, CA) is a high precision micro-mechanical test system with full computer control and data analysis; the system can be used to perform the four-point bending or double cantilever beam adhesion test. The system consists of specialized data acquisition hardware with mechanically stiff load frame around it to hold the sample, as well as to improve testing stability and yield. An actuator permits precise displacement control by the LabVIEW program, whereas a load cell reads the force *P* at each position simultaneously [242].

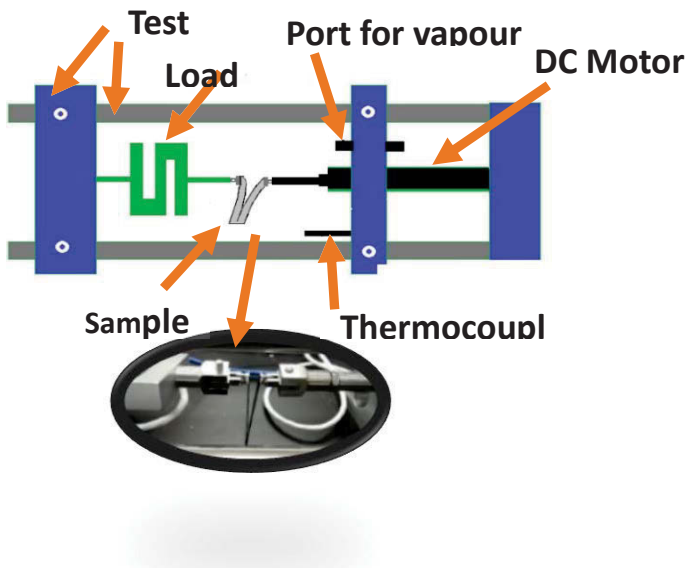

Figure 3.15 Schematic of a DTS delaminator adhesion test system [242].

3.5.1.1 Load cell test frame

A load cell is a transducer that is used to create an electrical signal whose magnitude is directly proportional to the force (*F*) being measured. In our DTS Delaminator, the load cell (Model: SSM-EEX-50) is designed for a maximum load of 222.4 N. It is specially-manufactured, environmentally sealed, have high load precision and temperature compensated. It is mounted in a test frame and equipped with a D-Sub 9-pin connector of which only 4 pins are used to carry the signals to the signal conditioning unit in the delaminator controller. The load cell must be calibrated before the experiment. However, precaution should be taken not to apply any side loads or torque to the load cell during adjustment, calibration or experiment [242].

Table 3.2 Specification for the load cell of the DTS Delaminator (Model: SSM-EEX-50).

Parameter	**Value**
Maximum load	222.4 N (50 lbs.)
Non-linearity	< ±0.05 %FS
Hysteresis	< ±0.03 %FS
Compensated temperature range	-15 to 65^{o}C

3.5.1.2 Load cell calibration

Load cell calibration is the set of operations that compares the accuracy and then aligns the load cell with the standard. The load cell can become less reliable because of a number of reasons such as instrumentation fault, loose cable, electrical or mechanical effect, drift, overuse, mistreatment, ageing etc. Without calibrations, load measurement

readings would become less and less accurate over time, giving us flawed values of force from experiments [242].

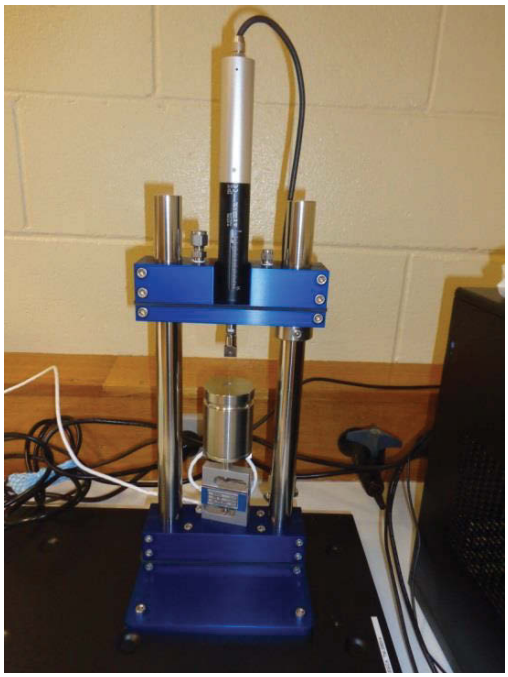

Figure 3.16 Experimental set-up for load cell calibration.

Calibration was verified by carefully putting 1kg weight on the centre of the calibration platform and watching the displayed "Load" value go to 9.82 N. Thus, by calibrating load cell against recognised standard, we ensured that the load cell was performing well and giving the right load value. Then the delaminator was ready to use for future DCB/FPB experiments and for subsequently giving the exact strain energy release rate to get the adhesion of the desired interface [242].

3.5.1.3 Software control

In order to get efficient controlling, data recording and subsequent analysis, the PC is equipped with pre-programmed LabVIEW software. LabVIEW software features an easy-to-use interface allowing minimum test setup time and allows the performing of either DCB or FPB experiments. The only difference in operation is— testing should be performed under tension for the DCB test, whereas FPB testing should be performed

under compression. LabVIEW software enables us to get different graphical information such as load vs. displacement; fracture energy vs. displacement; load vs. time etc. Also different parameters such as loading speed, homing speed, current load, load limit, relative actuator position, data acquisition rates can be adjusted and controlled by the software. The software control also enables the actuator to ramp up the displacement [242].

3.5.1.4 DC motor actuator

The most important hardware component of the system is the high-resolution linear actuator with DC motor (M-235.5DG). The actuator provides linear motion of 50 mm with 0.05 micrometre resolution in a compact package. It consists of a preloaded ultra-low-friction, heavy-duty ball screw which is driven by a precision closed-loop DC motor with motor-shaft-mounted, high-resolution encoder (2048 counts/rev.). The actuator features an extremely low friction construction allowing for minimum incremental motion of 50 nanometres. Contrary to conventional rotating micrometre drives, the M-235.5DG has a non-rotating design that eliminate not only torque-induced positioning and sinusoidal motion errors, but also wear at the contact point and tip-angle-dependent wobble [242].

Table 3.3 Specification for the DC motor actuator of the DTS Delaminator (Model: M-235.5DG).

Parameter	Value
Travel range	50 mm
Minimum incremental motion	0.05 μm
Unidirectional repeatability	0.1 μm
Bidirectional repeatability	1 μm
Maximum velocity	3mm/s
Maximum push/pull force	200 N
Maximum lateral force	100 N (at grip)
Encoder resolution	2048 counts/rev
Motor resolution	20000 steps/rev.

3.5.1.5 Environmental chamber

The test system configuration has an environmental chamber in order to control temperature and humidity. The environmental chamber has two ports, one for vapor injection and another for attaching thermocouple to measure temperature. The environmental chamber is designed to allow operation in temperatures of -20°C to 50°C and in humidity from 0 – 85% R.H. [242].

The environmental chamber enables us to examine the adhesion and the crack growth rate with respect to relative humidity and temperature. We can also conduct DCB experiments in solution, for example in water. Note that the load cell is sensitive to

temperature variation. In order to get stable readings from the load cell, it should be equilibrated to increased temperature prior to testing [242].

3.5.2 Instruments summary

Adhesion testing

Model: Delaminator DTS, Menlo Park, CA

DC motor actuator: Physik Instrumente (PI) M-235.5DG

Load cell: SSM-EEX-50

Software: LabVIEW

Wafer Polisher

Model: Buehler Metaserv 250 Grinder/Polisher

Polishing paper: Allied 600,800 and 1200 Grit Silicon Carbide Paper (8'' disc)

Wafer Dicer

Model: ADT 7100 Dicing System

Wafer Scriber

Model: IsoMet® Low Speed Saw

Raman spectroscopy

Model: Renishaw in-Via Spectrometer

Laser source: 50 mW, 514nm Argon ion laser

Scanning Electron Microscope

Model: ZEISS Supra 55VP SEM

Wafer curvature measurement instrument

Model: TENCOR FLX-2320

Optical profiler

Model: Veeco Wyko NT1100

Lithographic instruments

Brewer Science spin coater: Spinner with 3000 rpm for uniform resist deposition

S. E. M. Hotplates: soft- and hard-bake of the PR

EVG620 mask aligner (MA): UV Mask printing

AZ 726 developer: Developing of the mask after the UV exposure

Si and SiC etcher

Model: Versaline^{TM} DRIE (Plasma-Therm, USA) system

Oxygen plasma

Model: PROG200 Reactive Ion Etcher

CW laser

Model: Koheras AdjustiK by NKT Photonics

Wavelength: 1550 nm

Chapter summary

First, we described the synthesis process of catalytic graphene on silicon carbide on silicon. Afterwards, we described the characterization stages for assessing graphene quality on silicon carbide on silicon; then the characterization stages for failure analysis

of the adhesion tests in order to confirm the delamination along graphene/SiC interface and for viewing the fabrication results of the membrane resonators. We discussed the sample preparation for DCB and FPB adhesion testing. We also discussed fabrication stages (photolithography and etching steps) for membrane resonators. Finally, we discussed adhesion tests for measuring graphene/SiC adhesion, and optical measurement processes to find the mechanical parameters (f and Q) of the resonators.

Chapter 4–Ultrahigh adhesion of epitaxial graphene on SiC on silicon

4.1 Introduction

Graphene is a monoatomic layer consisting of sp^2 hybridized carbon atoms organized into a hexagonal lattice in two dimensions. Graphene is an extremely promising functional material for further miniaturization of electrical [2-4] and mechanical devices [5] with enhanced performance, particularly due to the low power consumption. However, one of the major challenges is the typically low adhesion energy of graphene to other surfaces. Once the adhesion is insufficient in miniaturized devices, graphene can fold or bend due to shearing forces, or be lifted-off due to normal forces during device fabrication or operation, ultimately leading to the failure of such devices [15-17]. For example, the breaking and peeling off of the graphene membrane due to low adhesion with the substrate is a major obstacle for realizing a stable gas separation membrane [18]. Furthermore, graphene/substrate adhesion limits the maximum pressure difference that can be applied to a graphene-membrane gas separator. In addition, to introduce a bandgap by inducing strain in pressurized suspended graphene membranes, the predicted minimum adhesion energy needs to be above 3 J/m^2 in order to prevent delamination [19]. In general, in order to scale up the fabrication of graphene-based functional devices to reliable wafer-level production, it is necessary to ensure high adhesion at the graphene-to-substrate interface.

Most measurements of graphene adhesion reported in literature have been performed by either double cantilever beam (DCB) or blister tests and have been limited to graphene grown by chemical vapor deposition (CVD). For example, CVD monolayer graphene adhesion on seed copper foil, except for one instance [42], has been

consistently reported to be ≤ 2 J/m^2 [40-42] by DCB testing, where the variations in adhesion energy may be attributed to contamination, surface roughness, or trapped liquid [247]. Following the transfer of CVD graphene from seed copper foil to an appropriate substrate for fabricating graphene-based devices, the adhesion energy between graphene and the substrate drops to even lower values. For example, after transferring the CVD graphene onto silicon dioxide substrate, Shin *et al.* [32] reported the adhesion energy as 1.02 J/m^2 by means of a DCB test.

Unlike CVD or exfoliated graphene, graphene grown with a catalytic alloy on silicon carbide [1, 36] is directly grown on silicon substrates (transfer-free) and thus highly relevant to wafer scale fabrication. However, to date, there has been no study of the fracture behaviour nor of the adhesion of graphene on SiC on Si, primarily due to the unavailability of graphene with consistent coverage over large areas of SiC on Si. There is similarly no report of DCB tests to measure graphene adhesion on bulk SiC, likely because of the relative brittleness of SiC wafers which leads to beam fracture at relatively low loads, preventing any meaningful measurement of adhesion. Herein, we discuss our approach for performing the first such measurements. DCB tests are used to evaluate the adhesion of catalytic graphene and we report ultrahigh adhesion energy between the as-grown monolayer graphene and SiC on silicon. Results indicate that metal-mediated catalytic graphene on silicon carbide, one of the most promising methods for synthesizing graphene at large scale for semiconductor applications, also offers a significant improvement in graphene adhesion, potentially enabling multi-step wafer-scale semiconductor fabrication as well as improved device reliability.

Table 4.1 Literature review of the adhesion of graphene on different substrates by Double Cantilever Beam (DCB) and blister testing.

Methodology	Interface	Adhesion Energy (J/m^2)	Author
DCB test	Monolayer graphene on Cu	0.72	Yoon *et al.* [40]
	Graphene/SiO_2	1.02	Shin *et al.* [32]
	Graphene/PMMA	1.58	
	Graphene/PVP	2.31	
	Graphene/Cu	6.0	Na *et al.* [42]
	Graphene/Cu	2.10	Seo *et al.* [41]
	Graphene/Cu	1.54	Na *et al.* [125]
Blister Test	Monolayer graphene on SiO_2	0.45	Koenig *et al.* [45]
	Two- to five-layer graphene on SiO_2	0.31	
	Graphene on Cu	0.34	Cao *et al.* [118]
	Graphene on silicon	0.151	Zong *et al.* [119]
Continuum model along with pleat defect dimension	Trilayer graphene on SiC(0001)	3.0	Wells *et al.*[121]

4.2 Methods

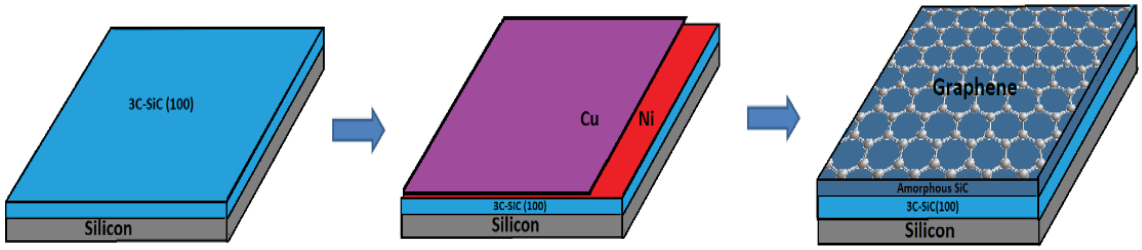

(a) (b) (c)

Figure 4.1 Fabrication process for catalytic graphene, redrawn from [1]. a) The starting epitaxial silicon carbide substrate on silicon, b) Ni and Cu deposition on top of silicon carbide substrate on silicon using e-beam evaporator, c) After annealing at 1100 °C, monolayer graphene forms on epitaxial silicon carbide substrate on silicon. However, an amorphous layer was formed during the graphitization process at the top portion of the crystalline SiC film and below the monolayer graphene.

4.2.1 Alloy-mediated graphene synthesis

A 4-in. (100mm in diameter) Si (100) wafer with an epitaxial layer of cubic SiC (540 nm) was purchased from NOVASIC (France) and used as received. The 3C-SiC/Si wafer was diced into 50x70 mm^2 slides (figure 4.1(a)). Using the Temescal FC-2000 e-beam evaporator, a 13 nm thick Cu layer and a 9 nm thick Ni layer (figure 4.1(b)) were deposited onto these 3C-SiC/Si slides at a rate of 1 – 1.5 Å/sec at a base pressure of 2×10^{-6} Torr. Next, we annealed the sample in a Carbolite HT furnace for 60 min at 1100 °C and ~10^{-3}-10^{-4} mbar for graphitization. The cool down ramp was around 8 hours from 1100 °C to room temperature under a medium vacuum (below~10^{-3}-10^{-4} mbar). After that, we performed wet chemical etching with Freckle's etch solution [36] for metal and metal silicide removal and to get a monolayer of graphene on the SiC (100) (figure 4.1(c)). The samples were cleaned with deionized water and dried by Nitrogen gas flow. TEM suggests the presence of a ~20 nm amorphous and crystalline SiC layer underneath the graphene, as discussed in Section 3.1.

4.2.2 DCB measurements

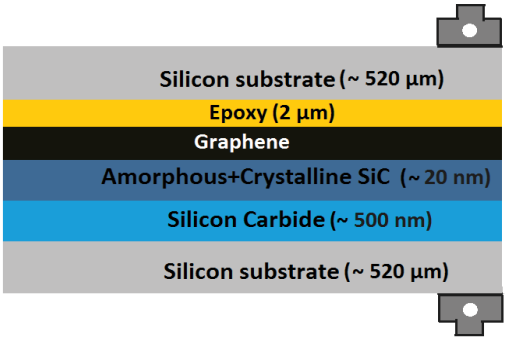

Figure 4.2 Schematic of a sandwiched beam structure containing the graphene on SiC on Si for DCB test of the interfacial debonding energies. The metal tabs are drawn at a higher resolution.

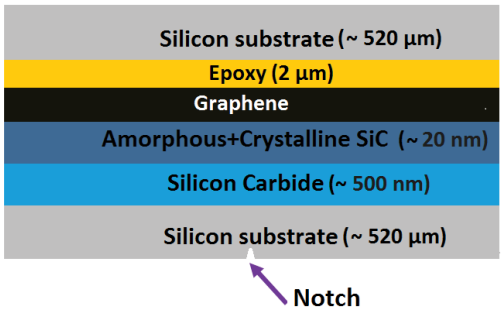

Figure 4.3 Schematic of sandwiched beam structure for four-point bending test.

DCB specimens were fabricated by dicing a 30 mm wide and 50 mm long rectangular section from a catalytic-graphene/SiC/Si wafer and bonding it to a similar sized blank silicon substrate to form a coupon structure (cross-section shown in figure 4.2). A selected epoxy (Epo-Tek 353ND consisting of bisphenol F and imidazole; Epoxy Technology) was used for bonding and the two substrates were attached together with constant clamping pressure (150 kPa), the epoxy then being cured for 1 hr at 125 ^{0}C in a convection oven. This curing process resulted in a 2-µm thick brittle epoxy layer which should contribute marginally to the adhesion energy. Aluminium loading tabs containing low-friction ruby jewel bearings were attached to the DCB specimen to measure the adhesion energy accurately by reducing friction between the loading tabs and pins. A commercial high-strength epoxy (Loctite E-20NS) under high pressure was used to attach the tabs to the DCB specimen [43].

The specimens were loaded in tension under displacement control, and the load, P, versus displacement, Δ, data were recorded as the crack naturally propagated from the

initial crack into the relevant interfaces. All adhesion tests were performed using a thin-film adhesion test system (Delaminator DTS, Menlo Park, CA).

The adhesion energy, G_c (J/m^2), was measured in terms of the critical value of the applied strain energy release rate, G. G_c can be expressed in terms of the critical load, P_c, at which debond growth occurs, the debond length, a, the plane strain elastic modulus, E', of the substrates and the specimen dimensions; width, B and half-thickness, h. The adhesion energy is then typically calculated from [40]

$$G_c = \frac{12P_c^2a^2}{E'B^2h^3}\left(1+0.64\frac{h}{a}\right)^2, \tag{4.1}$$

where,
$$a = \left(\frac{CE'Bh^3}{8}\right)^{1/3} - 0.64h \quad , \tag{4.2}$$

where, C = specimen compliance .

4.2.3 Four-point bending measurements

Specimens for four-point bend adhesion measurements were prepared from 50 mm squares cleaved from graphene/SiC/Si wafers and subsequently bonded to a blank silicon substrate of similar size using epoxy (figure 4.3). In this case, a central region (~5mmx50mm) is not bonded and serves to aid initiation of the delamination process during testing. The sample coupons were then cured at 120 °C for 1 hr. Individual four-point bend specimens were diced from the sandwiched coupon using a dicer blade such that dimensions of each beam were 5 mm x 50 mm x 1 mm. Using a diamond scribe, a central notch was made in the centre of the substrate beam, centred over the initiation region. The beam was then loaded for four-point bending while the load (P) was monitored and the displacement (Δ) was controlled. The four-point bending adhesion measurements were taken at a displacement rate of 0.5 μm/s.

Initially, the composite structure was loaded elastically, storing strain energy within the elastic substrates. Eventually, the notch initiated debonding in the SiC/graphene/Si

stack. At a critical load (P_C), the strain energy release rate became larger than the fracture resistance of the graphene/SiC interface, resulting in debond extension along the graphene/SiC interface and the load plateau. Using simple beam mechanics, the interface fracture energy can be written as [244]

$$G_c = \frac{21(1-\nu^2)P_c^2 L^2}{16E'b^2h^3} \quad , \tag{4.3}$$

where E' is the plane strain modulus of the substrate, and the dimensions L, b, and h are distance between inner and outer dowell pin, width of the beam and half height of the beam, respectively.

4.2.4 Surface analysis

We assessed the quality of the graphene using a Renishaw InVia micro-Raman system with an excitation wavelength of 532 nm. A Digital Instruments Dimension 3100 atomic force microscope (AFM) was used to measure the topography of the sample before and after delamination; data was then analysed using the NanoScope Analysis 1.7 software. A Zeiss Supra 55VP scanning electron microscope (SEM) at the University of Technology, Sydney, was used to collect SEM images. The chemical bonding and composition of the surface of the samples was assessed by XPS using a Specs 150 SAGE instrument operated with a Mg K_α X-ray source (Mg anode operated at 10 keV and 10 mA).

4.3 Results

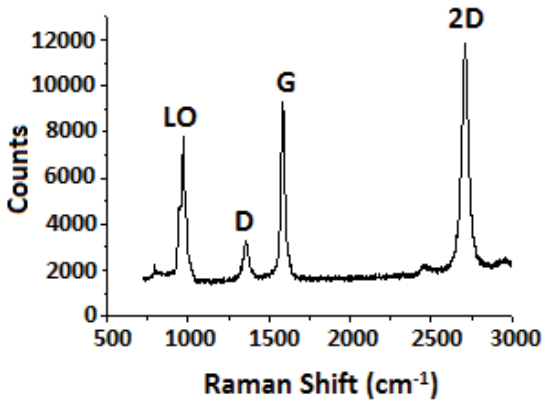

Figure 4.4 Raman spectrum of the graphene on silicon carbide film on silicon. Raman spectra of a graphene on SiC showing the LO, D, G and 2D peaks at ~971, 1355, 1585 and 2710 cm^{-1}. D, G and 2D are characteristic graphene peaks whereas the longitudinal optical (LO) peak response is originated in the cubic silicon carbide layer underneath.

4.3.1 Characterization of graphene on SiC on Si before substrate bonding

Our experimental conditions are equivalent to those in Mishra *et al*. [39], who suggest a ~20 nm thick mixed phase of oxidized amorphous and crystalline SiC under the atomic layer of carbon, based on the time of flight secondary ion mass spectrometry (ToF-SIMS), transmission electron microscopy (TEM) and X-ray photoelectron spectroscopy (XPS) measurements. In the amorphized layer, some of the Si–C bonds are replaced by an oxycarbide (C-Si-O) bond during the graphitization [1, 39]. Figure 4.4 shows the Raman spectrum of the as-grown catalytic graphene on SiC film with the graphene D-band (at ~1355 cm^{-1}), G-band (at ~1585 cm^{-1}), 2D-band (at ~2710 cm^{-1}) and silicon carbide longitudinal optical (LO) peak (at ~971 cm^{-1}). The higher intensity of the 2D-band compared to G-peak intensity $I_{2D}/I_G \approx 1.2$ and the transmission electron microscopy (TEM) image suggest the presence of monolayer graphene [39]. The I_D/I_G ratio is as low as 0.29-0.32, indicative of a material with a low density of defects.

Averaging over several scanning areas of 20 μm×20 μm, the root mean square roughness of the graphene on a 3C–SiC sample was ~29nm, which is about threefold

that of bare 3C–SiC films grown on silicon substrate (~ 9nm) (see supplementary information, figure S1, for AFM line scan profiles).

4.3.2 Fracture data

4.3.2.1 DCB result

Two DCB specimens were constructed from the sandwiched wafers, one of which demonstrated a nice force-displacement curve containing multiple loading/crack growth/unloading cycles, whereas the other sample fractured through the thickness of

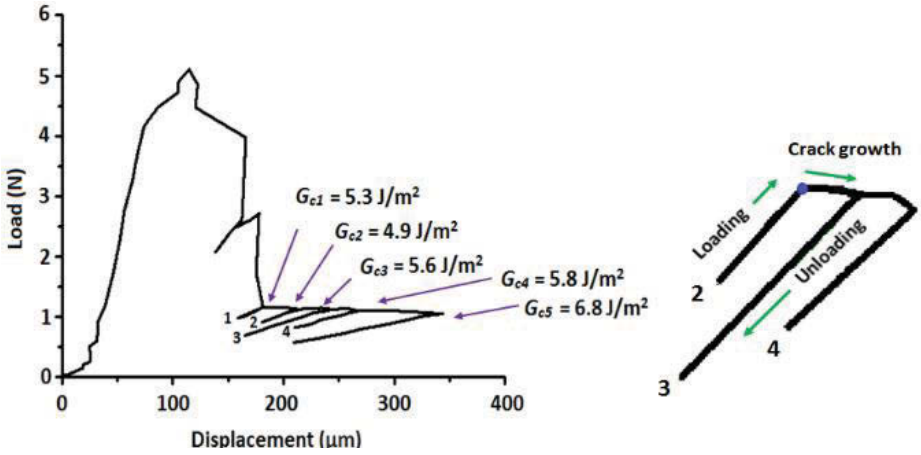

Figure 4.5 a) Load displacement curve for DCB Test, b) part of figure (a) demonstrating a loading-unloading cycle.

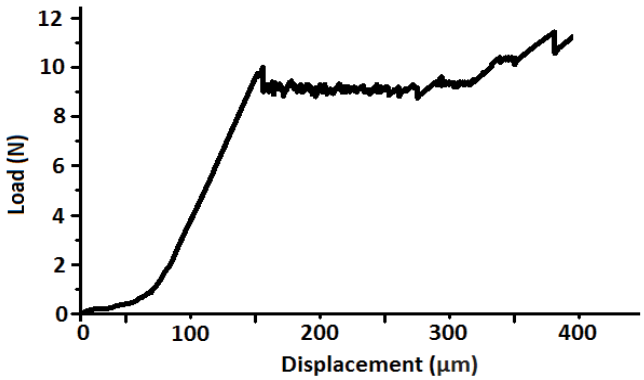

Figure 4.6 Load displacement curve for a four-point bending test.

the beam prior to delamination. The load-displacement curve for the successful DCB test is shown in figure 4.5(a). An initial loading was followed by a sharp decrease in

load, indicating crack initiation. A loading/crack growth/unloading cycle is shown in figure 4.5(b). The loading of the beam leads to a critical load at which the load starts to decrease, exhibiting changes in specimen compliance with crack extension. The beams were subsequently unloaded to measure the compliance (from inverse of slope), then loaded again until further crack propagation occurred, and this cycle was repeated several times [43]. Instantaneous crack lengths of the DCB specimen could be calculated from Equation (4.2) using the specimen compliance, geometry and plane strain elastic modulus. From the crack length and the critical load at which debond extension occurred, the critical fracture energy could be measured (using Equation (4.1)). The average fracture energy of the observed interface using DCB test was found to be 5.7±0.7 J/m^2.

4.3.2.2 FPB result

The interfacial adhesion energy for the SiC/graphene was obtained by putting the average plateau load in the formula for critical strain energy release rate, equation (4.3). The near-steady state energy release rate plateau corresponds to an average debonding energy of 7.6 J/m^2. This value seems in very good agreement with that found from DCB testing, as we note that the higher loading mode in FPB (~ 45 degree phase angle as compared to the pure opening mode of DCB) leads to a higher dissipation component in the FPB measured values. As the layered stack is essentially brittle, but we do have a substantial interfacial roughness at the interface between SiC and graphene, we expect that the slightly higher measured value in FPB is mostly due to interfacial friction upon debonding, rather than plastic dissipation. Note finally that although only one successful measurement may not be considered statistically significant, the extremely well-defined plateau acts as a collective measurement of adhesion energy at every

given point along the delaminated specimen surface, and furthermore the good agreement with the DCB values confirms accuracy of the measurement.

Four-point bending tests suffered from lower test yield due to substrate fragility. Among ten samples, six samples broke sharply, showing no plateau during the four-point bending test. Two samples delaminated on one side of the notch and therefore were not considered reliable measurements. The two remaining samples delaminated on both sides of the notch, only one of which demonstrated an extended and reliable plateau related to a steady-state energy release rate, typical of an interfacial debonding. Figure 4.6 represents the load displacement curve and the plateau of the successful four-point bending test.

4.3.2.3 Reference

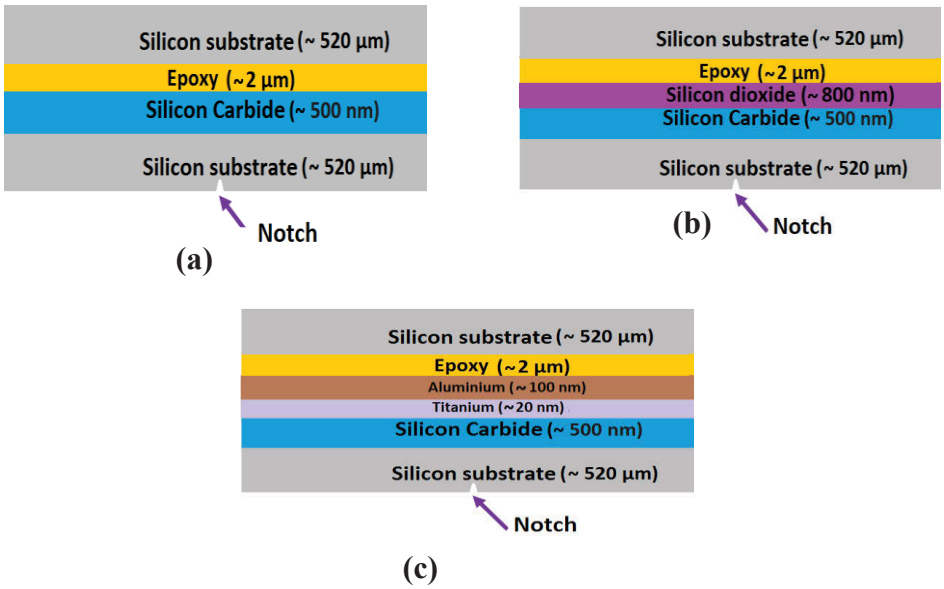

Figure 4.7 Schematic of sandwiched beam structure of the references, a) silicon carbide on silicon, epoxy-bonded to blank silicon beam (Si/SiC/Epoxy/Si), b) silicon dioxide deposited atop silicon carbide on silicon, epoxy-bonded to blank silicon beam (Si/SiC/SiO_2/Epoxy/Si), c) aluminium/titanium adhesion-promoting layers deposited atop silicon carbide on silicon, epoxy-bonded to blank silicon beam (Si/SiC/Ti/Al/Epoxy/Si.)

To probe the adhesion energy of the SiC/Si interface prior to graphitization, a series of reference samples were prepared, as indicated in figure 4.7. Note that figure 4.7(a) is the same structure as seen in figure 4.3, except the samples were not graphitized. In each case, a different bonding scheme is used, with SiO_2 and Ti/Al layers added in figure 4.7(b) and 4.7(c) respectively, in an effort to drive crack delamination into the SiC/Si interface. Results of the four-point bending tests performed on these specimens are presented in Table 4.2.

In each of the Si/SiC/Epoxy/Si and Si/SiC/SiO_2/Epoxy/Si specimens tested, we were unable to propagate a crack through any layer via a four-point bending test, instead observing crack propagation through the thickness of the beam (Table 4.2).Upon addition of Ti/Al layers atop the SiC, we were able to perform a single valid four-point bending test, likely enabled by the additional plasticity in the metal layers, which gave an adhesion energy of 43 J/m^2 at the SiC/Ti interface (Table 4.2) (see Supplementary information, figure S8 for the corresponding plateau and figure S9, for XPS scan of two delaminated sides). Overall, these results indicate that prior to graphitization, the SiC/Si reference structures (figure 4.7) lack a low-energy interface to allow crack propagation prior to beam fracture, and strongly imply a high adhesion energy between SiC/Si.

Table 4.2 Results of four-point bend tests performed on reference Si/SiC structures.

Stack	**Number of samples tested**	**Number of samples with valid results**	**Delaminated Interface**	**Adhesion energy (J/m^2)**
Si/SiC/Epoxy/Si	11	0	None	
Si/SiC/SiO_2/Epoxy/Si stack	10	0	None	
Si/SiC/Ti/Al/Epoxy/Si stack	10	1	SiC/Ti	43

4.3.3 Failure analysis for DCB

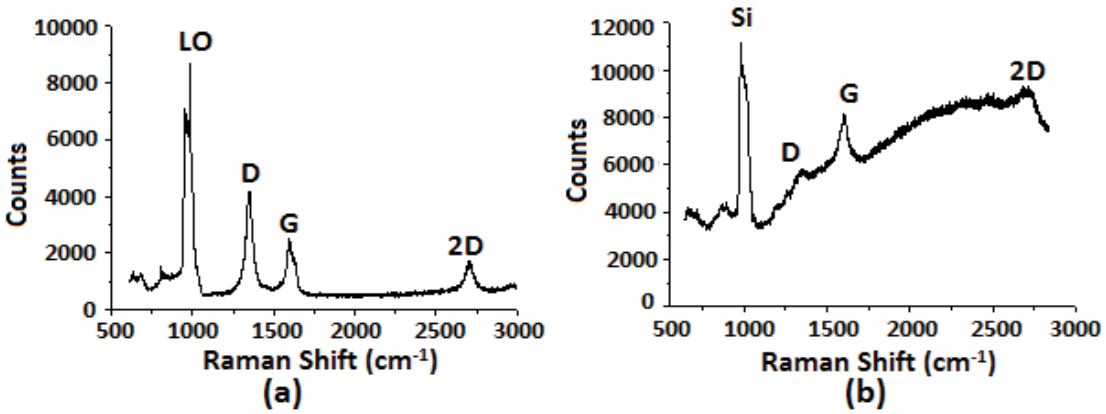

Figure 4.8 Raman spectra of the debonded graphene/SiC interface (a) side 1 (graphene/SiC side) and (b) side 2 (epoxy/graphene side).

Following adhesion measurements, the delaminated interfaces were diagnosed using Raman spectroscopy, XPS, SEM and AFM to confirm the location of the debonding path.

4.3.3.1 Raman

Figures 4.8(a) and 4.8(b) show the Raman spectra of side 1 and side 2 of the debonded interface. Side 1 has a silicon carbide longitudinal optical (LO) peak at 981 cm^{-1} in addition to a graphene D peak at ~1354 cm^{-1}, G peak at ~1586 cm^{-1} and 2D peak at ~2702 cm^{-1}; therefore, it will be termed the graphene/SiC side. The very high D peak (figure 4.8) compared to that on the initial graphene on SiC sample (figure 4.4) represents an abundance of defects.

On the other hand, the Raman spectra of the 'side 2' of the delaminated interface contain silicon peak at 977 cm^{-1} and graphene D peak at ~1353 cm^{-1}, G peak at ~1602 cm^{-1} and 2D peak at ~2706 cm^{-1}, verifying the presence of the graphene on the epoxy. In 'side 2', the graphene peaks are masked by the contributions from the epoxy fluorescence underneath; therefore we will term it as the graphene/epoxy side.

4.3.3.2 XPS

We performed XPS measurements on both sides of the debonded beams (figure 4.9) and the XPS spectra shows the deconvolution of the XPS C1s peaks from the debonded graphene/SiC interface (a) graphene/SiC side and (b) epoxy/graphene side.

Here, we focussed on the three strongest peaks. For the SiC side, the relative bonding ratios were 24.6 % carbon sp^2 bonding (the peak at 284.1 eV), 62.6 % SiC (the peak at

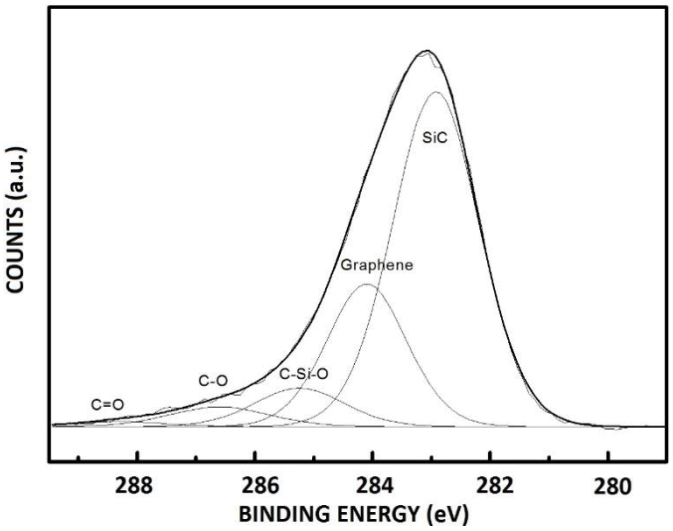

(a)

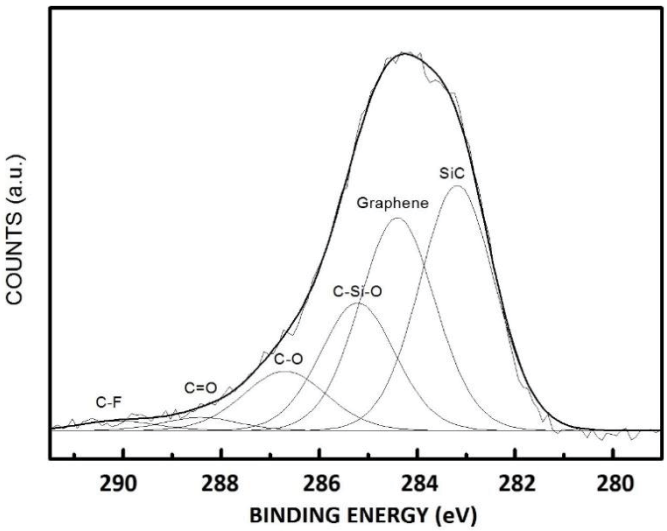

(b)

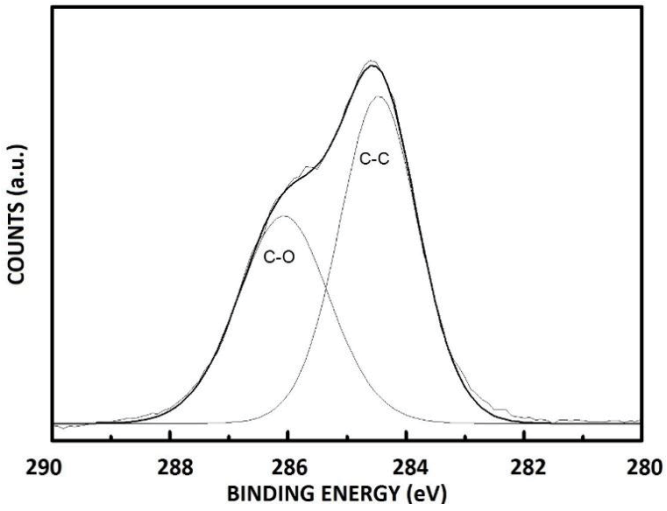

(c)

Figure 4.9 The XPS of the debonded graphene/SiC interface (a) graphene/SiC side, (b) epoxy/graphene side and c) the XPS of Epo-Tek 353ND (~2 mm epoxy).

283.0 eV) and 7.5% C-Si-O (the peak at 285.3 eV) (figure 4.9(a)). For the epoxy/graphene side, the relative bonding ratios were 30.8% carbon sp^2 bonding (the peak at 284.5 eV), 34.9% SiC (the peak at 283.2 eV) and 18.6% C-Si-O (the peak at 285.3 eV) (figure 4.9(b)). Therefore, XPS of the fracture sections demonstrated the presence of graphene, SiC and C-Si-O on both sides of the fracture.

As a reference, we also performed XPS measurements on ~2 mm thick epoxy. Figure 4.9(c) depicts the C1s XPS spectra which was split into two distinct peaks (284.5 eV, 286.1 eV), which are attributed to the sp^2 carbon and the carbon in C–OH bonds, respectively. Neither the SiC nor the C-Si-O peak, which are two major peaks in figure 4.9(b), are present in epoxy. Therefore, in figure 4.9(b), only the peak attributed to graphene would have some contribution from the epoxy.

4.3.3.3 SEM

The SEM image of the graphene/SiC side of the delamination indicates some micrometre-sized depressions, potentially corresponding to micrometre-sized hillocks on the opposite side (epoxy/graphene side). Since the XPS indicates the presence of SiC on epoxy/graphene side, we conclude that these micrometre-sized depressions correspond to the pull-out of SiC by a fraction of strongly adhered graphene and the corresponding hillocks represent the transfer of SiC patches on the epoxy/graphene side (see supplementary information, figure S2).

4.3.3.4 AFM

As for the SEM image, the AFM scans also reveal micrometer-scale hillocks on the epoxy/graphene side, with corresponding depressions being observed on the SiC/graphene side of the interfacial fracture. AFM depth profiles demonstrate that the height of the hillock is of the same order magnitude as the depth of the depression, and both are between 20-40 nm. Since the 20 nm of amorphous and crystalline SiC is present underneath the catalytic graphene [39], as discussed in section 4.3.1, we conclude that the transfer of a fraction of amorphous and crystalline SiC occurred from SiC/graphene side to graphene/epoxy side (see supplementary information, figure S3, for AFM line scan profiles of the two sides).

The RMS roughness parameter from 20 μm × 20 μm region scans is ∼18 nm on both sides after fracture (SiC/graphene side and Epoxy/graphene side). Notably, the RMS roughness of the delaminated sides is lower than that of the starting graphene/SiC sample itself, which was ∼ 27 nm and therefore it can be concluded that surfaces have been smoothed by the fracture process.

4.4 Discussion

Most studies on the adhesion of graphene are related to CVD graphene; for example CVD graphene adhesion on Cu seed [40-42, 118] and on SiO_2 substrate [32, 45, 125] have been studied by means of both DCB and blister testing. Although numerous studies have investigated the adhesion of CVD graphene on Cu foil and on SiO_2 substrate, little has been reported on the adhesion of an as-grown graphene. Therefore, a rigorous study of the adhesion energies of graphene and SiC substrate and its fracture behaviour is critical for any graphene-based device fabrication. We attempted in an earlier work to evaluate the adhesion of graphene/SiC (111) with four-point bending testing, but could only conclude that the adhesion energy of the directly-grown graphene to be sensibly higher than the transferred one, as failure analysis was inconclusive [1].

In this paper, we employed DCB and FPB tests, which are more reliable and reproducible than most other adhesion measurement techniques. For both of the tests, the required energy for delamination and the measured adhesion energy are well defined with minimal influence from residual stress of the thin film [115]. Here we report that the adhesion of graphene grown on SiC on Si– is 5.7 ± 0.7 J/m^2 as measured by DCB testing. In addition, we report adhesion energy as high as 7.6 J/m^2 using a four-point bending test. Since the DCB specimen was loaded under pure opening mode (phase angle = 0^0), the shear stress and frictional force do not contribute to the measurement. Therefore, the measured fracture energy in the DCB testing estimates a lower boundary of adhesion of the graphene/SiC interface. On the other hand, under conditions of steady state crack growth (in the plateau region), the phase angle of loading (ratio of shear to normal stresses) for a four-point bending test is approximately 43° [244]. In the four-point bending test, in contrast with a DCB test, the shear stress

and associated frictional force play a role in addition to the normal stress. Therefore, the additional energy dissipation through friction leads to a slight overestimation of adhesion for the four-point bending test.

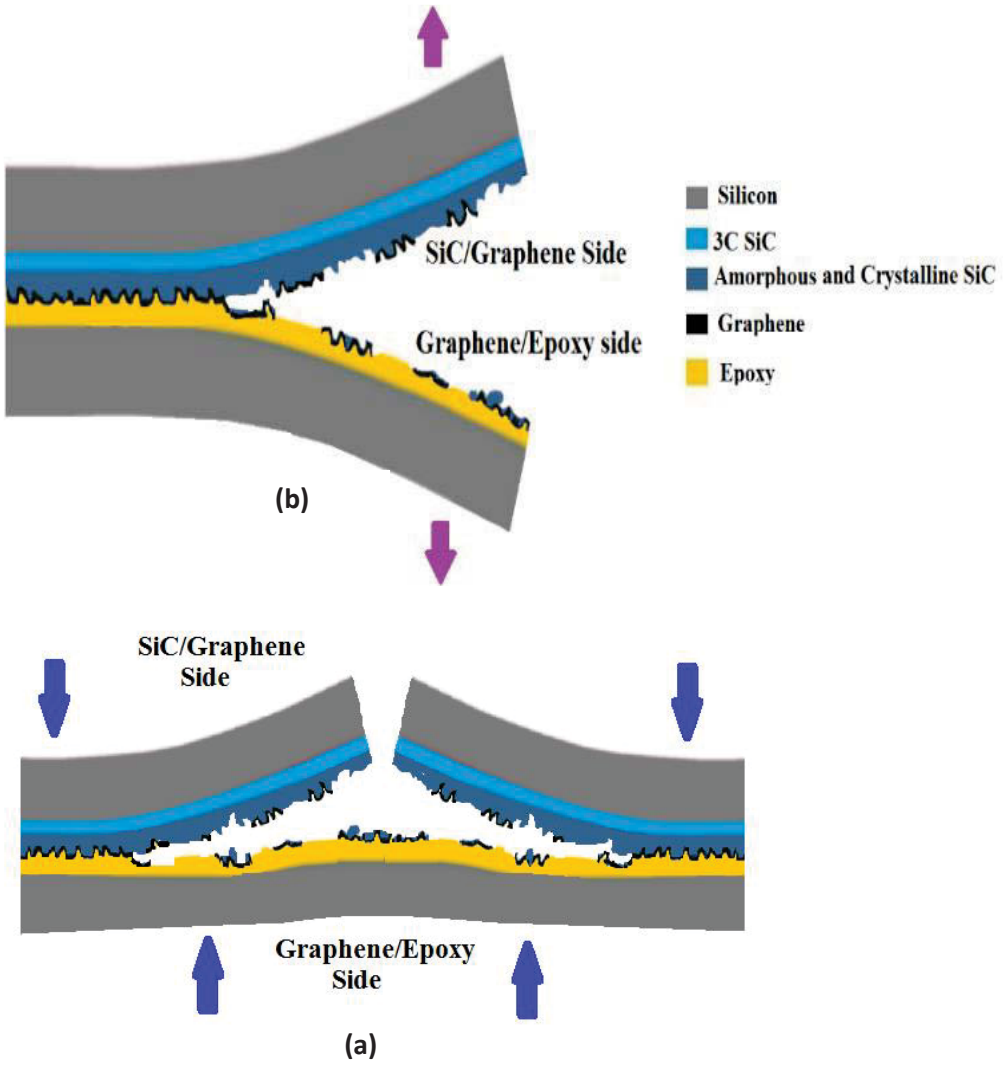

Figure 4.10 Schematic of interfacial fracture of highly rough graphene/SiC interface by a) a DCB test and b) a four-point bending test.

Since the XPS spectra suggested the presence of SiC on the epoxy/graphene side, we performed SEM and AFM in order to further investigate the debond path. SEM micrographs demonstrate the presence of depression in the SiC/graphene side and associated hillocks in the graphene/epoxy side, with sizes in the order of micrometers. The depth profiles by AFM indicate that the depth of the depressions and the height of the hillocks are between 20-40 nm; the same order of the thickness of the mixed amorphous and crystalline SiC layer present underneath the monolayer graphene [39]. The presence of a highly rough amorphous layer (RMS roughness is ~29 nm) along with the relatively high graphene/SiC adhesion may be responsible for the occasional pull-out of fractions of amorphous/polycrystallyne SiC material attached to a graphene grain, or groups of grains, as depicted in the schematic in figure 4.10.

The Raman spectra and XPS demonstrate the presence of graphene on both sides of the fracture which imply that the graphene domains, with average domain size of around 35 – 60 nm [39], have been distributed on both side of the fracture. These individual domains would have little variation in adhesion energy with some of the domains adhering strongly to the SiC substrate underneath and possibly debonding from the epoxy.

While the epoxy conforms to the graphene, the high roughness (RMS roughness was around ~29 nm) would lead to micro voids at epoxy/graphene interface. Therefore, there is no contact between the epoxy and graphene where these micro voids are present and consequently graphene remains on silicon carbide after the fracture of the interface. Na *et al.* [42] also proposed micro-voids at the graphene/epoxy interface and as a result, some graphene domains could not be transferred from Cu to epoxy because of these micro-voids. Dauskardt *et al.* [244] also investigated the fracture of the TiN/ SiO_2

interface which was highly rough and observed that SiO_2 is present on both sides of the fracture.

Unlike thermally decomposed graphene on SiC (0001), no buffer layer [121] is present between SiC(100) and catalytic graphene [39]. We propose that the observed high adhesion is correlated with 1) the high roughness of the SiC surface after graphitization and 2) the presence of chemical bonding at the interface, formed during the graphene growth.

The high roughness (RMS roughness is ~29 nm) of the SiC surface is likely due to the diffusion of nickel into the SiC layer at high temperature (1100^0C) [36] and the subsequent formation of an intermixed layer of metal silicides [39] which were eventually removed by wet etch. This rough SiC surface underneath the graphene results in a larger effective area of interfacial contact, leading potentially to a higher adhesion as measured by DCB. Na *et al.* [42] have attributed the high Cu/graphene adhesion (6 J/m^2) to the high roughness due to scratches and undulations scattered in Cu foil and to the overall high roughness of Cu foil (RMS roughness ~20 nm). However, the surface roughness should lead to a pronounced additional frictional component in the FPB testing, of which we did not obtain strong evidence. This is potentially because the delamination occurs by shearing off some of the highly interlocked regions, as demonstrated by the AFM and SEM failure analysis.

An additional likely reason for the substantially higher graphene adhesion we observe is the formation of chemical bonds at the interface between graphene and electronegative oxygen in amorphous silicon carbide. XPS depth profiling exhibits 35 at. % oxygen in the first 5 nm of depth, which includes the graphene and top SiC layer [39]. A similar type of bonding between amorphous SiO_x surfaces and graphene has been reported by Das *et al.* [126] and Rodrigues *et al.* [56].

The Van der Waals bonding associated with exfoliated/transferred graphene is not sufficient to hold large-scale graphene on a single-crystal dielectric silicon substrate. If the adhesion between substrate and graphene is as low as in the case of exfoliated or CVD graphene, poor graphene-substrate adhesion [40, 45, 118, 119] will lead to shorter lifespan, break structural stability and result in unreliable performance. Moreover, the insufficient adhesion would render the wafer-level fabrication of electronic, photonic, mechanical, optoelectrical or electromechanical devices extremely challenging. Direct (in-situ) growth of graphene grown from silicon carbide on silicon [1, 36] can overcome these limitations and high adhesion energies of good quality monolayer graphene will pave the way toward large scale wafer level production of highly reliable graphene-based devices.

4.5 Conclusion

We have, for the first time, directly measured the adhesion energy of large-area monolayer graphene as-grown on a silicon carbide substrate on silicon by DCB and four-point bending tests. In both cases, the transfer of monolayer graphene domains were confirmed by failure analyses such as Raman spectroscopy and XPS. DCB geometry was used to determine mode I fracture toughness (phase angle 0^0) whereas FPB was used to determine mixed mode fracture toughness (phase angle approximately 43^0). The DCB test, with phase angle 0^0, was used to determine mode I fracture toughness and the estimated adhesion energy of graphene grown on SiC on silicon was 5.7 ± 0.7 J/m^2. The four-point bending test estimated adhesion energy as high as 7.6 J/m^2. Therefore, we conclude that the adhesion energy between graphene and silicon carbide is strongly dependent on the fracture mode-mix. The higher measured adhesion in four-point bending test can be attributed to the energy dissipation through friction.

We believe that the measured high adhesion of catalytic graphene on SiC on Si is correlated with the highly rough SiC surface under the graphene that increases the effective area for bonding and also due to the chemical interaction between the electronegative oxygen atom of oxidized amorphous SiC and carbon atom of graphene layer [56]. Our study demonstrates that the in-situ catalytic graphene as-grown on silicon carbide on silicon offers fivefold improvement over the adhesion of CVD or exfoliated graphene on silicon or silicon dioxide substrate. High adhesion energies of catalytic graphene will ensure reliability of micro- and nano- graphene-based devices over long period and will pave the way to realise large scale, wafer level production of graphene-based devices.

Supporting Information of:

Ultrahigh adhesion of epitaxial graphene on SiC on Si

1. AFM line scan profile of SiC surface before and after graphitization

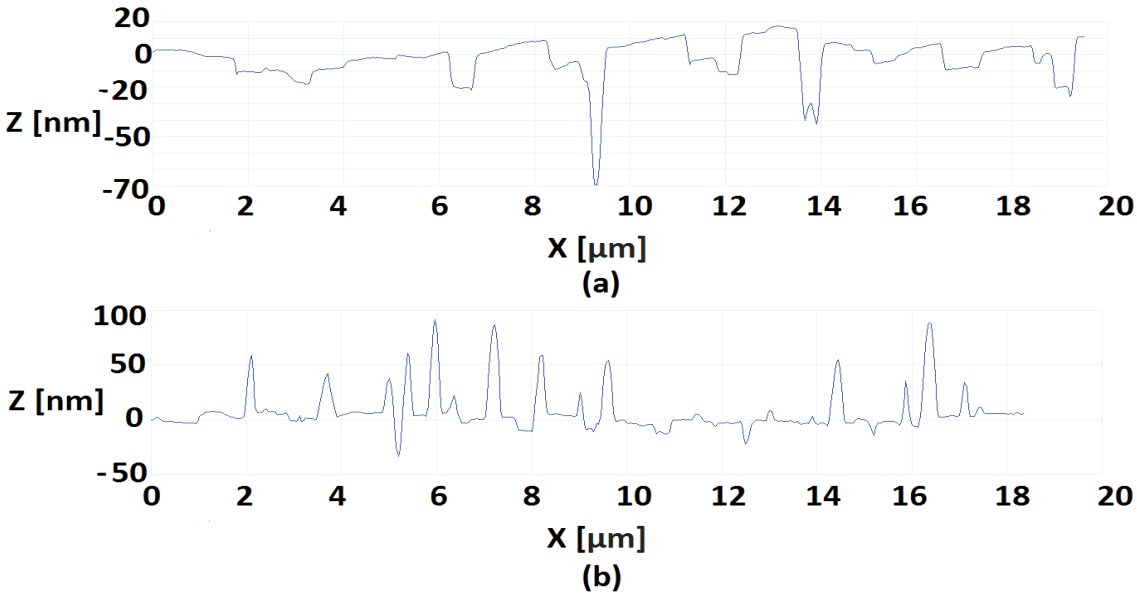

Figure S1 AFM line scan profiles of (a) as-grown silicon carbide film on silicon and (b) graphene on silicon carbide film on silicon.

2. Failure analysis for DCB test

2.1 SEM

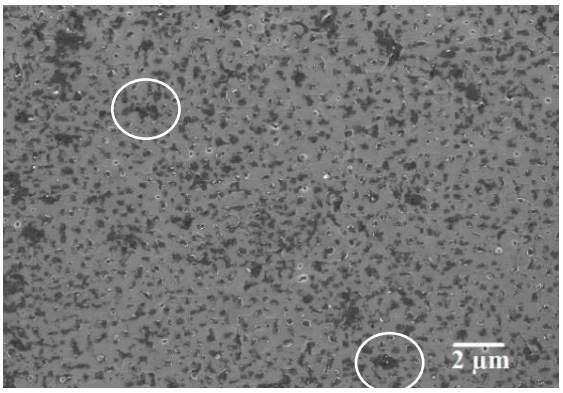

(a)

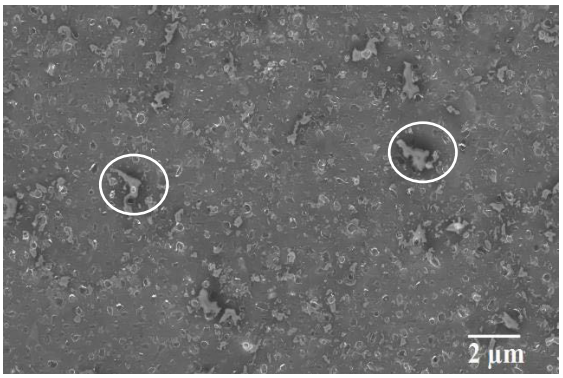

(b)

Figure S2. The SEM image of the fracture structure of graphene/SiC interfacial region following the DCB test (a) graphene/SiC side and (b) epoxy/graphene side.

2.2 AFM

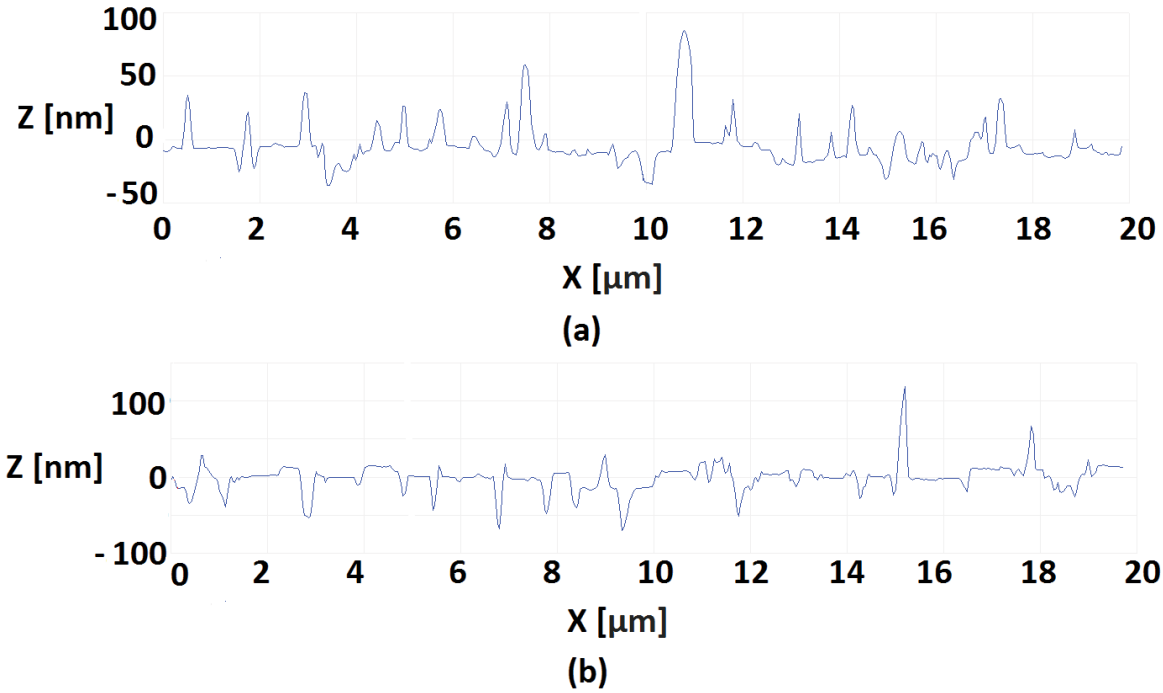

Figure S3. The AFM line scan profiles of the fracture structure of the SiC/graphene interface after the DCB test, (a) SiC/graphene side, (b) graphene/epoxy side.

3. Failure analysis for FPB test

Failure analysis suggest that the debonding path in a four-point bending test is similar to that of the DCB test.

3.1 Raman

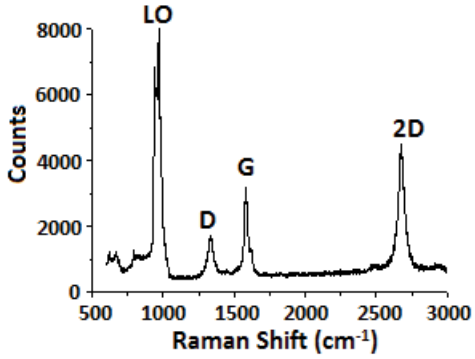

(a)

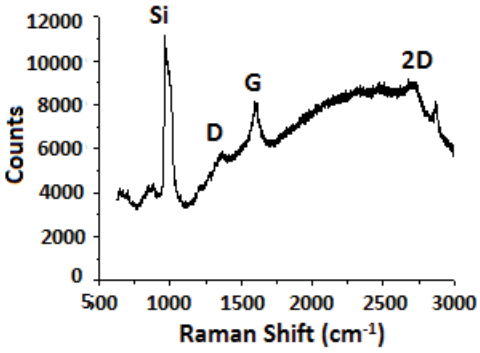

(b)

Figure S4 The Raman spectra of the debonded graphene/SiC interface (a) side 1 (graphene/SiC side) and (b) side 2 (epoxy/graphene side).

3.2 XPS

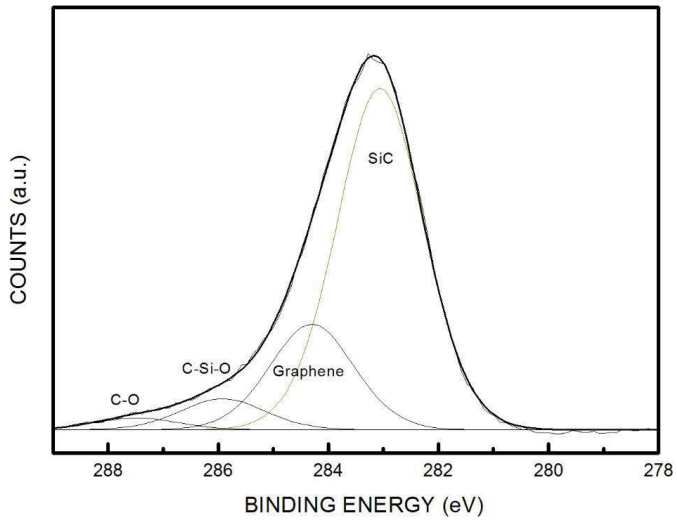

(a)

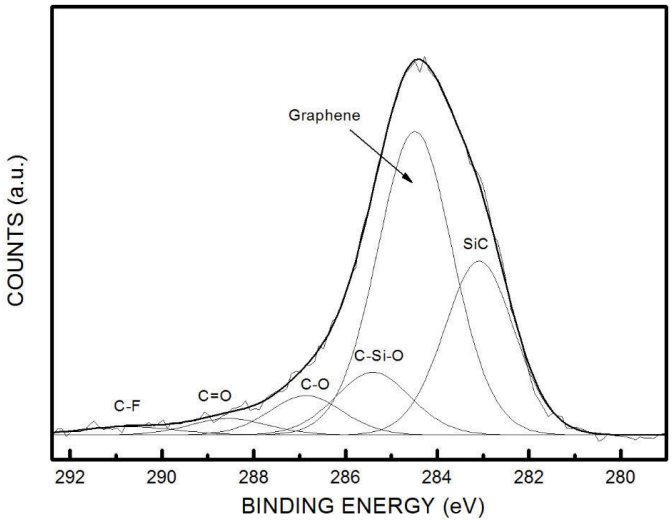

(b)

Figure S5. The XPS of the debonded graphene/SiC interface (a) graphene/SiC side and (b) epoxy/graphene side.

3.3 SEM

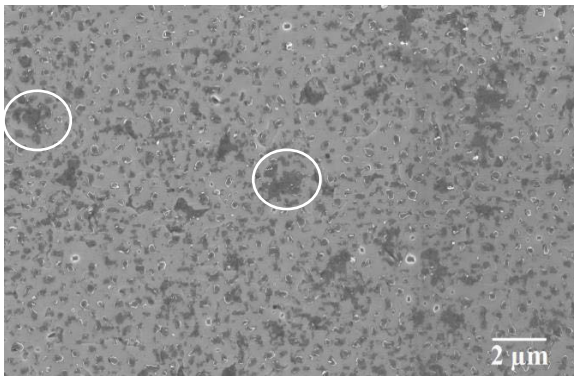

(a)

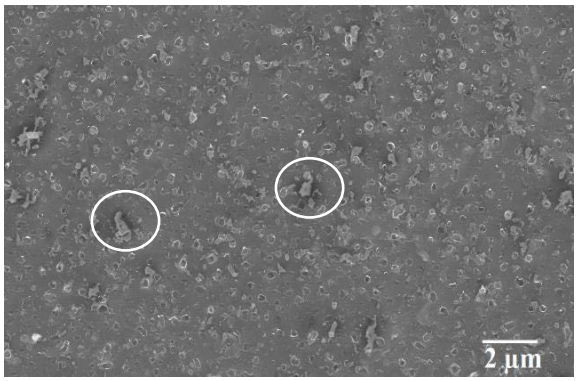

(b)

Figure S6. The SEM image of the fracture structure of the graphene/SiC interfacial region (a) graphene/SiC side and (b) epoxy/graphene side.

3.4 AFM

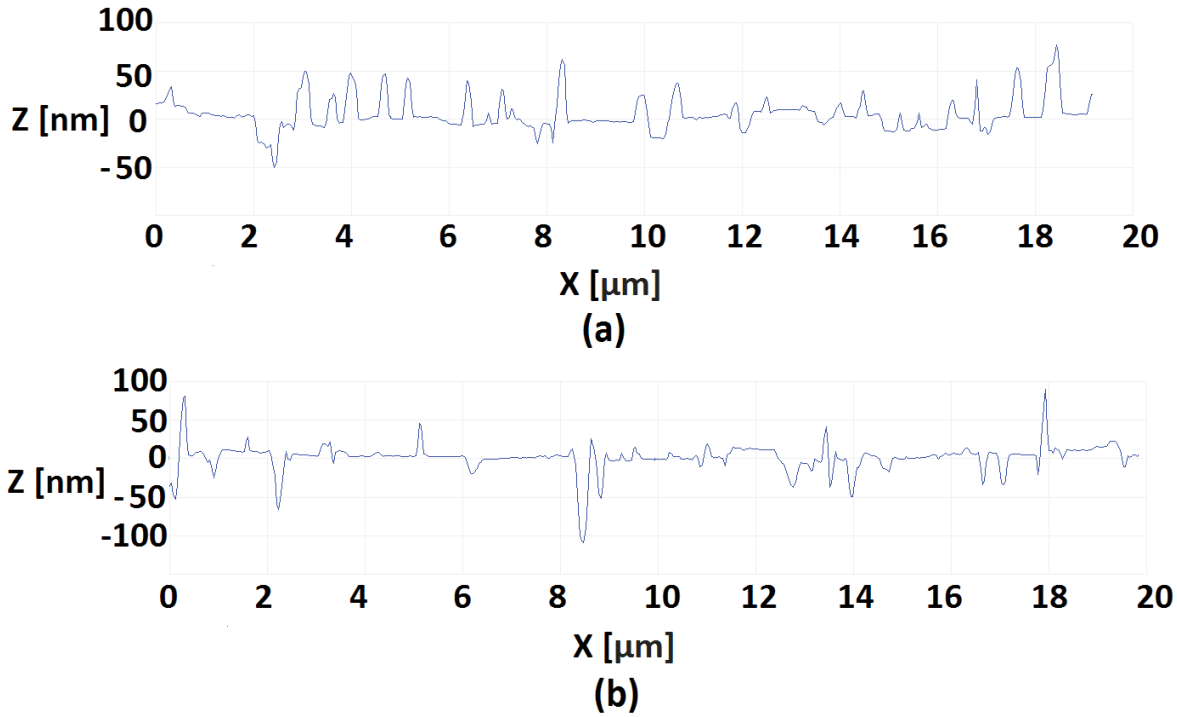

Figure S7. The AFM line scan profiles of the fracture structure of the SiC/graphene interface, (a) SiC/graphene side, (b) graphene/epoxy side.

4. Reference

4.1 The successfully delaminated sample plateau

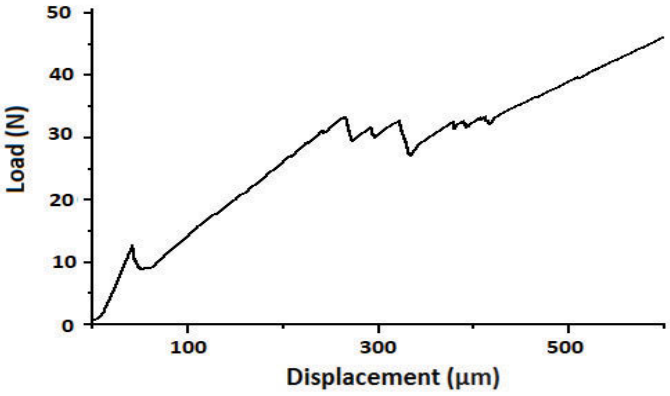

Figure S8. The successfully delaminated sample plateau for Si/SiC/Ti/Al/Epoxy/Si stack.

4.2 Failure analysis of delaminated sample

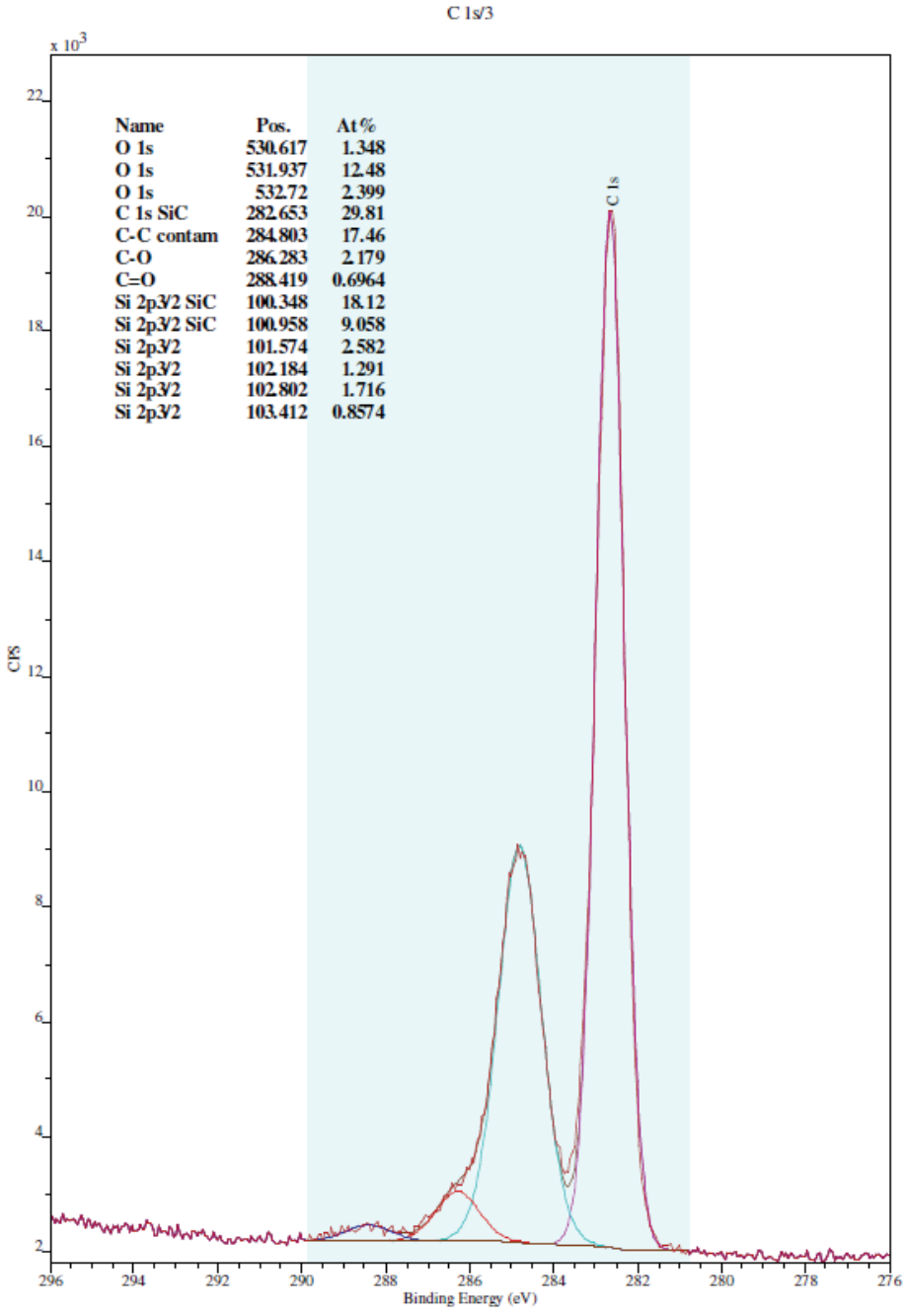

(a)

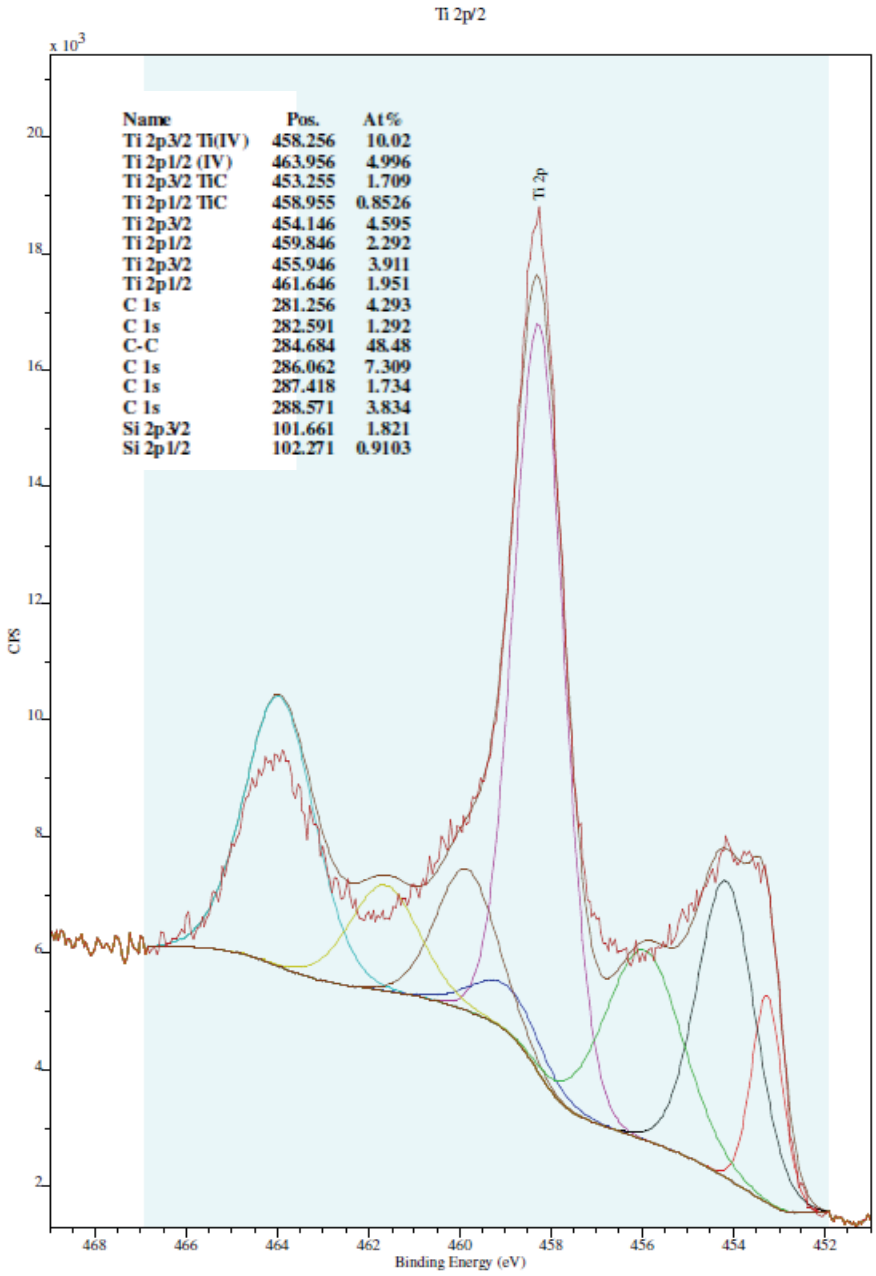

Figure S9. a) The XPS of successfully debonded reference sample for Si/SiC/Ti/Al/Epoxy/Si stack a) SiC side and b) Ti side.

(b)

4.3 Load displacement curve representing breaking of the beam without any plateau

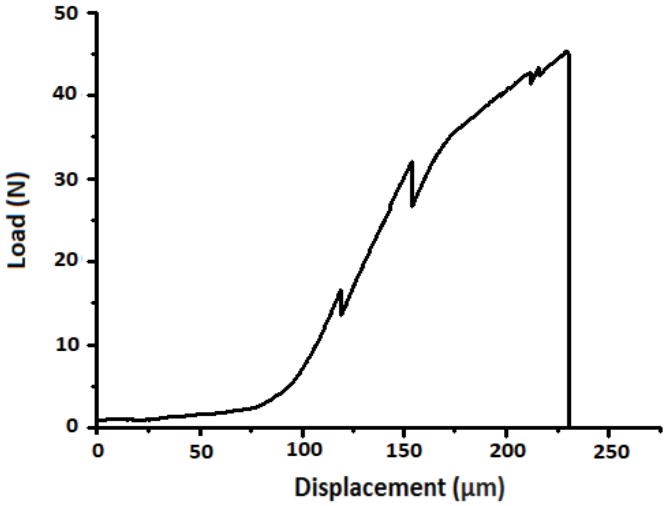

(a)

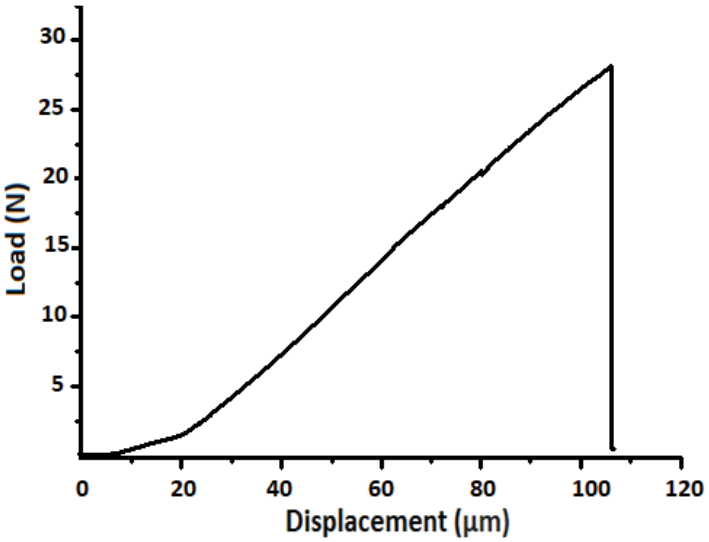

(b)

Figure S10 (a) and (b) Examples of the measurements representing breaking of the beam without any plateau, likely due to the absence of low-adhesion interface.

Chapter 5–Mechanical Performance of Graphene on Cubic Silicon Carbide Membrane Resonators on Silicon

5.1 Introduction

Epitaxial cubic silicon carbide (3C-SiC) on silicon (Si) is an outstanding mechanical material and can act as a solid carbon source and template for the direct growth of graphene, allowing for easier fabrication and higher adhesion between graphene and silicon carbide (SiC), as compared to graphene transferred on silicon nitride. We have reported the adhesion energy of 5.7 J/m^2 between graphene and SiC (chapter 4), which is fivefold higher than that of transferred graphene on SiO_2 [32].

Microresonators are an excellent platform for realizing miniaturized gravimetric biological/chemical sensors with very high sensitivity [152, 156]. Epitaxial SiC, having high thermal conductivity, electrical stability, resistance to radiation, Young modulus to density ratio and hardness, is suitable for use at high temperatures and in harsh environments [156, 248-251]. 3C-SiC on silicon Si is one of the most promising material candidates for mass resonant sensing applications due to its excellent mechanical properties, tunable tensile stress and easy fabrication [250, 252]. The factors that influence the sensitivity of the resonators are the mechanical quality factors (Q) and natural resonant frequencies (f_0) [253]. Our research group has shown that very high frequency×quality factor ($f_0 \times Q$) values (~10^{12} Hz) can be achieved through epitaxial SiC microstrings, exceeding the state-of-the-art silicon nitride (Si_3N_4) strings [168]. Our research group has also closely analyzed the factors influencing this product, including material properties, resonator geometry, clamping, and ambient pressure [44].

For the electrical actuation and readout of the SiC membrane resonator, a deposition of a conductive layer on top is necessary. However, it is well-known that the addition of even a thin conventional metal layer on the microresonator surface results in a considerable *Q* reduction and increased mass [254]. For example, a *Q* reduction of at least four times was reported from the metallization of Si_3N_4 through conventional metal layers of 5 nm thickness or above [255]. This damping can be mitigated by removing the metal from the resonator's clamping regions, but with the cost of adding difficulty to the fabrication and integration steps [256].

Novel materials need to be used as efficient conductive layers in order to reduce the metal damping due to plastic dissipation in conventional metals [257]. Graphene, as the thinnest, strongest and most conductive material available, is well suited for microelectromechanical systems (MEMS), and for the actuation and readout purposes of the micro-resonator [149, 155, 162, 171, 258]. Lee *et al.* [257] have shown that CVD graphene could be used as a metal replacement on a silicon nitride (Si_3N_4) membrane resonator surface and that the *Q* of the silicon nitride (Si_3N_4) membrane is only mildly degraded (~30% reduction). However, the reported adhesion of CVD graphene after transferring to different substrates is reported to be between 0.151 to 1.02 J/m^2 [32, 40, 45, 118, 119], which is not sufficient for wafer level fabrication of graphene coated membrane resonators.

As-grown graphene, with superior adhesion compared to CVD graphene, is a suitable coating material for replacing the metal coating in mechanical resonators for actuation and readout purposes. However, no work has been done to investigate the influence on the *Q*-factor when as-grown graphene is present on a SiC membrane resonator. In this article, for the first time, we make a comparison between the *f* and *Q* of uncoated SiC membranes, transfer-free monolayer graphene on SiC membranes, and a conventional

metal layer on SiC membranes of similar geometries. We illustrate how the use of graphene as a metal replacement can help to reduce the damping of conventional metals. This research is significant since both SiC [259, 260] and graphene [261] have a very high degree of biocompatibility and can hence be used for biosensing.

5.2 Materials and methods

5.2.1. Materials

3C-SiC films were deposited on a Si(100) wafer in a hot-wall horizontal low-pressure chemical vapour deposition system at 1000 °C, using propene and silane gases [262]. The film thickness was measured using a Veeco Wyko NT1100 optical profilometer with a 1Å resolution, assuming a refractive index of 2.65 for epitaxial SiC [263]. We measured the Young's modulus of a 1µm thick SiC film to be 330 GPa using Hysitron Triboindenter nanoindentation [264]. We also measured the residual mean stress of SiC with a Tencor Flexus 2320 curvature measurement system with nm resolution via a SiC etch-back process, as explained in our previous work [265, 266].

The metallic and graphene (G) layers were deposited or grown on SiC prior to the lithography stages. We produced monolayer graphene (G/SiC) with a thickness of ~1 nm on SiC films using our previously reported alloy-mediated (nickel and copper) catalytic approach [1, 36]. We first sputtered a double layer of Ni (thickness: 9 nm) and Cu (thickness: 12 nm) on the SiC surface. Next, we annealed the sample in a Carbolite HT furnace for 60 min at 1100 °C and ~10^{-3} -10^{-4} mbar for graphitization. Finally, we performed wet chemical etching [36] for metal removal and to obtain monolayer graphene on the SiC. We assessed the quality of the graphene using a Renishaw InVia micro-Raman system with an excitation wavelength of 514 nm.

5.2.2. Fabrication

We fabricated a series of membranes denoted as SiC, Ni-Cu/SiC, G/SiC and G/e-SiC respectively, as explained in Table 5.1.

Table 5.1 Description of each type of fabricated silicon carbide membrane.

Name of the Membrane	Description
SiC	Silicon carbide membrane that has no coating or overlayer.
Ni-Cu/SiC	Silicon carbide membrane with metal (nickel and copper) overlayer.
G/SiC	Graphene coated SiC membrane where no etching on SiC has been performed.
G/e-SiC	A thinner silicon carbide membrane with a graphene coating. The 'G/SiC' membrane transforms into 'G/e-SiC' membrane after etching is performed.

We first synthesized the graphene on 1x1 cm^2 wafer slide of SiC (100) on Si, as shown in figure 5.1(a) and explained in Section 5.2.1. Then, the ~25 μm thick photoresist (AZ 40 XT) was deposited on the back side of the wafer slide (figure 5.1(b)) and developed using a mask (figure 5.1(c)). The resulting photoresist pattern acts as a protective mask during the DRIE process. The unprotected area in the wafer was etched using the Versaline^{TM} DRIE (Plasma-Therm, USA) system, using C_4F_8 and SF_6 as reactive gases. This process allows the etching of 530 μm of silicon so as to leave a silicon carbide

layer of ~300 nm thickness, as shown in figure 5.1 (d). Thus, we fabricated graphene coated ~300 nm thick SiC membranes (G/SiC) with radius of 440 µm (figure 5.1(d) and figure 5.2(a)). To further improve the *Q*, we performed a partial etch-back process of the silicon carbide on an equivalent G/SiC membrane (G/e-SiC) by DRIE (figure 5.1(e)). This removed the highly defective bottom part of the silicon carbide film to improve the overall crystal quality (figure 5.1(e) and figure 5.2(b)). Subsequently, in order to isolate the effect of the graphene coating on the *Q*-factor of the resonator, the catalytic graphene coating was removed by 35sccm O_2 plasma treatment for 30 min to obtain a SiC membrane without graphene (figure 5.1(f)).

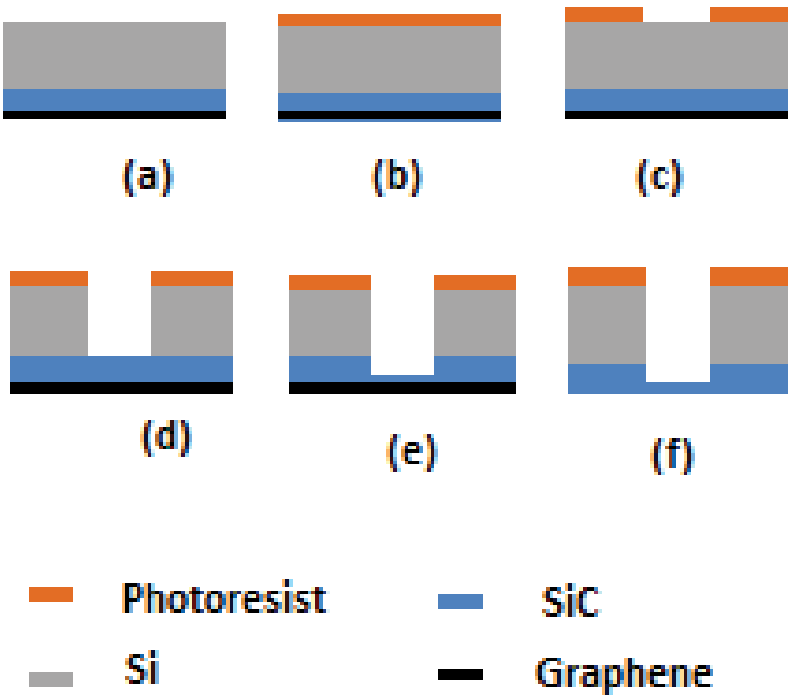

Figure 5.1 Fabricating SiC membranes with radius of 440 µm with an in-situ graphene coating: (a) as-grown catalytic graphene on SiC, (b) deposition of the photoresist on the back of the wafer slide, (c) the protective mask of photoresist obtained after the development, (d) Si anisotropic etching by DRIE, (e) SiC anisotropic etching by DRIE, (f) last step—the removal of the graphene from a partially etched graphene coated SiC membrane using O_2 plasma.

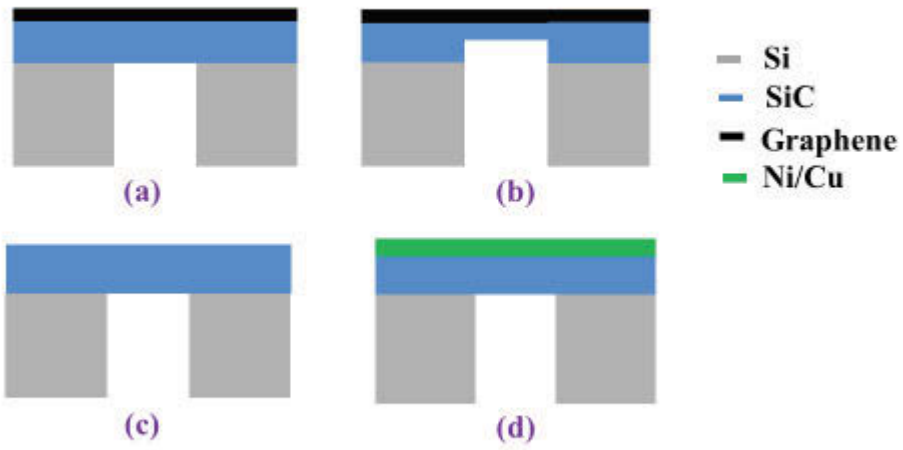

Figure 5.2 Side view schematic of the fabricated samples with radius of 440 µm a) Graphene coated silicon carbide membrane, b) Graphene coated SiC membrane after backside etching. c) Silicon carbide membrane, d) Ni-Cu coated SiC membrane.

Figure 5.2 shows the side view schematic of all membranes with radius of 440 µm, fabricated by using the lithography steps as in figure 5.1 and using DRIE. Figures 5.2(a) and 5.2(b) are equivalent to figures 5.1(d) and 5.1(e) respectively. We fabricated a 300 nm thick SiC membrane without coating (figure 5.2(c)). Likewise a 300nm thick Ni-Cu/SiC membrane was prepared by depositing a 20 nm thick Ni-Cu overlayer on top of 280 nm thick silicon carbide (figure 5.2(d).

In order to compare the mechanical properties of graphene coated resonators, we also fabricated SiC membranes with radius of 1500 µm. By DRIE, 530 µm of silicon was etched for fabricating ~ 540 nm thick SiC membranes of radius of 1500 µm (figure 5.10(a)). A partial etch-back DRIE process was used to fabricate 270 nm thick SiC (e-SiC) membrane (figure 5.10(b)) and graphene coated ~ 270 nm thick SiC (G/ e-SiC) membrane (figure 5.10(c)) with radius of 1500 µm.

5.2.3. FEM simulation

We simulated the fundamental out-of-plane mode *f* of the silicon carbide membranes through finite element modelling (FEM) analysis, using the COMSOL Multiphysics software. We input silicon carbide properties, including our experimentally measured Young modulus and residual gradient stress, density of 3.21 gcm^{-3}, and Poisson's ratio value of 0.267 [250, 267] into the COMSOL Multiphysics software for this purpose. We also added the measured residual gradient stress by subdividing the SiC membrane model into multiple layers according to our measured stress profile, as shown in [265].

5.2.4. Optical measurements

The fundamental out-of-plane mode mechanical resonance *f* measurements were performed at room temperature under vacuum (~10^{-7} mbar) using all-fibre Mach-Zehnder optical interferometry (figure 5.3) [268] with piezo-electric actuation. The *Q* factors were collected using the free ring-down method [269] as described elsewhere [44].

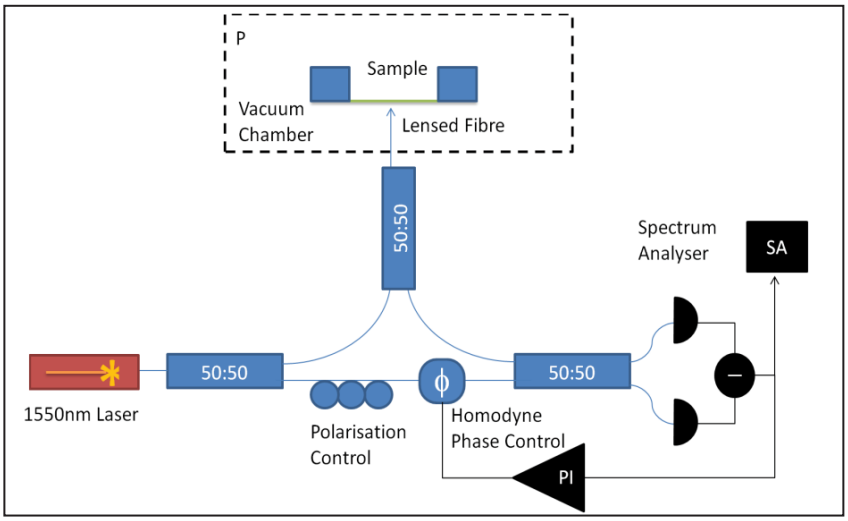

Figure 5.3 Optical measurement setup using Mach-Zehnder interferometer [270].

5.3 Results

Figure 5.4 shows the Raman spectrum of the as-grown catalytic graphene on SiC (100) film with the graphene D-band (at ~1355 cm^{-1}), G-band (at ~1584 cm^{-1}) and 2D-band (at ~2708 cm^{-1}). The higher intensity of 2D-band, compared to G-peak, intensity (I_{2D}/I_G = 1.2) and the transmission electron microscopy (TEM) image, suggest the presence of monolayer graphene [1, 33].

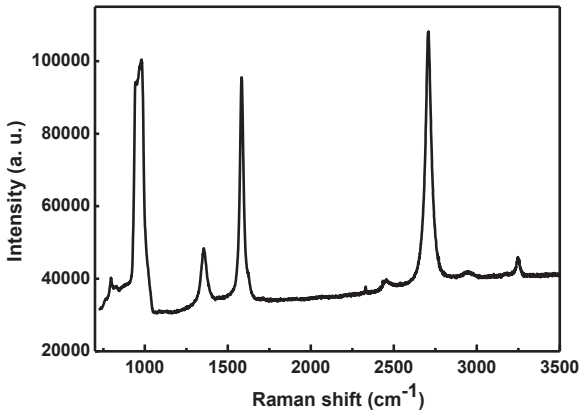

Figure 5.4 Raman spectroscopy of graphene on SiC film.

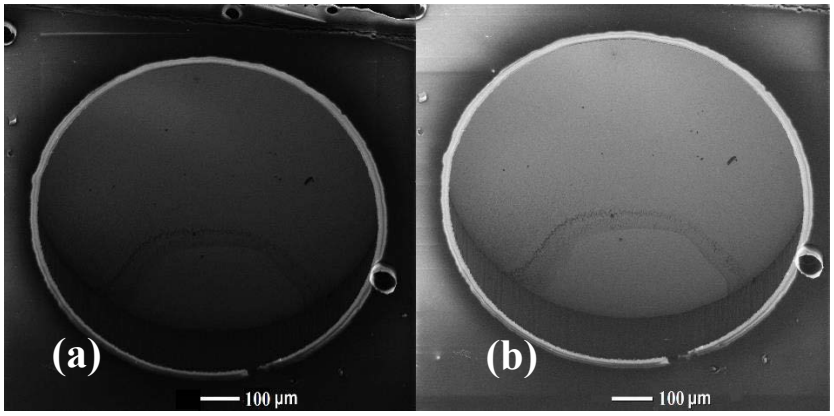

Figure 5.5 SEM images of G/SiC(100) membrane a) Top view and b) Tilted view.

As mentioned previously, the membranes were released through an anisotropic Si backside etching process, DRIE. The steep profile and the sharp edge (figure 5.5) of the membranes are attributed to the anisotropic nature of the DRIE process, and are better than the rounded etching profile of silicon in the vicinity of the SiC membrane

when isotropic etching such as XeF_2 is used [271]. Therefore, perfect clamping was achieved and energy dissipation from the clamping boundary to the Si substrate was minimized with moderate *Q* at fundamental mode. Table 5.2 shows the measured *f* and *Q* factors of released SiC, Ni-Cu/SiC, G/SiC, and G/e-SiC membranes of 440 μm radius in high vacuum. For comparison, the fundamental resonance frequency (f_s) is predicted from the FEM analysis using the same membrane geometries. Table 5.3 shows the measured *f* and *Q* factors of three types of membrane (SiC, e-SiC, and G/ e-SiC), each of 1500 μm radius in high vacuum.

Table 5.2 Optically measured f and Q for the SiC membrane having radius of 440 μm, with and without the graphene in high vacuum (~10^{-7} mbar).

No.	**Sample**	**Thickness (nm)**	***f*** **(kHz)**	***F*** **simulation (kHz)**	***Q***
(a)	SiC	300	180	180-195	10763 ± 536
(b)	Ni-Cu/SiC	300	168	....	1050± 350
(c)	G/SiC	300	173	180	5062 ± 387
(d)	G / e-SiC	~170	153	152-155	27106±758

Note: Graphene thickness is ~1 nm and the Ni-Cu thickness is ~20 nm

Table 5.3 Optically measured f and Q for the SiC membrane having radius of 1500 μm, with and without the graphene in high vacuum (~10^{-7} mbar).

No.	Sample	Thickness (nm)	*f* (kHz)	*Q*
(a)	SiC	~540	45.65	1132± 99
(b)	e-SiC	~270	64.72	11148± 357
(c)	G/ e-SiC	~270	54.90	6110± 381

5.4 Discussion

5.4.1 Resonant frequency

For a clamped membrane under tensile stress σ, with a density ρ and negligible bending stiffness, its natural resonant frequencies in a vacuum are [272-275]

$$f_{n,m} = \frac{K_{n,m}}{\pi 2a}\sqrt{\frac{\sigma}{\rho}} = \frac{K_{n,m}}{\pi 2a}\sqrt{\frac{\varepsilon E}{\rho}} \tag{5.1}$$

where, the constant $K_{m,n}$ is a constant depending on the mode indices *(m, n)* and for a circular membrane, $K_{m,n}$ is the *n*-th positive root of the *m*-th order Bessel function, *E* is the Young's modulus, *ε* is the strain in the membrane.

Equation (5.1) demonstrates that resonant frequency is proportional to the square root of effective Young's modulus of graphene coated SiC membrane. Effective Young's modulus of the graphene/ SiC biomaterial is [276],

$$E_{Bim} = \frac{(E_1h_1 + E_2h_2)\frac{1}{12}\{E_1(h_1^3 + 3h_1h_2^2) + E_2(h_2^3 + 3h_1^2h_2)\} - \{h_1h_2(E_2 - E_1)/2\}^2}{\frac{1}{12}(h_1 + h_2)\{E_1(h_1^3 + 3h_1h_2^2) + E_2(h_2^3 + 3h_1^2h_2)\}} \quad (5.2)$$

where E_1 and E_2 are Young's moduli for SiC and graphene; and h_1 and h_2 are thicknesses of SiC and graphene respectively.

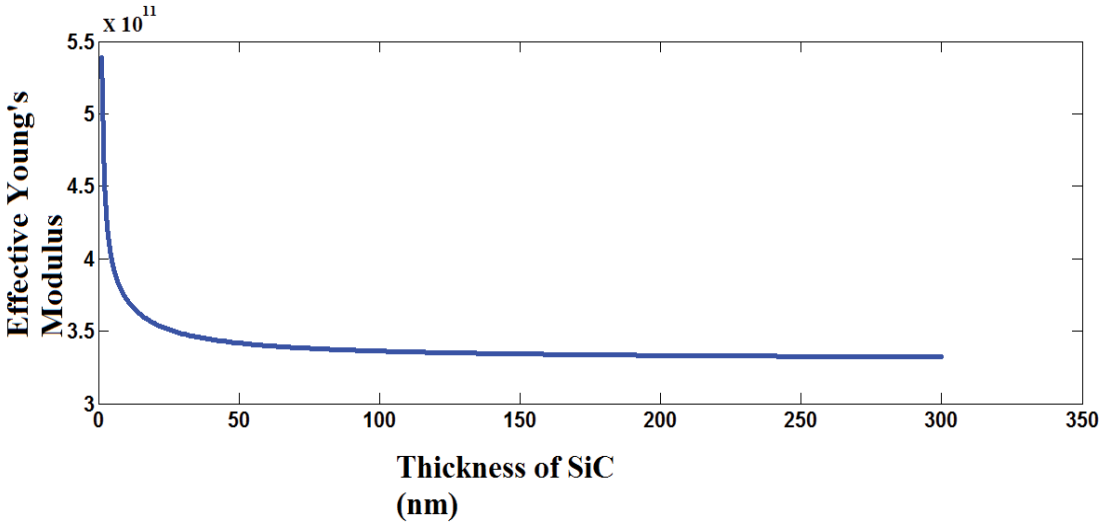

Figure 5.6 Plot of effective Young's modulus in G/SiC biomaterial membrane at different SiC thickness.

Assuming the Young's modulus of the graphene is 1 TPa [6], catalytic graphene thickness is 1 nm [1], SiC Young's modulus is 330 GPa [264] and that there is varying SiC thickness from 1 nm to 300 nm, the effective Young's modulus of G/SiC membrane could be estimated as a function of SiC thickness (figure 5.6, Appendix C). The effective Young's modulus vs SiC thickness plot demonstrates that we can tune the effective Young's modulus and hence the resonant frequency of the G/SiC membrane by varying SiC thickness. At SiC thickness below 50 nm, a significant increase in resonant frequency will occur due to the higher effective Young's modulus of the membrane. However, Young's modulus of the fabricated graphene coated SiC

membranes in this paper are primarily dominated by SiC Young's modulus because of the relatively high thickness of SiC compared to graphene.

The measured f for the SiC (100) membrane is in good agreement with the FEM simulation result (f_s) as can be seen from Table 5.2. Comparing samples (a) and (c) of Table 5.2, we can observe that the addition of the graphene layer slightly decreases the frequency of the membrane, which could be attributed to a decrease in tensile stress after graphitization. Comparing samples (a) and (b) of Table 5.3, we can observe that the reduction in the thickness of the silicon carbide layer by backside etching slightly increases the frequency of the membrane, which could also be attributed to the increase in tensile stress due to the removal of highly compressive SiC layers at and near interface [265].

5.4.2 *Q*-factor comparison

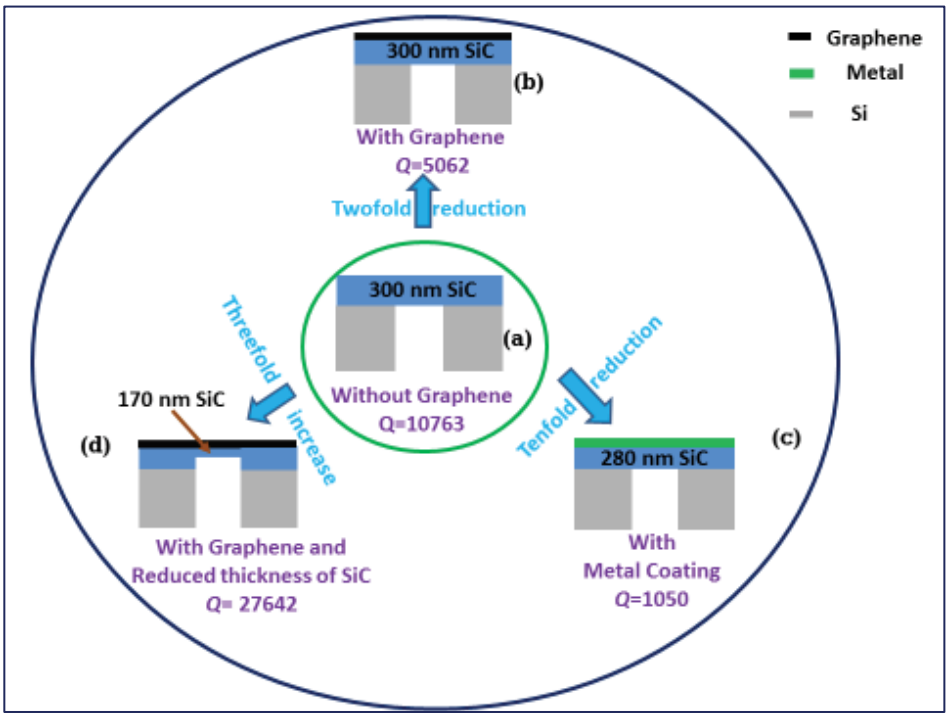

Figure 5.7 *Q*-factor analysis of fabricated SiC membranes having 440 µm radius.

We observe that the *Q*-factor of the SiC membranes is clearly affected by the graphene coatings. The *Q* is reduced by a factor of 2 (from 10763 to 5062) when the SiC membrane (figure 5.7(a)) is coated with graphene (figure 5.7(b)). On the other hand, the metal coating (figure 5.7(c)) reduces the quality factor of the membrane by almost one order of magnitude (from 10763 to 1050) when its Q is compared to that of the uncoated membrane (figure 5.7(a)). This shows that the influence of a graphene coating on the *Q* of the SiC membrane is substantially smaller as compared to the influence when using a ~20 nm thick Ni-Cu coating. The reason for this is most likely linked to the small thickness and low mass of graphene. Consequently, with the addition of the graphene coating, we can preserve the mechanical properties of SiC to a good degree as compared to using conventional metal coatings.

The 50% reduction in the *Q*-factor of graphene coated SiC membrane (G/SiC) is most likely linked to the additional surface losses due to increased roughness. The graphene coated SiC membrane (G/SiC) demonstrates at least a twofold increase in roughness [39] compared to bare SiC membrane and therefore surface loss [246, 277] is expected to be much higher in the case of a G/SiC membrane resonator compared to a SiC membrane resonator.

We have previously reported that an amorphous layer was formed during the graphitization process at the top portion of the crystalline SiC film and below the graphene layer. We have shown a TEM image of the amorphous layer in [39], where its influence on the overall crystal quality is evident. Therefore, unlike a bare SiC membrane, the G/SiC membrane has a ~20 nm amorphous and crystalline SiC layer underneath the graphene [39] and this material imperfection (grain boundaries) will lead to increased internal friction loss [156].

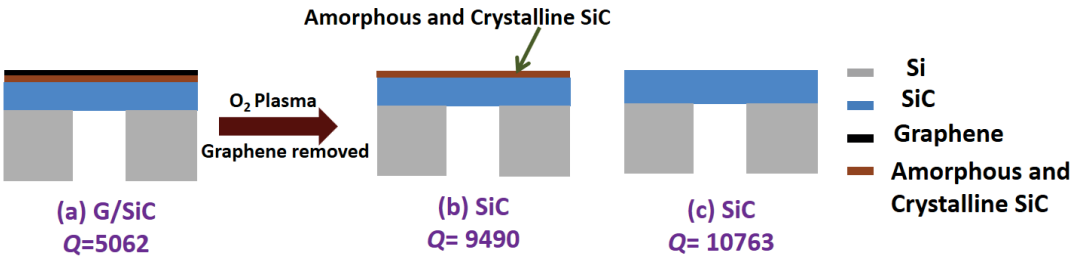

Figure 5.8 Schematic for removing graphene by oxygen plasma in order to get the SiC membrane containing amorphous and crystalline SiC layer on top.

We investigated the influence of the amorphous layer in a G/SiC membrane resonator (Q = 5062) by removing graphene (figure 5.8a). We found that the removal of catalytic graphene from a G/SiC membrane by oxygen plasma increases Q to 9490 (figure 5.8b). As a result of additional dissipation in the amorphous layer, the SiC membrane obtained after the graphene removal, demonstrates a lower Q-factor compared to a bare SiC membrane (9490 vs. 10763) (figure 5.8b vs figure 5.8c).

5.4.3 Q-factor improvement

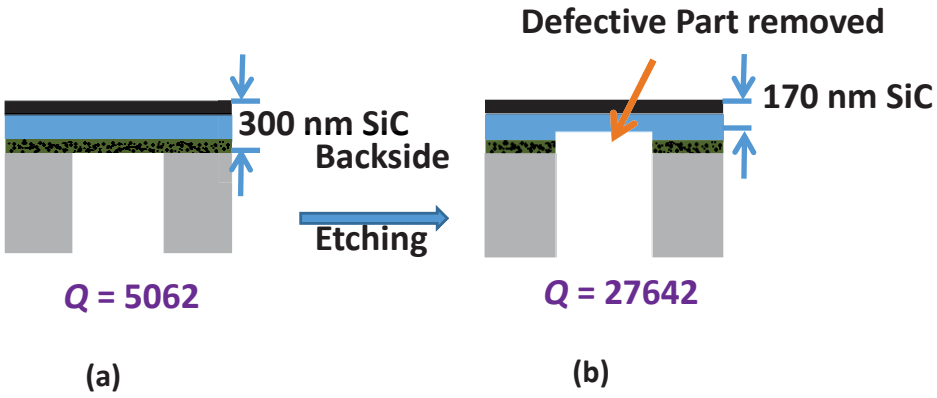

Figure 5.9 Schematic for improving Q-factor by backside etching of SiC membranes.

The Q-factor of graphene coated SiC membrane (figure 5.9(a), redrawn from figure 5.7(b)), can be further improved by removing the SiC film from its backside (figure

5.9(b), redrawn from figure 5.7 (d)) and a five-fold increase in Q (from 5062 to 27642) has been observed. We can attribute this effect to several factors.

First, an improvement in Q can be linked to the reduction in the SiC film thickness (by ~130 nm) since the membranes are strongly limited by clamping loss ($1/Q_c$) and the clamping loss is directly proportional to the membrane aspect ratio (thickness/diameter: t/D) [272, 278].

$$\frac{1}{Q_c} = A(n,m)\sigma^{3/2}\frac{t}{D} \ , \tag{5.3}$$

where, σ is the tensile stress and A is the prefactor associated with clamping loss that depends on the mode number of the resonator (n = azimuthal mode number, m = radial mode number). We estimated that the clamping loss is improved in sample (b) in figure 5.9 by a factor of 1.76 as compared to sample (a) in figure 5.9.

Secondly, although the reduction in thickness of SiC membrane causes a reduction in clamping loss by a factor of 1.76, it alone cannot explain the five-fold increase in Q (from 5062 to 27642). Therefore, the improvement in Q of 170 nm for SiC membrane (sample (b) of figure 5.9) may be correlated to the reduction of material losses by removing the interfacial portion of the SiC film from its backside. The quality of the thin hetero-epitaxial SiC on Si films is greatly influenced by the extensive number of crystal defects (stacking faults and twins) [279] nucleated close to the growing surface, due to the large lattice mismatch between the SiC film and the silicon substrate. The initial few tens of nanometers of SiC have the highest defect density and the film relaxes as thickness increases [264, 265]. This would result in high energy dissipation near the initial Si/SiC interface region, which greatly affects the value of Q.

As a third potential factor for the improvement of the Q-factor**,** after performing the backside etching of the membrane, the highly compressed nanolayer at the silicon

carbide/silicon interface is likely removed [265] so that the mean stress becomes more strongly tensile, causing an increase of the *Q* factor by damping dilution [156].

Therefore, after removing 130 nm from the backside, the *Q*-factor of 440 µm radius, 170 nm thick G/e-SiC membrane becomes as high as 27642, which is significant because resonators made solely of graphene demonstrate a poor quality factor (Q<3000) [148]. On the other hand, Barnes *et al.* [280] measured the *Q*-factor of a 500nm × 1mm × 1mm dimension SiC membrane as 26,500. The obtained *Q* factors in Table 5.2 and Table 5.3 are still much lower than the values we have previously reported for the SiC strings [44], probably due to the additional clamping losses associated with a membrane compared to those associated with a string. However, the membrane *Q* can be enhanced by selecting the appropriate mode shape, reducing the thickness of the membrane and improving the crystal quality to reduce material losses. The clamping loss can be reduced by using higher vibrational modes, since the fundamental mode is more sensitive to clamping loss [257, 272].

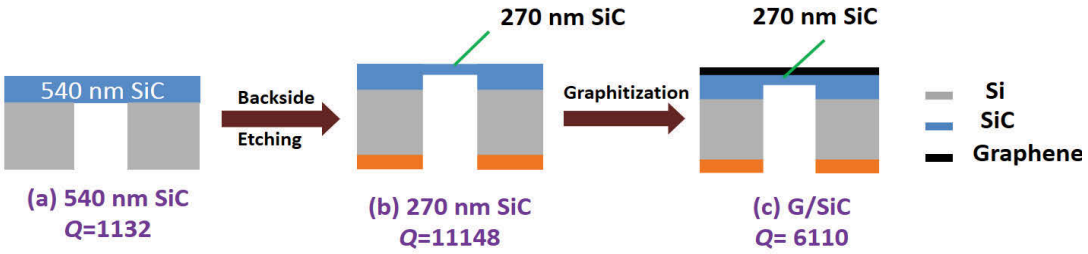

Figure 5.10 *Q*-factor analysis of fabricated SiC membranes having 1500 µm radius.

SiC membrane and graphene coated SiC membrane with 1500 µm radius demonstrate mechanical properties similar to those of 440 µm radius membrane. Comparing samples (a) and (b) of figure 5.10 (~540 nm vs ~270 nm thickness), we conclude that removal of the defective portion from the backside of the SiC film along with the ensuing simultaneous thickness reduction, resulted in a ten-fold increase in *Q* (11148

vs. 1132). The *Q*-factor of the graphene coated 1500 μm radius SiC membranes reduces by a factor of two (11148 vs. 6110) (figure 5.10), in line with the previous measurement with 440 μm membrane.

5.4.4 Advantage of catalytic graphene over transferred graphene coating

In the case of transferred graphene such as CVD graphene, relocating the graphene onto an appropriate substrate is needed for device fabrication [5]. This involves a number of additional steps and therefore poses an inconvenience. For example, in order to fabricate graphene-coated Si_3N_4 membrane resonators as fabricated by Lee *et al.* [257], the steps for transferring CVD graphene from the Cu foil to the Si_3N_4 membrane resonator need to be followed as shown in figure 5.11. First, the PMMA (polymethyl methacrylate) is spin-coated on top of the graphene/Cu stack and then the PDMS stamp is pressed over it. The resulting stack is wet-etched to remove the previous copper substrate. The stack is then gently pressed against the Si_3N_4 membrane on Si substrate, and two additional steps are needed to remove PDMS and PMMA. This cumbersome transfer process causes inconvenience in fabricating a graphene-coated Si_3N_4 drum resonator. In this regard, the catalytic graphene is advantageous over CVD and other forms of transferred graphene because it is grown on a wide bandgap SiC substrate without the need of any transfer [257].

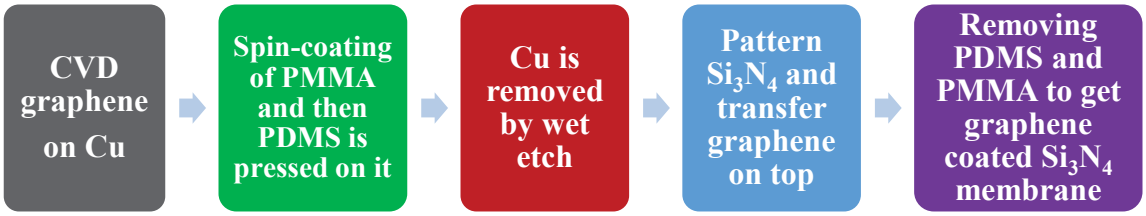

(a)

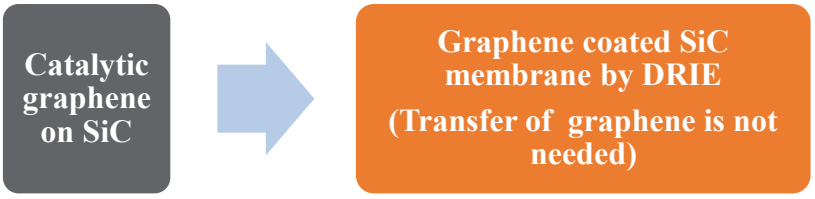

(b)

Figure 5.11 a) Schematic of steps associated with the transfer of CVD graphene on Si_3N_4 membrane [257], b) For catalytic graphene, graphene transfer is not needed [36].

For a membrane resonator coating made of transferred graphene, the adhesion of graphene with substrate is 0.151 to 1.02 J/m^2 [32, 40, 45, 118, 119, 125], which is not strong enough to guarantee sufficient mechanical reliability of transferred graphene-based devices. Our approach has adhesion as high as 5.7 J/m^2 between catalytic graphene and SiC as indicated by DCB testing; therefore sufficient adhesion is ensured in the catalytic graphene coated silicon carbide membrane resonator.

5.5. Conclusions

Silicon carbide micro-gravimetric biological/chemical sensors with high sensitivity are extremely promising as mass sensors. SiC is a preferred material because it acts as a template for graphene growth, is useful for harsh environments, high temperature applications and is biocompatible. Deposition of a conductive layer on top of the resonator is needed for enabling the electrical actuation and readout of a SiC membrane resonator. In this work, we have compared the *Q*–factor of metal over layer on SiC to

that of an alternative conductive coating, graphene. We have demonstrated that the ~20 nm thick Ni-Cu metal overlayer reduces the Q by almost one order of magnitude, whereas the SiC membrane Q decreases by only a factor of 2 when using graphene as the metal layer. The result is significant because unlike the transferred graphene coating on Si_3N_4 membrane, the as-grown catalytic graphene ensures adequate adhesion (Chapter 4) and therefore the graphene coated SiC membrane would be mechanically reliable. In order to improve the Q-factor of the graphene-coated silicon carbide membrane, a highly defective part and also the most compressively stressed portion was removed at the SiC/Si interface, and the thickness of the SiC membrane was reduced, enabling us to achieve a Q-factor of up to 2.7×10^4. The Q-factor could be further improved by reducing clamping loss through selecting appropriate membrane size and mode number. The damping in catalytic graphene coated resonators could potentially be further decreased by reducing the roughness of the SiC after graphitization.

CHAPTER 6–CONCLUSION

Until recently, no transfer-free techniques were available to grow large area monolayer graphene on silicon carbide on silicon, precluding any precise evaluation of adhesion between the grown graphene and its substrate.

In this thesis, the use of a Ni/Cu alloy-mediated process for the direct growth of monolayer graphene over large areas on cubic silicon carbide films on silicon (3C-SiC/Si) substrate has enabled us to perform double-cantilever beam (DCB) testing to assess the adhesion of graphene grown on 3C-SiC/Si wafers.

We have found the adhesion energy of the monolayer graphene to be 5.7 ± 0.7 J/m^2. This value indicates a five-fold higher adhesion for graphene, compared to that of transferred graphene onto a silicon dioxide (SiO_2) on silicon substrate, which is 1.02 J/m^2 or lower [32, 45]. The adhesion between transferred graphene and the underlying substrate originates predominantly from van der Waals forces. In the case of the graphene grown on a SiC/Si heterostructure, we suggest that the ultrahigh graphene/substrate adhesion is the result of two aspects. Firstly, the higher interface roughness, increasing the effective area for bonding and secondly, the presence of chemical bonding between the electronegative oxygen atoms of the oxidized silicon carbide and the carbon atoms of the graphene layer, formed during graphene growth [56,126]. The ultrahigh adhesion between graphene and 3C-SiC is of great relevance for ensuring reliability of future graphene-based devices and underpins the realisation of large scale, wafer-level device fabrication.

We have hence fabricated graphene/SiC membrane resonators with wafer-level processes. Typically, conventional metal layers are needed on resonators for actuation and readout purposes. However, the metal layers introduce significant damping/losses to the mechanical response of the resonators [254]. Reducing such losses by using graphene as a conductive layer has been proposed as an alternative [257], however the poor adhesion of transferred graphene to the underlying substrate is a major barrier for practical implementation. We have demonstrated that the *Q*-factor of a SiC membrane decreases by a factor of ten when a ~20nm Ni/Cu metal overlayer is deposited on SiC membrane resonators. On the other hand, when graphene overlayer is grown on SiC, the *Q*-factor of the membrane decreases by only a factor of two.

Therefore, thanks to the strong adhesion between the grown graphene and its 3C-SiC on silicon substrate, graphene-coated SiC membrane resonators are particularly promising candidates for chemical sensors. Moreover, these devices have practical significance as both SiC [259, 260] and graphene [261] have a very high degree of biocompatibility and hence could be used for biosensing.

Future suggested research lines are:

- A systematic study of the influence of different environmental parameters such as temperature and humidity on the adhesion of catalytic graphene on silicon carbide, with particular regard to the indication of potential corrosion protection granted by graphene on the defective silicon carbide material.
- The ultrahigh adhesion of the graphene demonstrated in this thesis should be utilized towards the fabrication of reliable mechanical, electrical, electromechanical, optical graphene-based devices on 3C-SiC/Si. For example, the electrical actuation and

readout of a silicon carbide membrane resonator through a graphene overlayer could be demonstrated.

APPENDIX A – MECHANISM FOR METAL ASSISTED CATALYTIC GRAPHENE SYNTHESIS

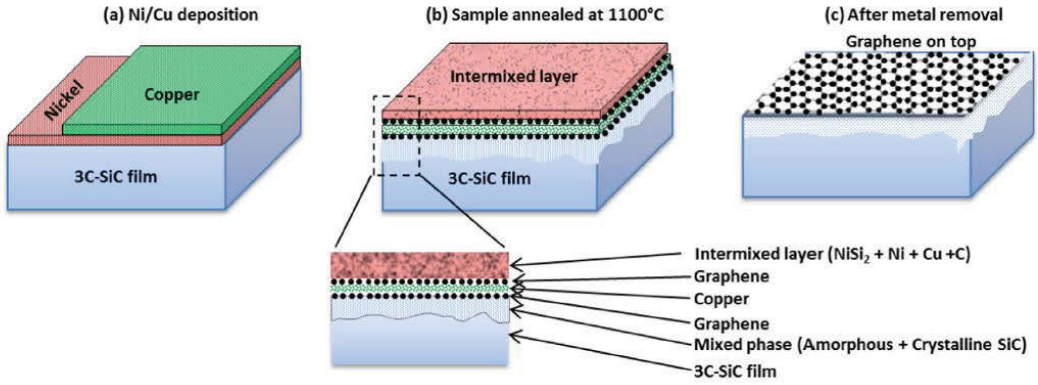

Figure A1 Schematic of the alloy-mediated catalytic graphitization mechanism. (adopted from Mishra *et al.* [39])

In alloy-mediated catalytic graphitization process [1, 39], nickel and copper is deposited atop of 3C-SiC/Si wafer, placed in the furnace and the temperature is gradually increased to 1100°C at moderate vacuum (~10^{-3}-10^{-4} mbar). After that, sample is annealed for 1 hour, leading to the formation of graphene on top of 3C-SiC film. Physical and chemical analyses suggest that the alloy-mediated graphitization comprises of three intermediate stages: (1) oxidation of Ni, (2) oxidation and amorphization of the top few tens of nm of SiC layer, accompanied by the release of atomic carbon (result of reaction between SiC and Ni), and (3) formation of the graphene layer on SiC layer by means of the catalytic action of Cu [39].

(1) <u>Oxidation of Ni</u>

As the temperature in the furnace rises to ~400 °C, Ni starts reacting with oxygen and Ni(II) oxide forms [1,39].

(2) Amorphization, oxidation of SiC and release of carbon

At temperature between 400°C–750°C, Ni and NiO diffuses into uppermost part of the crystalline 3C–SiC film, resulting in the weakening of Si–C bonding. Above ~750 °C, the Ni/NiO reacts with SiC, releasing atomic carbon. In addition, a layer consisting of amorphous and crystalline SiC is formed underneath the atomic carbon [1,39] (figure A1). The amorphous region (~20 nm) is highly oxidized containing ~20–25% oxygen, confirmed by HRTEM, ToF-SIMS depth profile and high-resolution synchrotron XPS data [39]. Furthermore, an intermixed layer ($NiSi_2$ +Ni + Cu + atomic carbon) is formed atop of atomic carbon.

(3) Graphene layer formation.

At 1100 °C, the melted Cu diffuses to the bottom of the liquid intermixed layer due to its relatively lower density, serving as a pseudo Cu foil. Being a very efficient catalyst for graphitization, Cu plays a crucial role in the fast precipitation of a monolayer graphene on the top and bottom surfaces of Cu. The presence of molten silicide and Cu enables a liquid phase epitaxy of graphene [1,39] whereas the absence of grain boundaries of melted Cu assist in achieving self-limiting graphitization [1,39]. Finally, using the Freckle etch solution, the intermixed layer along with the excess carbon on top is removed, leaving a single layer graphene on SiC layer on Si.

In summary, the synergistic combination of the catalytic actions of nickel, oxygen and copper leads to the formation of a monolayer graphene on the top surfaces of the SiC with superior uniformity and quality [1,39].

APPENDIX B - MASK FOR FABRICATING MEMBRANES

We designed a 7 inch masks by intellimask software containing two types of membranes of diameter 440 μm and 1500 μm as shown below.

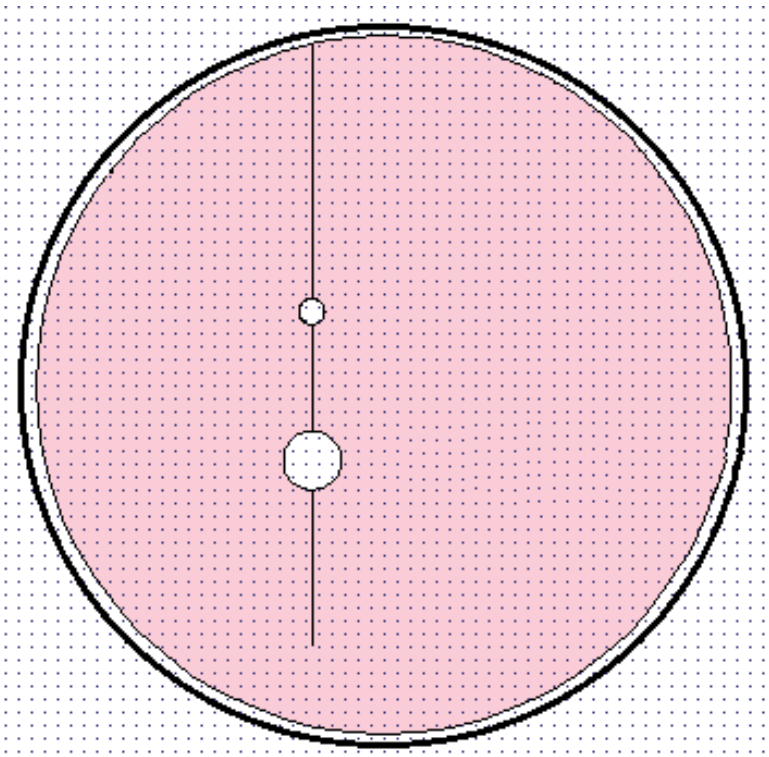

APPENDIX C: MATLAB CODE FOR ESTIMATING EFFECTIVE YOUNG'S MODULUS OF GRAPHENE/SIC BI-MATERIAL

```
%h1 = [1*10^-9,300*10^-9,10000];
h1_ary=1e-9:1e-9:300e-9;
h2=1e-9;
E2=1e12;
E1=330e9;
idx=0;
x_ax=zeros(1,length(h1_ary));
y_ax=x_ax;
for h1=1e-9:1e-9:300e-9
   idx=idx+1;
   m1=(E1*h1+E2*h2)*1/12*(E1*(h1^3+3*h1*h2^2)+E2*(h2^3+3*h1^2*h2))-
(h1*h2*(E2-E1)/2)^2; %write the function
   m2=(1/12*E1*(h1^3+3*h2^2*h1)+1/12*(h2^2+3*h1^2)*E2*h2)*(h1+h2);
   Er=m1/m2;
   %Ep=100*(Er-E1)/E1;
   x_ax(idx)=1e9*h1;
   y_ax(idx)=Er;
end

plot (x_ax,y_ax)
```

APPENDIX D: MODE MIXITY

Mode mixity, a comparative measure of the amount of shear and normal stress components, is an important parameter for interpreting the adhesion of the thin film with substrate. Mode mixity or phase angle is defined by,

$$\psi = \tan^{-1}\frac{\tau}{\sigma} = \tan^{-1}\left(\frac{K_{II}}{K_I}\right)$$

where, $\tau = K_I$ = the component of stress coplanar with material cross section (also known as the shear stress)

and $\sigma = K_{II}$= the component of stress normal with material cross section (also known as the normal stress)

The strain energy release rate is the energy dissipated during fracture per unit of newly created fracture surface area, $G = -\left[\frac{\partial U}{\partial A}\right]$, where U is the potential energy available for crack growth. Interfacial fracture toughness is a property which describes the ability of a material containing a crack to resist fracture. Interfacial fracture toughness is a function of ψ. Suppose the crack tip is loaded in mixed mode (ψ). Then the condition for initiation of crack propagation in the interface is,$G=\Gamma(\psi)$. Interfacial fracture toughness is lowest (Γ_0) when the interface undergoes pure opening fracture (at $\psi = 0^0$). On the other hand, it is the maximum when interface goes through pure shear (at $\psi = 90^0$).

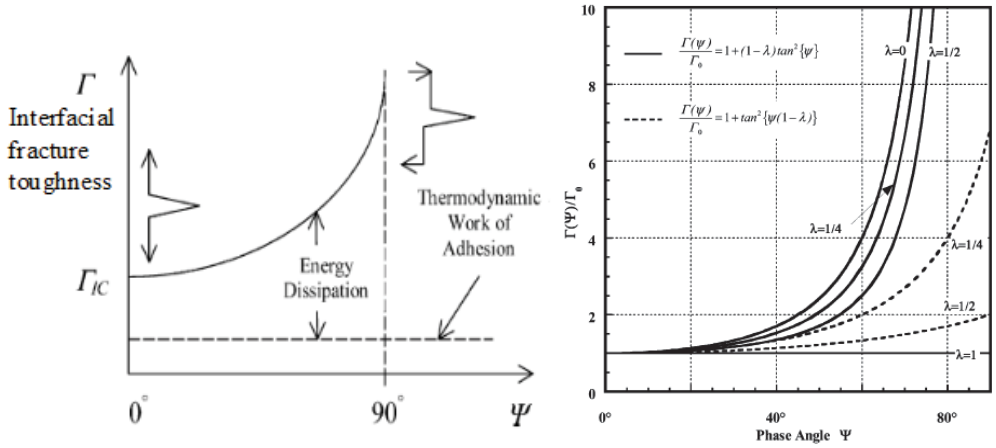

Figure D1 Interfacial fracture toughness vs phase angle (adapted from [281]).

The Interfacial fracture toughness function $\Gamma(\psi)$ could be determined experimentally and also be expressed by phenomenological theory like a realistic theory given by Hutchinson and Suo [282]

$$\Gamma(\psi) = \Gamma_0[1 + \tan^2\{\psi\{1 - \lambda\}]$$

$$\text{and } \Gamma(\psi) = \Gamma_0[1 + (1 - \lambda)\tan^2\psi]$$

where, λ is an adjustable parameter.

References

[1] F. Iacopi, N. Mishra, B. V. Cunning, D. Goding, S. Dimitrijev, R. Brock*, et al.*, "A catalytic alloy approach for graphene on epitaxial SiC on silicon wafers," *Journal of Materials Research,* vol. 30, pp. 609-616, 2015.

[2] M. Ahmed, B. Wang, B. Gupta, J. J. Boeckl, N. Motta, and F. Iacopi, "On-Silicon Supercapacitors with Enhanced Storage Performance," *Journal of The Electrochemical Society,* vol. 164, pp. A638-A644, 2017.

[3] M. F. El-Kady, V. Strong, S. Dubin, and R. B. Kaner, "Laser scribing of high-performance and flexible graphene-based electrochemical capacitors," *Science,* vol. 335, pp. 1326-1330, 2012.

[4] S. Wang, P. K. Ang, Z. Wang, A. L. L. Tang, J. T. Thong, and K. P. Loh, "High mobility, printable, and solution-processed graphene electronics," *Nano letters,* vol. 10, pp. 92-98, 2009.

[5] Z. H. Khan, A. R. Kermany, A. Öchsner, and F. Iacopi, "Mechanical and electromechanical properties of graphene and their potential application in MEMS," *Journal of Physics D: Applied Physics,* vol. 50, p. 053003, 2017.

[6] C. Lee, X. Wei, J. W. Kysar, and J. Hone, "Measurement of the elastic properties and intrinsic strength of monolayer graphene," *science,* vol. 321, pp. 385-388, 2008.

[7] L. Xu, N. Wei, X. Xu, Z. Fan, and Y. Zheng, "Defect-activated self-assembly of multilayered graphene paper: a mechanically robust architecture with high strength," *Journal of Materials Chemistry A,* vol. 1, pp. 2002-2010, 2013.

[8] H. Tomori, A. Kanda, H. Goto, Y. Ootuka, K. Tsukagoshi, S. Moriyama*, et al.*, "Introducing nonuniform strain to graphene using dielectric nanopillars," *Applied physics express,* vol. 4, p. 075102, 2011.

[9] X. Wang, H. Tian, W. Xie, Y. Shu, W.-T. Mi, M. A. Mohammad*, et al.*, "Observation of a giant two-dimensional band-piezoelectric effect on biaxial-strained graphene," *NPG Asia Materials,* vol. 7, p. e154, 2015.

[10] A. A. Balandin, S. Ghosh, W. Bao, I. Calizo, D. Teweldebrhan, F. Miao*, et al.*, "Superior thermal conductivity of single-layer graphene," *Nano letters,* vol. 8, pp. 902-907, 2008.

[11] J. H. Seol, A. L. Moore, L. Shi, I. Jo, and Z. Yao, "Thermal conductivity measurement of graphene exfoliated on silicon dioxide," *Journal of Heat Transfer,* vol. 133, p. 022403, 2011.

[12] K. S. Kim, Y. Zhao, H. Jang, S. Y. Lee, J. M. Kim, K. S. Kim*, et al.*, "Large-scale pattern growth of graphene films for stretchable transparent electrodes," *nature,* vol. 457, p. 706, 2009.

[13] S. Chen, L. Brown, M. Levendorf, W. Cai, S.-Y. Ju, J. Edgeworth*, et al.*, "Oxidation resistance of graphene-coated Cu and Cu/Ni alloy," *ACS nano,* vol. 5, pp. 1321-1327, 2011.

[14] F. Iacopi, S. Brongersma, B. Vandevelde, M. O'Toole, D. Degryse, Y. Travaly*, et al.*, "Challenges for structural stability of ultra-low-k-based interconnects," *Microelectronic engineering,* vol. 75, pp. 54-62, 2004.

[15] H. C. Schniepp, K. N. Kudin, J.-L. Li, R. K. Prud'homme, R. Car, D. A. Saville*, et al.*, "Bending properties of single functionalized graphene sheets probed by atomic force microscopy," *ACS nano,* vol. 2, pp. 2577-2584, 2008.

[16] V. Carozo, C. M. Almeida, E. H. Ferreira, L. G. Cancado, C. A. Achete, and A. Jorio, "Raman signature of graphene superlattices," *Nano letters,* vol. 11, pp. 4527-4534, 2011.

[17] K.-S. Kim, H.-J. Lee, C. Lee, S.-K. Lee, H. Jang, J.-H. Ahn*, et al.*, "Chemical vapor deposition-grown graphene: the thinnest solid lubricant," *ACS nano,* vol. 5, pp. 5107-5114, 2011.

[18] K. Celebi, J. Buchheim, R. M. Wyss, A. Droudian, P. Gasser, I. Shorubalko*, et al.*, "Ultimate permeation across atomically thin porous graphene," *Science,* vol. 344, pp. 289-292, 2014.

[19] J. S. Bunch and M. L. Dunn, "Adhesion mechanics of graphene membranes," *Solid State Communications,* vol. 152, pp. 1359-1364, 2012.

[20] M. Ahmed, N. Kishi, R. Sugita, A. Fukaya, I. Khatri, J. Liang*, et al.*, "Graphene synthesis by thermal chemical vapor deposition using solid precursor," *Journal of Materials Science: Materials in Electronics,* vol. 24, pp. 2151-2155, 2013.

[21] M. Ahmed, N. Kishi, and T. Soga, "Large scale bi-layer graphene by suppression of nucleation from a solid precursor," *RSC Advances,* vol. 5, pp. 42645-42652, 2015.

[22] M. Ahmed, M. J. Uddin, M. A. Rahman, N. Kishi, and T. Soga, "Controlled Cu Nanoparticle Growth on Wrinkle Affecting Deposition of Large Scale Graphene," *Journal of Crystal Growth,* 2016.

[23] H. Jang, Y. J. Park, X. Chen, T. Das, M. S. Kim, and J. H. Ahn, "Graphene-Based Flexible and Stretchable Electronics," *Advanced Materials,* 2016.

[24] A. Giesbers, P. Bouten, J. Cillessen, L. van der Tempel, J. Klootwijk, A. Pesquera*, et al.*, "Defects, a challenge for graphene in flexible electronics," *Solid State Communications,* 2016.

[25] E. O. Polat, O. Balci, N. Kakenov, C. Kocabas, and R. Dahiya, "Synthesis of graphene on ultra-smooth copper foils for large area flexible electronics," in *Ph. D. Research in Microelectronics and Electronics (PRIME), 2015 11th Conference on*, 2015, pp. 53-56.

[26] Y. Shao, M. F. El-Kady, L. J. Wang, Q. Zhang, Y. Li, H. Wang*, et al.*, "Graphene-based materials for flexible supercapacitors," *Chemical Society Reviews,* vol. 44, pp. 3639-3665, 2015.

[27] N. Petrone, I. Meric, T. Chari, K. L. Shepard, and J. Hone, "Graphene field-effect transistors for radio-frequency flexible electronics," *Electron Devices Society, IEEE Journal of the,* vol. 3, pp. 44-48, 2015.

[28] M. Merisalu, T. Kahro, J. Kozlova, A. Niilisk, A. Nikolajev, M. Marandi*, et al.*, "Graphene–polypyrrole thin hybrid corrosion resistant coatings for copper," *Synthetic Metals,* vol. 200, pp. 16-23, 2015.

[29] D. Prasai, J. C. Tuberquia, R. R. Harl, G. K. Jennings, and K. I. Bolotin, "Graphene: corrosion-inhibiting coating," *ACS nano,* vol. 6, pp. 1102-1108, 2012.

[30] E. Sutter, P. Albrecht, F. E. Camino, and P. Sutter, "Monolayer graphene as ultimate chemical passivation layer for arbitrarily shaped metal surfaces," *Carbon,* vol. 48, pp. 4414-4420, 2010.

[31] N. Kirkland, T. Schiller, N. Medhekar, and N. Birbilis, "Exploring graphene as a corrosion protection barrier," *Corrosion Science,* vol. 56, pp. 1-4, 2012.

[32] W. Cheol Shin, T. Yoon, J. Hun Mun, T. Yong Kim, S.-Y. Choi, T.-S. Kim*, et al.*, "Doping suppression and mobility enhancement of graphene transistors fabricated using an adhesion promoting dry transfer process," *Applied Physics Letters,* vol. 103, p. 243504, 2013.

[33] K. V. Emtsev, A. Bostwick, K. Horn, J. Jobst, G. L. Kellogg, L. Ley, *et al.*, "Towards wafer-size graphene layers by atmospheric pressure graphitization of silicon carbide," *Nature materials,* vol. 8, pp. 203-207, 2009.

[34] W. A. De Heer, C. Berger, X. Wu, P. N. First, E. H. Conrad, X. Li, *et al.*, "Epitaxial graphene," *Solid State Communications,* vol. 143, pp. 92-100, 2007.

[35] B. Gupta, M. Notarianni, N. Mishra, M. Shafiei, F. Iacopi, and N. Motta, "Evolution of epitaxial graphene layers on 3C SiC/Si (111) as a function of annealing temperature in UHV," *Carbon,* vol. 68, pp. 563-572, 2014.

[36] B. V. Cunning, M. Ahmed, N. Mishra, A. R. Kermany, B. Wood, and F. Iacopi, "Graphitized silicon carbide microbeams: wafer-level, self-aligned graphene on silicon wafers," *Nanotechnology,* vol. 25, p. 325301, 2014.

[37] F. Iacopi, M. Ahmed, and B. V. Cunning, "Process for forming graphene layers on silicon carbide," ed: US Patent App. 15/022,532, 2014.

[38] F. Iacopi, N. Mishra, B. Cunning, A. Kermany, D. Goding, A. Pradeepkumar, *et al.*, "Self-aligned graphene on silicon substrates as ultimate metal replacement for nanodevices."

[39] N. Mishra, J. J. Boeckl, A. Tadich, R. T. Jones, P. J. Pigram, M. Edmonds, *et al.*, "Solid source growth of graphene with Ni–Cu catalysts: towards high quality in situ graphene on silicon," *Journal of Physics D: Applied Physics,* vol. 50, p. 095302, 2017.

[40] T. Yoon, W. C. Shin, T. Y. Kim, J. H. Mun, T.-S. Kim, and B. J. Cho, "Direct measurement of adhesion energy of monolayer graphene as-grown on copper and its application to renewable transfer process," *Nano letters,* vol. 12, pp. 1448-1452, 2012.

[41] J. Seo, W. S. Chang, and T.-S. Kim, "Adhesion improvement of graphene/copper interface using UV/ozone treatments," *Thin solid films,* vol. 584, pp. 170-175, 2015.

[42] S. R. Na, J. W. Suk, L. Tao, D. Akinwande, R. S. Ruoff, R. Huang, *et al.*, "Selective mechanical transfer of graphene from seed copper foil using rate effects," *ACS nano,* vol. 9, pp. 1325-1335, 2015.

[43] R. Brock, R. Rewari, F. D. Novoa, P. Hebert, J. Ermer, D. C. Miller, *et al.*, "Quantitative adhesion characterization of antireflective coatings in

multijunction photovoltaics," *Solar Energy Materials and Solar Cells,* vol. 153, pp. 78-83, 2016.

[44] A. R. Kermany, J. S. Bennett, G. A. Brawley, W. P. Bowen, and F. Iacopi, "Factors affecting the f ☒Q product of 3C-SiC microstrings: what is the upper limit for sensitivity?," *Journal of Applied Physics,* p. (to be published), 2016

[45] S. P. Koenig, N. G. Boddeti, M. L. Dunn, and J. S. Bunch, "Ultrastrong adhesion of graphene membranes," *Nature nanotechnology,* vol. 6, pp. 543-546, 2011.

[46] K. S. Novoselov, A. K. Geim, S. Morozov, D. Jiang, Y. Zhang, S. a. Dubonos, *et al.*, "Electric field effect in atomically thin carbon films," *science,* vol. 306, pp. 666-669, 2004.

[47] (date accessed 17 June 2016). *The Royal Schwedish Academy of Science. Scientific Background on the Nobel Prize in Physics 2010*. Available: www.nobelprize.org/nobel_prizes/.../advanced-physicsprize2010.pdf

[48] M. S. Fuhrer, C. N. Lau, and A. H. MacDonald, "Graphene: materially better carbon," *MRS bulletin,* vol. 35, pp. 289-295, 2010.

[49] Y. Li, "Reversible wrinkles of monolayer graphene on a polymer substrate: toward stretchable and flexible electronics," *Soft matter,* vol. 12, pp. 3202-3213, 2016.

[50] S. Bae, H. Kim, Y. Lee, X. Xu, J.-S. Park, Y. Zheng, *et al.*, "Roll-to-roll production of 30-inch graphene films for transparent electrodes," *Nature nanotechnology,* vol. 5, pp. 574-578, 2010.

[51] U. Khan, P. May, A. O'Neill, and J. N. Coleman, "Development of stiff, strong, yet tough composites by the addition of solvent exfoliated graphene to polyurethane," *Carbon,* vol. 48, pp. 4035-4041, 2010.

[52] R. Jan, A. Habib, and I. H. Gul, "Stiff, strong, yet tough free-standing dielectric films of graphene nanosheets-polyurethane nanocomposites with very high dielectric constant and loss," *Electronic Materials Letters,* vol. 12, pp. 91-99, 2016.

[53] H. Lee, M. Kim, I. Kim, and H. Lee, "Flexible and Stretchable Optoelectronic Devices using Silver Nanowires and Graphene," *Advanced Materials,* 2016.

[54] M. Ahmed, M. Khawaja, M. Notarianni, B. Wang, D. Goding, B. Gupta*, et al.*, "A thin film approach for SiC-derived graphene as an on-chip electrode for supercapacitors," *Nanotechnology,* vol. 26, p. 434005, 2015.

[55] B. Wang, M. Ahmed, B. Wood, and F. Iacopi, "All-solid-state supercapacitors on silicon using graphene from silicon carbide," *Applied Physics Letters,* vol. 108, p. 183903, 2016.

[56] G. da Cunha Rodrigues, P. Zelenovskiy, K. Romanyuk, S. Luchkin, Y. Kopelevich, and A. Kholkin, "Strong piezoelectricity in single-layer graphene deposited on SiO2 grating substrates," *Nature communications,* vol. 6, 2015.

[57] A. D. Smith, S. Vaziri, F. Niklaus, A. C. Fischer, M. Sterner, A. Delin*, et al.*, "Pressure sensors based on suspended graphene membranes," *Solid-State Electronics,* vol. 88, pp. 89-94, 2013.

[58] J. Zhao, C. He, R. Yang, Z. Shi, M. Cheng, W. Yang*, et al.*, "Ultra-sensitive strain sensors based on piezoresistive nanographene films," *Applied Physics Letters,* vol. 101, p. 063112, 2012.

[59] A. Smith, F. Niklaus, A. Paussa, S. Vaziri, A. C. Fischer, M. Sterner*, et al.*, "Electromechanical piezoresistive sensing in suspended graphene membranes," *Nano letters,* vol. 13, pp. 3237-3242, 2013.

[60] J. S. Bunch, A. M. Van Der Zande, S. S. Verbridge, I. W. Frank, D. M. Tanenbaum, J. M. Parpia*, et al.*, "Electromechanical resonators from graphene sheets," *Science,* vol. 315, pp. 490-493, 2007.

[61] A. Eichler, J. Moser, J. Chaste, M. Zdrojek, I. Wilson-Rae, and A. Bachtold, "Nonlinear damping in mechanical resonators made from carbon nanotubes and graphene," *Nature nanotechnology,* vol. 6, pp. 339-342, 2011.

[62] S. Ghosh, I. Calizo, D. Teweldebrhan, E. Pokatilov, D. Nika, A. Balandin*, et al.*, "Extremely high thermal conductivity of graphene: Prospects for thermal management applications in nanoelectronic circuits," *Applied Physics Letters,* vol. 92, p. 151911, 2008.

[63] D. Yoon, Y.-W. Son, and H. Cheong, "Negative thermal expansion coefficient of graphene measured by Raman spectroscopy," *Nano letters,* vol. 11, pp. 3227-3231, 2011.

[64] X. Li, W. Cai, J. An, S. Kim, J. Nah, D. Yang*, et al.*, "Large-area synthesis of high-quality and uniform graphene films on copper foils," *Science,* vol. 324, pp. 1312-1314, 2009.

[65] A. Obraztsov, E. Obraztsova, A. Tyurnina, and A. Zolotukhin, "Chemical vapor deposition of thin graphite films of nanometer thickness," *Carbon,* vol. 45, pp. 2017-2021, 2007.

[66] K. Novoselov, A. K. Geim, S. Morozov, D. Jiang, M. Katsnelson, I. Grigorieva*, et al.*, "Two-dimensional gas of massless Dirac fermions in graphene," *nature,* vol. 438, pp. 197-200, 2005.

[67] A. Capasso, A. D. R. Castillo, H. Sun, A. Ansaldo, V. Pellegrini, and F. Bonaccorso, "Ink-jet printing of graphene for flexible electronics: An environmentally-friendly approach," *Solid State Communications,* vol. 224, pp. 53-63, 2015.

[68] J. Li, F. Ye, S. Vaziri, M. Muhammed, M. C. Lemme, and M. Östling, "Efficient inkjet printing of graphene," *Advanced materials,* vol. 25, pp. 3985-3992, 2013.

[69] E. B. Secor, P. L. Prabhumirashi, K. Puntambekar, M. L. Geier, and M. C. Hersam, "Inkjet printing of high conductivity, flexible graphene patterns," *The journal of physical chemistry letters,* vol. 4, pp. 1347-1351, 2013.

[70] D. J. Finn, M. Lotya, G. Cunningham, R. J. Smith, D. McCloskey, J. F. Donegan*, et al.*, "Inkjet deposition of liquid-exfoliated graphene and MoS 2 nanosheets for printed device applications," *Journal of Materials Chemistry C,* vol. 2, pp. 925-932, 2014.

[71] W. Qian, R. Hao, J. Zhou, M. Eastman, B. A. Manhat, Q. Sun*, et al.*, "Exfoliated graphene-supported Pt and Pt-based alloys as electrocatalysts for direct methanol fuel cells," *Carbon,* vol. 52, pp. 595-604, 2013.

[72] H. Sun, A. E. D. R. Castillo, S. Monaco, A. Capasso, A. Ansaldo, M. Prato*, et al.*, "Binder-free graphene as an advanced anode for lithium batteries," *Journal of Materials Chemistry A,* 2016.

[73] C. Sun, F. Li, C. Ma, Y. Wang, Y. Ren, W. Yang*, et al.*, "Graphene–Co 3 O 4 nanocomposite as an efficient bifunctional catalyst for lithium–air batteries," *Journal of Materials Chemistry A,* vol. 2, pp. 7188-7196, 2014.

[74] A. L. M. Reddy, A. Srivastava, S. R. Gowda, H. Gullapalli, M. Dubey, and P. M. Ajayan, "Synthesis of nitrogen-doped graphene films for lithium battery application," *ACS nano,* vol. 4, pp. 6337-6342, 2010.

[75] X. Wei, B. Fragneaud, C. A. Marianetti, and J. W. Kysar, "Nonlinear elastic behavior of graphene: Ab initio calculations to continuum description," *Physical Review B,* vol. 80, p. 205407, 2009.

[76] F. Liu, P. Ming, and J. Li, "Ab initio calculation of ideal strength and phonon instability of graphene under tension," *Physical Review B,* vol. 76, p. 064120, 2007.

[77] J.-U. Lee, D. Yoon, and H. Cheong, "Estimation of Young's modulus of graphene by Raman spectroscopy," *Nano letters,* vol. 12, pp. 4444-4448, 2012.

[78] I. Ovid'ko, "Mechanical properties of graphene," *Rev. Adv. Mater. Sci,* vol. 34, pp. 1-11, 2013.

[79] C. Lee, X. Wei, Q. Li, R. Carpick, J. W. Kysar, and J. Hone, "Elastic and frictional properties of graphene," *physica status solidi (b),* vol. 246, pp. 2562-2567, 2009.

[80] C. S. Ruiz-Vargas, H. L. Zhuang, P. Y. Huang, A. M. van der Zande, S. Garg, P. L. McEuen*, et al.*, "Softened elastic response and unzipping in chemical vapor deposition graphene membranes," *Nano letters,* vol. 11, pp. 2259-2263, 2011.

[81] M. Huang, T. A. Pascal, H. Kim, W. A. Goddard III, and J. R. Greer, "Electronic− mechanical coupling in graphene from in situ nanoindentation experiments and multiscale atomistic simulations," *Nano letters,* vol. 11, pp. 1241-1246, 2011.

[82] Y. Liu, D. Zhang, K. Wang, Y. Liu, and Y. Shang, "A novel strain sensor based on graphene composite films with layered structure," *Composites Part A: Applied Science and Manufacturing,* vol. 80, pp. 95-103, 2016.

[83] Y. Y. Zhang and Y. Gu, "Mechanical properties of graphene: Effects of layer number, temperature and isotope," *Computational Materials Science,* vol. 71, pp. 197-200, 2013.

[84] S. Subrina, D. Kotchetkov, and A. A. Balandin, "Heat removal in silicon-on-insulator integrated circuits with graphene lateral heat spreaders," *Electron Device Letters, IEEE,* vol. 30, pp. 1281-1283, 2009.

[85] E. Pop, D. Mann, Q. Wang, K. Goodson, and H. Dai, "Thermal conductance of an individual single-wall carbon nanotube above room temperature," *Nano letters,* vol. 6, pp. 96-100, 2006.

[86] P. Kim, L. Shi, A. Majumdar, and P. McEuen, "Thermal transport measurements of individual multiwalled nanotubes," *Physical review letters,* vol. 87, p. 215502, 2001.

[87] P. Klemens and D. Pedraza, "Thermal conductivity of graphite in the basal plane," *Carbon,* vol. 32, pp. 735-741, 1994.

[88] J. H. Seol, I. Jo, A. L. Moore, L. Lindsay, Z. H. Aitken, M. T. Pettes*, et al.*, "Two-dimensional phonon transport in supported graphene," *Science,* vol. 328, pp. 213-216, 2010.

[89] S. Chen, Q. Wu, C. Mishra, J. Kang, H. Zhang, K. Cho*, et al.*, "Thermal conductivity of isotopically modified graphene," *Nature materials,* vol. 11, pp. 203-207, 2012.

[90] J. Los, K. Zakharchenko, M. Katsnelson, and A. Fasolino, "Melting temperature of graphene," *Physical Review B,* vol. 91, p. 045415, 2015.

[91] K. Zakharchenko, A. Fasolino, J. Los, and M. Katsnelson, "Melting of graphene: from two to one dimension," *Journal of Physics: Condensed Matter,* vol. 23, p. 202202, 2011.

[92] W. Gao and R. Huang, "Thermomechanics of monolayer graphene: Rippling, thermal expansion and elasticity," *Journal of the Mechanics and Physics of Solids,* vol. 66, pp. 42-58, 2014.

[93] N. Mounet and N. Marzari, "First-principles determination of the structural, vibrational and thermodynamic properties of diamond, graphite, and derivatives," *Physical Review B,* vol. 71, p. 205214, 2005.

[94] V. Singh, S. Sengupta, H. S. Solanki, R. Dhall, A. Allain, S. Dhara*, et al.*, "Probing thermal expansion of graphene and modal dispersion at low-temperature using graphene nanoelectromechanical systems resonators," *Nanotechnology,* vol. 21, p. 165204, 2010.

[95] J.-W. Jiang, J.-S. Wang, and B. Li, "Thermal expansion in single-walled carbon nanotubes and graphene: Nonequilibrium Green's function approach," *Physical Review B,* vol. 80, p. 205429, 2009.

[96] W. Bao, F. Miao, Z. Chen, H. Zhang, W. Jang, C. Dames*, et al.*, "Controlled ripple texturing of suspended graphene and ultrathin graphite membranes," *Nature nanotechnology,* vol. 4, pp. 562-566, 2009.

[97] E. Steward, B. Cook, and E. Kellett, "Dependence on temperature of the interlayer spacing in carbons of different graphitic perfection," 1960.

[98] D. Kirilenko, A. Dideykin, and G. Van Tendeloo, "Measuring the corrugation amplitude of suspended and supported graphene," *Physical Review B,* vol. 84, p. 235417, 2011.

[99] Q. Li, C. Lee, R. W. Carpick, and J. Hone, "Substrate effect on thickness-dependent friction on graphene," *physica status solidi (b),* vol. 247, pp. 2909-2914, 2010.

[100] J.-H. Ko, S. Kwon, I.-S. Byun, J. S. Choi, B. H. Park, Y.-H. Kim*, et al.*, "Nanotribological properties of fluorinated, hydrogenated, and oxidized graphenes," *Tribology Letters,* vol. 50, pp. 137-144, 2013.

[101] S. Kwon, J.-H. Ko, K.-J. Jeon, Y.-H. Kim, and J. Y. Park, "Enhanced nanoscale friction on fluorinated graphene," *Nano letters,* vol. 12, pp. 6043-6048, 2012.

[102] H. Lee, N. Lee, Y. Seo, J. Eom, and S. Lee, "Comparison of frictional forces on graphene and graphite," *Nanotechnology,* vol. 20, p. 325701, 2009.

[103] J. S. Choi, J.-S. Kim, I.-S. Byun, D. H. Lee, M. J. Lee, B. H. Park*, et al.*, "Friction anisotropy–driven domain imaging on exfoliated monolayer graphene," *Science,* vol. 333, pp. 607-610, 2011.

[104] I. Szlufarska, M. Chandross, and R. W. Carpick, "Recent advances in single-asperity nanotribology," *Journal of Physics D: Applied Physics,* vol. 41, p. 123001, 2008.

[105] O. Penkov, H.-J. Kim, H.-J. Kim, and D.-E. Kim, "Tribology of graphene: a review," *International journal of precision engineering and manufacturing,* vol. 15, pp. 577-585, 2014.

[106] R. W. Carpick, D. Ogletree, and M. Salmeron, "Lateral stiffness: a new nanomechanical measurement for the determination of shear strengths with friction force microscopy," *Applied Physics Letters,* vol. 70, pp. 1548-1550, 1997.

[107] R. W. Carpick and M. Salmeron, "Scratching the surface: fundamental investigations of tribology with atomic force microscopy," *Chemical Reviews,* vol. 97, pp. 1163-1194, 1997.

[108] C. Lee, Q. Li, W. Kalb, X.-Z. Liu, H. Berger, R. W. Carpick*, et al.*, "Frictional characteristics of atomically thin sheets," *Science,* vol. 328, pp. 76-80, 2010.

[109] F. Wählisch, J. Hoth, C. Held, T. Seyller, and R. Bennewitz, "Friction and atomic-layer-scale wear of graphitic lubricants on SiC (0001) in dry sliding," *Wear,* vol. 300, pp. 78-81, 2013.

[110] T. Filleter, J. L. McChesney, A. Bostwick, E. Rotenberg, K. Emtsev, T. Seyller*, et al.*, "Friction and dissipation in epitaxial graphene films," *Physical review letters,* vol. 102, p. 086102, 2009.

[111] D.-H. Cho, L. Wang, J.-S. Kim, G.-H. Lee, E. S. Kim, S. Lee*, et al.*, "Effect of surface morphology on friction of graphene on various substrates," *Nanoscale,* vol. 5, pp. 3063-3069, 2013.

[112] T. Filleter and R. Bennewitz, "Structural and frictional properties of graphene films on SiC (0001) studied by atomic force microscopy," *Physical Review B,* vol. 81, p. 155412, 2010.

[113] M. Rastei, B. Heinrich, and J. Gallani, "Puckering Stick-Slip Friction Induced by a Sliding Nanoscale Contact," *Physical review letters,* vol. 111, p. 084301, 2013.

[114] L.-Y. Lin, D.-E. Kim, W.-K. Kim, and S.-C. Jun, "Friction and wear characteristics of multi-layer graphene films investigated by atomic force microscopy," *Surface and Coatings Technology,* vol. 205, pp. 4864-4869, 2011.

[115] (date accessed 5 June 2017). *Mechanical Reliability of Microelectronic Interfaces*. Available: http://dauskardt.stanford.edu/robert_hohlfelder/Techniques.html

[116] C. Boztug, J. R. Sánchez-Pérez, F. Cavallo, M. G. Lagally, and R. Paiella, "Strained-germanium nanostructures for infrared photonics," *ACS nano,* vol. 8, pp. 3136-3151, 2014.

[117] N. G. Boddeti, S. P. Koenig, R. Long, J. Xiao, J. S. Bunch, and M. L. Dunn, "Mechanics of adhered, pressurized graphene blisters," *Journal of Applied Mechanics,* vol. 80, p. 040909, 2013.

[118] Z. Cao, P. Wang, W. Gao, L. Tao, J. Suk, R. Ruoff*, et al.*, "A blister test for interfacial adhesion of large-scale transferred graphene," *Carbon,* vol. 69, pp. 390-400, 2014.

[119] Z. Zong, C.-L. Chen, M. R. Dokmeci, and K.-t. Wan, "Direct measurement of graphene adhesion on silicon surface by intercalation of nanoparticles," *Journal of Applied Physics,* vol. 107, p. 026104, 2010.

[120] S. Das, D. Lahiri, D.-Y. Lee, A. Agarwal, and W. Choi, "Measurements of the adhesion energy of graphene to metallic substrates," *Carbon,* vol. 59, pp. 121-129, 2013.

[121] G. Wells, T. Hopf, K. Vassilevski, E. Escobedo-Cousin, N. Wright, A. Horsfall*, et al.*, "Determination of the adhesion energy of graphene on SiC (0001) via measurement of pleat defects," *Applied Physics Letters,* vol. 105, p. 193109, 2014.

[122] N. Ferralis, R. Maboudian, and C. Carraro, "Evidence of structural strain in epitaxial graphene layers on 6H-SiC (0001)," *Physical review letters,* vol. 101, p. 156801, 2008.

[123] C. Riedl, C. Coletti, T. Iwasaki, A. Zakharov, and U. Starke, "Quasi-free-standing epitaxial graphene on SiC obtained by hydrogen intercalation," *Physical review letters,* vol. 103, p. 246804, 2009.

[124] Z. H. Ni, T. Yu, Y. H. Lu, Y. Y. Wang, Y. P. Feng, and Z. X. Shen, "Uniaxial strain on graphene: Raman spectroscopy study and band-gap opening," *ACS nano,* vol. 2, pp. 2301-2305, 2008.

[125] S. R. Na, S. Rahimi, L. Tao, H. Chou, S. K. Ameri, D. Akinwande*, et al.*, "Clean graphene interfaces by selective dry transfer for large area silicon integration," *Nanoscale,* vol. 8, pp. 7523-7533, 2016.

[126] S. Das, D. Lahiri, A. Agarwal, and W. Choi, "Interfacial bonding characteristics between graphene and dielectric substrates," *Nanotechnology,* vol. 25, p. 045707, 2014.

[127] (date accessed 5 June 2017). S. D. C. Bruner, R. Brock (PV active layers), F. Novoa, W. Cui, S. Isaacson, T. Mirfakhrai, R. H. Dauskardt. *Adhesion and Debonding Kinetics in PV Devices and Modules*. Available: www.nrel.gov/pv/pdfs/2014_pvmrw_30_dauskardt.pdf

[128] E. KHATIBI, "Piezoresistivity of graphene," 2011.

[129] Y. Kanda, "Piezoresistance effect of silicon," *Sensors and Actuators A: Physical,* vol. 28, pp. 83-91, 1991.

[130] W. Yang, C. He, L. Zhang, Y. Wang, Z. Shi, M. Cheng*, et al.*, "Growth, characterization, and properties of nanographene," *Small,* vol. 8, pp. 1429-1435, 2012.

[131] H. Hosseinzadegan, C. Todd, A. Lal, M. Pandey, M. Levendorf, and J. Park, "Graphene has ultra high piezoresistive gauge factor," in *Micro Electro*

Mechanical Systems (MEMS), 2012 IEEE 25th International Conference on, 2012, pp. 611-614.

[132] Y. Lee, S. Bae, H. Jang, S. Jang, S.-E. Zhu, S. H. Sim*, et al.*, "Wafer-scale synthesis and transfer of graphene films," *Nano letters,* vol. 10, pp. 490-493, 2010.

[133] Y. Wang, R. Yang, Z. Shi, L. Zhang, D. Shi, E. Wang*, et al.*, "Super-elastic graphene ripples for flexible strain sensors," *ACS nano,* vol. 5, pp. 3645-3650, 2011.

[134] Y.-J. Kim, J. Y. Cha, H. Ham, H. Huh, D.-S. So, and I. Kang, "Preparation of piezoresistive nano smart hybrid material based on graphene," *Current Applied Physics,* vol. 11, pp. S350-S352, 2011.

[135] S.-E. Zhu, M. K. Ghatkesar, C. Zhang, and G. Janssen, "Graphene based piezoresistive pressure sensor," *Applied Physics Letters,* vol. 102, p. 161904, 2013.

[136] L. Christel and K. Petersen, "A catheter pressure sensor with side vent using multiple silicon fusion bonding," in *7th International Conference on Solid− State Sensors and Actuators (Transducers' 93), Yokohama, Japan*, 1993, pp. 7-10.

[137] P. Melvås, "Ultraminiaturized Pressure Sensor for Catheter Based Applications," 2002.

[138] C. K. Fung, M. Q. Zhang, R. H. Chan, and W. J. Li, "A PMMA-based micro pressure sensor chip using carbon nanotubes as sensing elements," in *Micro Electro Mechanical Systems, 2005. MEMS 2005. 18th IEEE International Conference on*, 2005, pp. 251-254.

[139] J. S. Bunch, S. S. Verbridge, J. S. Alden, A. M. van der Zande, J. M. Parpia, H. G. Craighead*, et al.*, "Impermeable atomic membranes from graphene sheets," *Nano letters,* vol. 8, pp. 2458-2462, 2008.

[140] Y. Zhang, "In situ fatigue crack detection using piezoelectric paint sensor," *Journal of Intelligent Material Systems and Structures,* vol. 17, pp. 843-852, 2006.

[141] P. Kijanka, P. Packo, W. J. Staszewski, and F. L. di Scalea, "Actuation stress modelling of piezoceramic transducers under variable temperature field," *Journal of Intelligent Material Systems and Structures,* vol. 27, pp. 337-349, 2016.

[142] M. T. Ong and E. J. Reed, "Engineered piezoelectricity in graphene," *ACS nano,* vol. 6, pp. 1387-1394, 2012.

[143] S. Chandratre and P. Sharma, "Coaxing graphene to be piezoelectric," *Applied Physics Letters,* vol. 100, p. 023114, 2012.

[144] Y. Xu, C. Chen, V. V. Deshpande, F. A. DiRenno, A. Gondarenko, D. B. Heinz*, et al.*, "Radio frequency electrical transduction of graphene mechanical resonators," *Applied Physics Letters,* vol. 97, p. 243111, 2010.

[145] C. Chen, S. Rosenblatt, K. I. Bolotin, W. Kalb, P. Kim, I. Kymissis*, et al.*, "Performance of monolayer graphene nanomechanical resonators with electrical readout," *Nature nanotechnology,* vol. 4, pp. 861-867, 2009.

[146] K. Matsui, A. Inaba, Y. Oshidari, Y. Takei, H. Takahashi, T. Takahata*, et al.*, "Mechanical properties of few layer graphene cantilever," in *Micro Electro Mechanical Systems (MEMS), 2014 IEEE 27th International Conference on*, 2014, pp. 1087-1090.

[147] I. Berinskii, D. Indeitsev, N. Morozov, D. Y. Skubov, and L. Shtukin, "Differential graphene resonator as a mass detector," *Mechanics of Solids,* vol. 50, pp. 127-134, 2015.

[148] R. A. Barton, B. Ilic, A. M. Van Der Zande, W. S. Whitney, P. L. McEuen, J. M. Parpia*, et al.*, "High, size-dependent quality factor in an array of graphene mechanical resonators," *Nano letters,* vol. 11, pp. 1232-1236, 2011.

[149] C. Wong, M. Annamalai, Z. Wang, and M. Palaniapan, "Characterization of nanomechanical graphene drum structures," *Journal of Micromechanics and Microengineering,* vol. 20, p. 115029, 2010.

[150] R. N. Patel, J. P. Mathew, A. Borah, and M. M. Deshmukh, "Low tension graphene drums for electromechanical pressure sensing," *2D Materials,* vol. 3, p. 011003, 2016.

[151] R. A. Barton, I. R. Storch, V. P. Adiga, R. Sakakibara, B. R. Cipriany, B. Ilic*, et al.*, "Photothermal self-oscillation and laser cooling of graphene optomechanical systems," *Nano letters,* vol. 12, pp. 4681-4686, 2012.

[152] G. Stemme, "Resonant silicon sensors," *Journal of Micromechanics and Microengineering,* vol. 1, p. 113, 1991.

[153] A. Naik, M. Hanay, W. Hiebert, X. Feng, and M. Roukes, "Towards single-molecule nanomechanical mass spectrometry," *Nature nanotechnology,* vol. 4, pp. 445-450, 2009.

[154] R. A. Barton, J. Parpia, and H. G. Craighead, "Fabrication and performance of graphene nanoelectromechanical systems," *Journal of Vacuum Science & Technology B,* vol. 29, p. 050801, 2011.

[155] Y. Oshidari, T. Hatakeyama, R. Kometani, S. i. Warisawa, and S. Ishihara, "High quality factor graphene resonator fabrication using resist shrinkage-induced strain," *Applied Physics Express,* vol. 5, p. 117201, 2012.

[156] A. R. Kermany, J. S. Bennett, V. M. Valenzuela, W. P. Bowen, and F. Iacopi, "Potential of epitaxial silicon carbide microbeam resonators for chemical sensing," *physica status solidi (a),* 2016.

[157] C. Chen and J. Hone, "Graphene nanoelectromechanical systems," *Proceedings of the IEEE,* vol. 101, pp. 1766-1779, 2013.

[158] V. Gouttenoire, T. Barois, S. Perisanu, J. L. Leclercq, S. T. Purcell, P. Vincent*, et al.*, "Digital and FM Demodulation of a Doubly Clamped Single-Walled Carbon-Nanotube Oscillator: Towards a Nanotube Cell Phone," *Small,* vol. 6, pp. 1060-1065, 2010.

[159] V. Sazonova, Y. Yaish, H. Üstünel, D. Roundy, T. A. Arias, and P. L. McEuen, "A tunable carbon nanotube electromechanical oscillator," *Nature,* vol. 431, pp. 284-287, 2004.

[160] S. Lee, C. Chen, V. V. Deshpande, G.-H. Lee, I. Lee, M. Lekas*, et al.*, "Electrically integrated SU-8 clamped graphene drum resonators for strain engineering," *Applied Physics Letters,* vol. 102, p. 153101, 2013.

[161] C. Chen, V. V. Deshpande, M. Koshino, S. Lee, A. Gondarenko, A. H. MacDonald*, et al.*, "Modulation of mechanical resonance by chemical potential oscillation in graphene," *Nature Physics,* vol. 12, pp. 240-244, 2016.

[162] C. Chen, S. Lee, V. V. Deshpande, G.-H. Lee, M. Lekas, K. Shepard*, et al.*, "Graphene mechanical oscillators with tunable frequency," *Nature nanotechnology,* vol. 8, pp. 923-927, 2013.

[163] A. M. v. d. Zande, R. A. Barton, J. S. Alden, C. S. Ruiz-Vargas, W. S. Whitney, P. H. Pham*, et al.*, "Large-scale arrays of single-layer graphene resonators," *Nano letters,* vol. 10, pp. 4869-4873, 2010.

[164] D. Garcia-Sanchez, A. M. van der Zande, A. S. Paulo, B. Lassagne, P. L. McEuen, and A. Bachtold, "Imaging mechanical vibrations in suspended graphene sheets," *Nano letters,* vol. 8, pp. 1399-1403, 2008.

[165] S. Y. Kim and H. S. Park, "The importance of edge effects on the intrinsic loss mechanisms of graphene nanoresonators," *Nano letters,* vol. 9, pp. 969-974, 2009.

[166] J.-W. Jiang and J.-S. Wang, "Why edge effects are important on the intrinsic loss mechanisms of graphene nanoresonators," *Journal of Applied Physics,* vol. 111, p. 054314, 2012.

[167] T. Miao, S. Yeom, P. Wang, B. Standley, and M. Bockrath, "Graphene nanoelectromechanical systems as stochastic-frequency oscillators," *Nano letters,* vol. 14, pp. 2982-2987, 2014.

[168] A. R. Kermany, G. Brawley, N. Mishra, E. Sheridan, W. P. Bowen, and F. Iacopi, "Microresonators with Q-factors over a million from highly stressed epitaxial silicon carbide on silicon," *Applied Physics Letters,* vol. 104, p. 081901, 2014.

[169] M. Takamura, H. Okamoto, K. Furukawa, H. Yamaguchi, and H. Hibino, "Energy dissipation in edged and edgeless graphene mechanical resonators," *Journal of Applied Physics,* vol. 116, p. 064304, 2014.

[170] S. S. Verbridge, H. G. Craighead, and J. M. Parpia, "A megahertz nanomechanical resonator with room temperature quality factor over a million," *Applied Physics Letters,* vol. 92, pp. 13112-13112, 2008.

[171] J. T. Robinson, M. Zalalutdinov, J. W. Baldwin, E. S. Snow, Z. Wei, P. Sheehan*, et al.*, "Wafer-scale reduced graphene oxide films for nanomechanical devices," *Nano letters,* vol. 8, pp. 3441-3445, 2008.

[172] M. K. Zalalutdinov, J. T. Robinson, C. E. Junkermeier, J. C. Culbertson, T. L. Reinecke, R. Stine*, et al.*, "Engineering graphene mechanical systems," *Nano letters,* vol. 12, pp. 4212-4218, 2012.

[173] S. Adhikari and R. Chowdhury, "Zeptogram sensing from gigahertz vibration: Graphene based nanosensor," *Physica E: Low-dimensional Systems and Nanostructures,* vol. 44, pp. 1528-1534, 2012.

[174] R. De Alba, F. Massel, I. Storch, T. Abhilash, A. Hui, P. McEuen*, et al.*, "Tunable phonon cavity coupling in graphene membranes," *arXiv preprint arXiv:1604.04605,* 2016.

[175] J. P. Mathew, R. N. Patel, A. Borah, R. Vijay, and M. M. Deshmukh, "Dynamical strong coupling and parametric amplification of mechanical modes of graphene drums," *Nature nanotechnology,* 2016.

[176] C. Yan, J. Wang, W. Kang, M. Cui, X. Wang, C. Y. Foo*, et al.*, "Highly stretchable piezoresistive graphene–nanocellulose nanopaper for strain sensors," *Advanced Materials,* vol. 26, pp. 2022-2027, 2014.

[177] T.-L. Ren, H. Tian, D. Xie, and Y. Yang, "Flexible graphite-on-paper piezoresistive sensors," *Sensors,* vol. 12, pp. 6685-6694, 2012.

[178] E. Kälvesten, L. Smith, L. Tenerz, and G. Stemme, "The first surface micromachined pressure sensor for cardiovascular pressure measurements," in *Micro Electro Mechanical Systems, 1998. MEMS 98. Proceedings., The Eleventh Annual International Workshop on*, 1998, pp. 574-579.

[179] J. Zhao, G. Wang, R. Yang, X. Lu, M. Cheng, C. He*, et al.*, "Tunable Piezoresistivity of Nanographene Films for Strain Sensing," *ACS nano,* vol. 9, pp. 1622-1629, 2015.

[180] T. Yamada, Y. Hayamizu, Y. Yamamoto, Y. Yomogida, A. Izadi-Najafabadi, D. N. Futaba*, et al.*, "A stretchable carbon nanotube strain sensor for human-motion detection," *Nature nanotechnology,* vol. 6, pp. 296-301, 2011.

[181] M. AliáMohammad, "A flexible, transparent and ultrathin single-layer graphene earphone," *RSC Advances,* vol. 5, pp. 17366-17371, 2015.

[182] J. W. Suk, K. Kirk, Y. Hao, N. A. Hall, and R. S. Ruoff, "Thermoacoustic sound generation from monolayer graphene for transparent and flexible sound sources," *Advanced Materials,* vol. 24, pp. 6342-6347, 2012.

[183] H. Tian, D. Xie, Y. Yang, T.-L. Ren, Y.-F. Wang, C.-J. Zhou*, et al.*, "Single-layer graphene sound-emitting devices: experiments and modeling," *Nanoscale,* vol. 4, pp. 2272-2277, 2012.

[184] H. Tian, T.-L. Ren, D. Xie, Y.-F. Wang, C.-J. Zhou, T.-T. Feng*, et al.*, "Graphene-on-paper sound source devices," *ACS nano,* vol. 5, pp. 4878-4885, 2011.

[185] W. Fei, J. Zhou, and W. Guo, "Low-voltage Driven Graphene Foam Thermoacoustic Speaker," *Small,* vol. 11, pp. 2252-2256, 2015.

[186] H. Tian, C. Li, M. A. Mohammad, Y.-L. Cui, W.-T. Mi, Y. Yang*, et al.*, "Graphene earphones: Entertainment for both humans and animals," *ACS nano,* vol. 8, pp. 5883-5890, 2014.

[187] Q. Zhou and A. Zettl, "Electrostatic graphene loudspeaker," *Applied Physics Letters,* vol. 102, p. 223109, 2013.

[188] P. K. Nayak, C.-J. Hsu, S.-C. Wang, J. C. Sung, and J.-L. Huang, "Graphene coated Ni films: A protective coating," *Thin Solid Films,* vol. 529, pp. 312-316, 2013.

[189] E. Pop, V. Varshney, and A. K. Roy, "Thermal properties of graphene: Fundamentals and applications," *MRS bulletin,* vol. 37, pp. 1273-1281, 2012.

[190] R. Nair, P. Blake, A. Grigorenko, K. Novoselov, T. Booth, T. Stauber*, et al.*, "Fine structure constant defines visual transparency of graphene," *Science,* vol. 320, pp. 1308-1308, 2008.

[191] M. Schriver, W. Regan, W. J. Gannett, A. M. Zaniewski, M. F. Crommie, and A. Zettl, "Graphene as a long-term metal oxidation barrier: worse than nothing," *ACS nano,* vol. 7, pp. 5763-5768, 2013.

[192] L. Nilsson, M. Andersen, R. Balog, E. Lægsgaard, P. Hofmann, F. Besenbacher*, et al.*, "Graphene coatings: probing the limits of the one atom thick protection layer," *ACS nano,* vol. 6, pp. 10258-10266, 2012.

[193] J.-H. Huh, S. H. Kim, J. H. Chu, S. Y. Kim, J. H. Kim, and S.-Y. Kwon, "Enhancement of seawater corrosion resistance in copper using acetone-derived graphene coating," *Nanoscale,* vol. 6, pp. 4379-4386, 2014.

[194] D.-e. Jiang, B. G. Sumpter, and S. Dai, "Unique chemical reactivity of a graphene nanoribbon's zigzag edge," *The Journal of chemical physics,* vol. 126, p. 134701, 2007.

[195] J. Jin, X. Wang, and M. Song, "Graphene-based nanostructured hybrid materials for conductive and superhydrophobic functional coatings," *Journal of nanoscience and nanotechnology,* vol. 11, pp. 7715-7722, 2011.

[196] N. Li, L. Liu, and F. Yang, "Highly conductive graphene/PANi-phytic acid modified cathodic filter membrane and its antifouling property in EMBR in neutral conditions," *Desalination,* vol. 338, pp. 10-16, 2014.

[197] S. Anandan, T. Narasinga Rao, M. Sathish, D. Rangappa, I. Honma, and M. Miyauchi, "Superhydrophilic graphene-loaded TiO2 thin film for self-cleaning applications," *ACS applied materials & interfaces,* vol. 5, pp. 207-212, 2012.

[198] X. Wang, L. Song, H. Yang, H. Lu, and Y. Hu, "Synergistic effect of graphene on antidripping and fire resistance of intumescent flame retardant poly (butylene succinate) composites," *Industrial & Engineering Chemistry Research,* vol. 50, pp. 5376-5383, 2011.

[199] Y. Shi, X. Qian, K. Zhou, Q. Tang, S. Jiang, B. Wang*, et al.*, "CuO/graphene nanohybrids: preparation and enhancement on thermal stability and smoke suppression of polypropylene," *Industrial & Engineering Chemistry Research,* vol. 52, pp. 13654-13660, 2013.

[200] S.-D. Jiang, Z.-M. Bai, G. Tang, Y. Hu, and L. Song, "Synthesis of ZnS decorated graphene sheets for reducing fire hazards of epoxy composites," *Industrial & Engineering Chemistry Research,* vol. 53, pp. 6708-6717, 2014.

[201] D. Berman, A. Erdemir, and A. V. Sumant, "Few layer graphene to reduce wear and friction on sliding steel surfaces," *Carbon,* vol. 54, pp. 454-459, 2013.

[202] M.-S. Won, O. V. Penkov, and D.-E. Kim, "Durability and degradation mechanism of graphene coatings deposited on Cu substrates under dry contact sliding," *Carbon,* vol. 54, pp. 472-481, 2013.

[203] D. Berman, A. Erdemir, and A. V. Sumant, "Reduced wear and friction enabled by graphene layers on sliding steel surfaces in dry nitrogen," *Carbon,* vol. 59, pp. 167-175, 2013.

[204] A. J. Marsden, M. Phillips, and N. R. Wilson, "Friction force microscopy: a simple technique for identifying graphene on rough substrates and mapping the orientation of graphene grains on copper," *Nanotechnology,* vol. 24, p. 255704, 2013.

[205] D. Berman, S. A. Deshmukh, S. K. Sankaranarayanan, A. Erdemir, and A. V. Sumant, "Macroscale superlubricity enabled by graphene nanoscroll formation," *Science,* vol. 348, pp. 1118-1122, 2015.

[206] K. I. Bolotin, K. Sikes, Z. Jiang, M. Klima, G. Fudenberg, J. Hone*, et al.*, "Ultrahigh electron mobility in suspended graphene," *Solid State Communications,* vol. 146, pp. 351-355, 2008.

[207] H.-L. Lee, Y.-C. Yang, and W.-J. Chang, "Mass detection using a graphene-based nanomechanical resonator," *Japanese Journal of Applied Physics,* vol. 52, p. 025101, 2013.

[208] H. Sone, Y. Fujinuma, and S. Hosaka, "Picogram mass sensor using resonance frequency shift of cantilever," *Japanese Journal of Applied Physics,* vol. 43, p. 3648, 2004.

[209] G. Abadal, Z. J. Davis, B. Helbo, X. Borrise, R. Ruiz, A. Boisen*, et al.*, "Electromechanical model of a resonating nano-cantilever-based sensor for

high-resolution and high-sensitivity mass detection," *Nanotechnology,* vol. 12, p. 100, 2001.

[210] K. Ekinci, Y. Yang, and M. Roukes, "Ultimate limits to inertial mass sensing based upon nanoelectromechanical systems," *Journal of applied physics,* vol. 95, pp. 2682-2689, 2004.

[211] B. Lassagne, D. Garcia-Sanchez, A. Aguasca, and A. Bachtold, "Ultrasensitive mass sensing with a nanotube electromechanical resonator," *Nano letters,* vol. 8, pp. 3735-3738, 2008.

[212] J. Chaste, A. Eichler, J. Moser, G. Ceballos, R. Rurali, and A. Bachtold, "A nanomechanical mass sensor with yoctogram resolution," *Nature nanotechnology,* vol. 7, pp. 301-304, 2012.

[213] K. Ekinci, X. Huang, and M. Roukes, "Ultrasensitive nanoelectromechanical mass detection," *Applied Physics Letters,* vol. 84, pp. 4469-4471, 2004.

[214] C. Sun, M. S. Boutilier, H. Au, P. Poesio, B. Bai, R. Karnik*, et al.*, "Mechanisms of molecular permeation through nanoporous graphene membranes," *Langmuir,* vol. 30, pp. 675-682, 2014.

[215] S. Garaj, W. Hubbard, A. Reina, J. Kong, D. Branton, and J. Golovchenko, "Graphene as a subnanometre trans-electrode membrane," *Nature,* vol. 467, pp. 190-193, 2010.

[216] D. Cohen-Tanugi and J. C. Grossman, "Water desalination across nanoporous graphene," *Nano letters,* vol. 12, pp. 3602-3608, 2012.

[217] D.-e. Jiang, V. R. Cooper, and S. Dai, "Porous graphene as the ultimate membrane for gas separation," *Nano letters,* vol. 9, pp. 4019-4024, 2009.

[218] A. W. Hauser and P. Schwerdtfeger, "Nanoporous graphene membranes for efficient 3He/4He separation," *The Journal of Physical Chemistry Letters,* vol. 3, pp. 209-213, 2012.

[219] S. C. O'Hern, M. S. Boutilier, J.-C. Idrobo, Y. Song, J. Kong, T. Laoui*, et al.*, "Selective ionic transport through tunable subnanometer pores in single-layer graphene membranes," *Nano letters,* vol. 14, pp. 1234-1241, 2014.

[220] D. C. Bell, M. C. Lemme, L. A. Stern, J. R. Williams, and C. M. Marcus, "Precision cutting and patterning of graphene with helium ions," *Nanotechnology,* vol. 20, p. 455301, 2009.

[221] M. D. Fischbein and M. Drndić, "Electron beam nanosculpting of suspended graphene sheets," *Applied Physics Letters,* vol. 93, p. 113107, 2008.

[222] P. Xu, J. Yang, K. Wang, Z. Zhou, and P. Shen, "Porous graphene: properties, preparation, and potential applications," *Chinese Science Bulletin,* vol. 57, pp. 2948-2955, 2012.

[223] B. Wen, C. Sun, and B. Bai, "Inhibition effect of a non-permeating component on gas permeability of nanoporous graphene membranes," *Physical Chemistry Chemical Physics,* vol. 17, pp. 23619-23626, 2015.

[224] C. Sathe, X. Zou, J.-P. Leburton, and K. Schulten, "Computational investigation of DNA detection using graphene nanopores," *ACS nano,* vol. 5, pp. 8842-8851, 2011.

[225] H. W. C. Postma, "Rapid sequencing of individual DNA molecules in graphene nanogaps," *Nano letters,* vol. 10, pp. 420-425, 2010.

[226] C. A. Merchant, K. Healy, M. Wanunu, V. Ray, N. Peterman, J. Bartel*, et al.*, "DNA translocation through graphene nanopores," *Nano letters,* vol. 10, pp. 2915-2921, 2010.

[227] C. J. Russo and J. Golovchenko, "Atom-by-atom nucleation and growth of graphene nanopores," *Proceedings of the National Academy of Sciences,* vol. 109, pp. 5953-5957, 2012.

[228] M. E. Suk and N. Aluru, "Water transport through ultrathin graphene," *The Journal of Physical Chemistry Letters,* vol. 1, pp. 1590-1594, 2010.

[229] E. N. Wang and R. Karnik, "Water desalination: Graphene cleans up water," *Nature nanotechnology,* vol. 7, pp. 552-554, 2012.

[230] D. Cohen-Tanugi and J. C. Grossman, "Nanoporous graphene as a reverse osmosis membrane: Recent insights from theory and simulation," *Desalination,* vol. 366, pp. 59-70, 2015.

[231] S. Gangadoo, A. Taylor-Robinson, and J. Chapman, "Nanoparticle and biomaterial characterisation techniques," *Materials Technology,* vol. 30, pp. B44-B56, 2015.

[232] (date accessed 15 August 2017). *Radiological and Environmental Management, Purdue University.* Available: https://www.purdue.edu/ehps/rem/rs/sem.htm

[233] (date accessed 7 August,2017). *Sample-Electron Interaction*. Available: http://www.nanoscience.com/technology/sem-technology/sample-electron-interaction/

[234] (date accessed 15 August 2017). *Theory of Raman Scattering*. Available: http://bwtek.com/raman-theory-of-raman-scattering/

[235] (date accessed 15 August 2017). *X-Ray Photoelectron Spectroscopy*. Available: https://wiki.utep.edu/display/~anarayanaswamy/X-Ray+Photoelectron+Spectroscopy

[236] (date accessed 14 June 2017). *Surface Analysis by X-Ray Photoelectron Spectroscopy – XPS*. Available: http://www.andersonmaterials.com/xps.html

[237] Mai. (date accessed June 5,2017). *Fundamental Theory of Atomic Force Microscopy*. Available: http://nanoscience.gatech.edu/research/Fundamental%20AFM.php

[238] (date accessed June 8 2017). *Atomic Force Microscopy*. Available: http://www.jpk.com/what-is-atomic-force-microscopy.432.en.html

[239] (date accessed 5 June 2017). *Veeco Dimension 3100 Atomic Force Microscope Users Manual*. Available: https://www.nist.gov/sites/default/files/documents/2017/05/09/Veeco_Dimension3100_AFM_USERMANUAL_v1.pdf

[240] G. S. May and C. J. Spanos, *Fundamentals of semiconductor manufacturing and process control*: John Wiley & Sons, 2006.

[241] A. Remennikov and M. Roche, "NEW COMPOSITE CONSTRUCTION OF HYBRID BEAMS COMBINING STEEL INVERTED T-SECTION AND RC FLANGE."

[242] "Instruction Manual, Delaminator Adhesion Test System; DTS Company, Menlo Park, CA," ed.

[243] Z. Gan, S. G. Mhaisalkar, Z. Chen, S. Zhang, Z. Chen, and K. Prasad, "Study of interfacial adhesion energy of multilayered ULSI thin film structures using four-point bending test," *Surface and Coatings Technology,* vol. 198, pp. 85-89, 2005.

[244] R. Dauskardt, M. Lane, Q. Ma, and N. Krishna, "Adhesion and debonding of multi-layer thin film structures," *Engineering Fracture Mechanics,* vol. 61, pp. 141-162, 1998.

[245] K. Zetie, S. Adams, and R. Tocknell, "How does a Mach-Zehnder interferometer work?," *Physics Education,* vol. 35, p. 46, 2000.

[246] K. Y. Yasumura, T. D. Stowe, E. M. Chow, T. Pfafman, T. W. Kenny, B. C. Stipe*, et al.*, "Quality factors in micron-and submicron-thick cantilevers," *Journal of microelectromechanical systems,* vol. 9, pp. 117-125, 2000.

[247] Z. Cao, L. Tao, D. Akinwande, R. Huang, and K. M. Liechti, "Mixed-mode interactions between graphene and substrates by blister tests," *Journal of Applied Mechanics,* vol. 82, p. 081008, 2015.

[248] R. G. Azevedo, D. G. Jones, A. V. Jog, B. Jamshidi, D. R. Myers, L. Chen*, et al.*, "A SiC MEMS resonant strain sensor for harsh environment applications," *IEEE Sensors Journal,* vol. 7, pp. 568-576, 2007.

[249] N. Wright and A. Horsfall, "SiC sensors: a review," *Journal of Physics D: Applied Physics,* vol. 40, p. 6345, 2007.

[250] V. Cimalla, J. Pezoldt, and O. Ambacher, "Group III nitride and SiC based MEMS and NEMS: materials properties, technology and applications," *Journal of Physics D: Applied Physics,* vol. 40, p. 6386, 2007.

[251] P. M. Sarro, "Silicon carbide as a new MEMS technology," *Sensors and Actuators A: Physical,* vol. 82, pp. 210-218, 2000.

[252] O. Cooper, B. Wang, C. L. Brown, J. Tiralongo, and F. Iacopi, "Toward Label-Free Biosensing With Silicon Carbide: A Review," *IEEE Access,* vol. 4, pp. 477-497, 2016.

[253] A. Boisen, S. Dohn, S. S. Keller, S. Schmid, and M. Tenje, "Cantilever-like micromechanical sensors," *Reports on Progress in Physics,* vol. 74, p. 036101, 2011.

[254] R. Sandberg, K. Mølhave, A. Boisen, and W. Svendsen, "Effect of gold coating on the Q-factor of a resonant cantilever," *Journal of Micromechanics and Microengineering,* vol. 15, p. 2249, 2005.

[255] L. Sekaric, D. Carr, S. Evoy, J. Parpia, and H. Craighead, "Nanomechanical resonant structures in silicon nitride: fabrication, operation and dissipation issues," *Sensors and Actuators A: Physical,* vol. 101, pp. 215-219, 2002.

[256] P.-L. Yu, T. Purdy, and C. Regal, "Control of material damping in high-Q membrane microresonators," *Physical review letters,* vol. 108, p. 083603, 2012.

[257] S. Lee, V. P. Adiga, R. A. Barton, A. M. van der Zande, G.-H. Lee, B. R. Ilic*, et al.*, "Graphene Metallization of High-Stress Silicon Nitride Resonators for Electrical Integration," *Nano letters,* vol. 13, pp. 4275-4279, 2013.

[258] S. M. Avdoshenko, C. G. da Rocha, and G. Cuniberti, "Nanoscale ear drum: Graphene based nanoscale sensors," *Nanoscale,* vol. 4, pp. 3168-3174, 2012.

[259] S. E. Saddow, C. L. Frewin, C. Coletti, N. Schettini, E. Weeber, A. Oliveros*, et al.*, "Single-crystal silicon carbide: A biocompatible and hemocompatible semiconductor for advanced biomedical applications," in *Materials Science Forum*, 2011, pp. 824-830.

[260] S. E. Saddow, *Silicon carbide biotechnology: a biocompatible semiconductor for advanced biomedical devices and applications*: Elsevier, 2012.

[261] A. M. Pinto, I. C. Gonçalves, and F. D. Magalhães, "Graphene-based materials biocompatibility: a review," *Colloids and Surfaces B: Biointerfaces,* vol. 111, pp. 188-202, 2013.

[262] L. Wang, S. Dimitrijev, J. Han, P. Tanner, A. Iacopi, and L. Hold, "Demonstration of p-type 3C-SiC grown on 150 mm Si (100) substrates by atomic-layer epitaxy at 1000°C," *journal of crystal growth,* vol. 329, pp. 67-70, 2011.

[263] S. Singh, J. R. Potopowicz, L. G. Van Uitert, and S. H. Wemple, "Nonlinear optical properties of hexagonal silicon carbide," *Applied Physics Letters,* vol. 19, pp. 53-56, 1971.

[264] F. Iacopi, G. Walker, L. Wang, L. Malesys, S. Ma, B. V. Cunning*, et al.*, "Orientation-dependent stress relaxation in hetero-epitaxial 3C-SiC films," *Applied Physics Letters,* vol. 102, p. 011908, 2013.

[265] F. Iacopi, R. E. Brock, A. Iacopi, L. Hold, and R. H. Dauskardt, "Evidence of a highly compressed nanolayer at the epitaxial silicon carbide interface with silicon," *Acta Materialia,* vol. 61, pp. 6533-6540, 2013.

[266] A. R. Kermany and F. Iacopi, "Controlling the intrinsic bending of hetero-epitaxial silicon carbide micro-cantilevers," *Journal of Applied Physics,* vol. 118, p. 155304, 2015.

[267] H. Yao, L. Ouyang, and W. Y. Ching, "Ab initio calculation of elastic constants of ceramic crystals," *Journal of the American Ceramic Society,* vol. 90, pp. 3194-3204, 2007.

[268] K. P. Zetie, S. F. Adams, and R. M. Tocknell, "How does a Mach-Zehnder interferometer work?," *Physics Education,* vol. 35, p. 46, 2000.

[269] K. Y. Yasumura, T. D. Stowe, E. M. Chow, T. Pfafman, T. W. Kenny, B. C. Stipe*, et al.*, "Quality factors in micron-and submicron-thick cantilevers," *IEEE Journal of Microelectromechanical Systems,* vol. 9, pp. 117-125, 2000.

[270] A. R. Kermany, "'Design and fabrication of SiC micro-transducers with large Q-factors for high resolution sensing'," PhD dessertation, School of Engineering, Griffith University, Brisbane, QLD, Australia.

[271] S. Ma, S. Wang, F. Iacopi, and H. Huang, "A resonant method for determining the residual stress and elastic modulus of a thin film," *Applied Physics Letters,* vol. 103, p. 031603, 2013.

[272] V. P. Adiga, B. Ilic, R. Barton, I. Wilson-Rae, H. Craighead, and J. Parpia, "Approaching intrinsic performance in ultra-thin silicon nitride drum resonators," *Journal of Applied Physics,* vol. 112, p. 064323, 2012.

[273] V. Adiga, B. Ilic, R. Barton, I. Wilson-Rae, H. Craighead, and J. Parpia, "Modal dependence of dissipation in silicon nitride drum resonators," *Applied Physics Letters,* vol. 99, p. 253103, 2011.

[274] P. Kanjanaboos, X.-M. Lin, J. E. Sader, S. M. Rupich, H. M. Jaeger, and J. R. Guest, "Self-assembled nanoparticle drumhead resonators," *Nano letters,* vol. 13, pp. 2158-2162, 2013.

[275] H. Schlicke, C. J. Schröter, and T. Vossmeyer, "Electrostatically driven drumhead resonators based on freestanding membranes of cross-linked gold nanoparticles," *Nanoscale,* vol. 8, pp. 15880-15887, 2016.

[276] F. Avilés, A. Oliva, and A. May-Pat, "Determination of Elastic Modulus in a Bimaterial Through a One-dimensional Laminated Model," *Journal of Materials Engineering and Performance,* vol. 17, pp. 482-488, 2008.

[277] L. G. Villanueva and S. Schmid, "Evidence of surface loss as ubiquitous limiting damping mechanism in SiN micro-and nanomechanical resonators," *Physical review letters,* vol. 113, p. 227201, 2014.

[278] S. Chakram, Y. Patil, L. Chang, and M. Vengalattore, "Dissipation in ultrahigh quality factor SiN membrane resonators," *Physical review letters,* vol. 112, p. 127201, 2014.

[279] N. Mishra, L. Hold, A. Iacopi, B. Gupta, N. Motta, and F. Iacopi, "Controlling the surface roughness of epitaxial SiC on silicon," *Journal of Applied Physics,* vol. 115, p. 203501, 2014.

[280] A. Barnes, R. Roberts, N. Tien, C. Zorman, and P. X.-L. Feng, "Silicon carbide (SiC) membrane nanomechanical resonators with multiple vibrational modes," in *Solid-State Sensors, Actuators and Microsystems Conference (TRANSDUCERS), 2011 16th International*, 2011, pp. 2614-2617.

[281] A. Volinsky, N. Moody, and W. Gerberich, "Interfacial toughness measurements for thin films on substrates," *Acta materialia,* vol. 50, pp. 441-466, 2002.

[282] J. W. Hutchinson and Z. Suo, "Mixed mode cracking in layered materials," *Advances in applied mechanics,* vol. 29, p. 191, 1992.

[283] S. Y. Chang and Y. C. Huang, "Analyses of interface adhesion between porous SiO_2 low-k film and SiC/SiN layers by nanoindentation and nanoscratch tests," *Microelectronic engineering*, vol. 28, p. 319-27, 2007.

[284] J. Tomastik and R. Ctvrtlik, "Nanoscratch test—A tool for evaluation of cohesive and adhesive properties of thin films and coatings," In *EPJ Web of Conferences*, *EDP Sciences*, vol. 48, p. 00027, 2013.